UNIVERSIDADE FEDERAL DO RECÔNCAVO DA BAHIA
CENTRO DE CIÊNCIAS AGRÁRIAS, AMBIENTAIS E BIOLÓGICAS
EMBRAPA MANDIOCA E FRUTICULTURA
PROGRAMA DE PÓS-GRADUAÇÃO EM RECURSOS GENÉTICOS VEGETAIS
CURSO DE MESTRADO

High-throughput phenotyping in castor bean using aerial imagery

Myriam EL ADAS

CRUZ DAS ALMAS-BA
2025

High-throughput phenotyping in castor bean using aerial imagery

Myriam EL ADAS
Duplo diploma em agronomia, Mestre em Agrobiosciências Vegetais
Universidade Libanesa faculdade de Agronomia (ULFA),
Ecole Nationale Supérieure Agronomique de Toulouse (INP-ENSAT)- 2022

Dissertação apresentada ao colegiado do Programa de Pós-Graduação em Recursos Genéticos Vegetais da Universidade Federal do Recôncavo da Bahia, como requisito parcial para a obtenção do título de Mestra em Recursos Genéticos Vegetais.

Orientadora: Profª. Drª. Simone Alves Silva

Co-orientador Pr. Dr. Diego Marmolejo

CRUZ DAS ALMAS-BA
2025

FICHA CATALOGRÁFICA

A221h

Adas, Myriam el.

High-throughput phenotyping in castor bean using aerial imagery / Myriam el Adas._ Cruz das Almas, BA, 2025.

100f.: il.

Dissertação (Mestrado) – Universidade Federal do Recôncavo da Bahia, Centro de Ciências Agrárias Ambientais e Biológicas, Mestrado em Recursos Genéticos Vegetais.

Orientadora: Prof. Dra. Simone Alves Silva.
Coorientador: Prof. Dr. Diego Marmolejo Cortes.

1.Mamona – Caracterização. 2.Mamona – Germoplasma vegetal – Manejo. 3.Fenótipo – Análise. I.Universidade Federal do Recôncavo da Bahia, Centro de Ciências Agrárias Ambientais e Biológicas. II.Título.

CDD: 633.85

Ficha elaborada pela Biblioteca Central da UFRB. Responsável pela Elaboração Antonio Marcos Sarmento das Chagas (Bibliotecário - CRB5 / 1615).

UNIVERSIDADE FEDERAL DO RECÔNCAVO DA BAHIA
CENTRO DE CIÊNCIAS AGRÁRIAS, AMBIENTAIS E BIOLÓGICAS
EMBRAPA MANDIOCA E FRUTICULTURA
PROGRAMA DE PÓS-GRADUAÇÃO EM RECURSOS GENÉTICOS VEGETAIS
CURSO DE MESTRADO

High-throughput phenotyping in castor bean using aerial imagery

COMISSÃO EXAMINADORA DA DEFESA DE DISSERTAÇÃO DE
Myriam EL ADAS

Aprovada em: 14 de agosto de 2025

BANCA EXAMINADORA

Profª. Drª. Simone Alves Silva
Universidade Federal do Recôncavo da Bahia - UFRB
Orientadora

Prof. Dr. Carlos Alberto da Silva Ledo
Universidade Federal do Recôncavo da Bahia - UFRB
Examinador Interno

Documento assinado digitalmente
gov.br
CARLOS ALBERTO DA SILVA LEDO
Data: 14/10/2025 15:27:26-0300
Verifique em https://validar.iti.gov.br

Prof. Dr. Everton Luís Poelking
Universidade Federal do Recôncavo da Bahia - UFRB
Examinador Externo

Documento assinado digitalmente
gov.br
EVERTON LUIS POELKING
Data: 14/10/2025 15:53:07-0300
Verifique em https://validar.iti.gov.br

AGRADECIMENTOS

Gostaria de expressar minha profunda gratidão:

A Deus, por ter me oferecido esse sopro de vida,

À minha família, por ter me ensinado a resiliência,

Ao Brasil, por seu acolhimento caloroso,

À Universidade Federal do Recôncavo da Bahia (UFRB) pela oportunidade,

À CAPES, pelo auxílio financeiro concedido por meio da bolsa de estudos,

Ao Programa de Pós-Graduação em Recursos Genéticos Vegetais pelo curso enriquecedor,

À minha orientadora, Prª Simone Alves, por acreditar em mim,

Ao Pr. Diego Marmolejo, pelo suporte,

Ao Pr. Everton Luís Poelking, pela colaboração e material disponibilizado para conseguir realizar o trabalho,

À equipe da fazenda experimental, pelo apoio no campo,

A toda a equipe do grupo de Pesquisa NBIO e NucGEO, pela união,

A todos os professores das disciplinas cursadas durante o mestrado, pelos ensinamentos,

A todos os meus colegas que fizeram parte dessa caminhada e deixaram ela mais leve!

Fenotipagem de alto rendimento da mamona utilizando imagens aéreas

Autora: Myriam EL ADAS
Orientadora: Dra. Simone Alves Silva

RESUMO:

A caracterização morfológica da mamoneira (*Ricinus communis* L.) é desafiadora por depender de numerosos descritores, muitas vezes trabalhosos, subjetivos e destrutivos. Este estudo avaliou o potencial de imagens obtidas por Aeronaves Remotamente Pilotadas (ARP), com sensores RGB e multiespectrais, para fenotipagem de alto rendimento ao longo dos principais estádios fenológicos, além de propor uma metodologia aplicada. Conduziu-se experimento com duas cultivares (IAC-80, BRS-ENERGIA) e duas linhagens (UFRB-23, UFRB-222) do banco de germoplasma do NBIO/UFRB. Realizaram-se 10 voos com DJI Mavic 3 Entreprise M, mantendo GSD fixo de 1,84 cm/pixel. No primeiro estudo, estimativas de altura de plantas derivadas de Modelos Digitais de Elevação (MDEs) produzidos a partir de imagens RGB foram comparadas a medições diretas. Observaram-se correlações fortes nos 105, 118 e 132 dias após a semeadura ($R \geq 0,94$), sobretudo no estádio reprodutivo. A análise de Bland–Altman confirmou a concordância entre os métodos, com viés mínimo quando as plantas atingiram altura acima de 1,2 m. No segundo estudo, ajustaram-se seis modelos de regressão às trajetórias de crescimento de 13 índices de vegetação RGB e 23 multiespectrais nos quatro genótipos. Os modelos quadrático e exponencial mostraram maior estabilidade, enquanto funções mais complexas, como Gompertz e Richards, foram mais suscetíveis a falhas em conjuntos com baixa variância. Entre os índices, GLI e RGBVI apresentaram ajustes moderados (R^2 = 0,63–0,76), refletindo dinâmicas fenológicas coerentes com as observações de campo. Em conjunto, os resultados validam o uso integrado de imagens RGB e multiespectrais obtidas por ARP na fenotipagem de características e da fenologia da mamoneira, oferecendo uma abordagem promissora para acelerar aplicações no melhoramento genético de *Ricinus communis*.

Palavra-chaves: *Ricinus communis L.*; altura da planta; estádio fenológico

High-throughput phenotyping in castor bean using aerial imagery

Author: Myriam EL ADAS
Advisor: Drª. Simone Alves Silva

ABSTRACT:

Morphological characterization of castor bean (Ricinus communis L.) is challenging because it relies on many qualitative and quantitative descriptors that are often labor-intensive, subjective, and destructive. This study evaluated the potential of Remotely Piloted Aircraft (RPA) imagery—RGB and multispectral—for high-throughput phenotyping across the main phenological stages and proposed a practical workflow. The experiment involved two cultivars (IAC-80, BRS-ENERGIA) and two lines (UFRB-23, UFRB-222) from the NBIO/UFRB germplasm bank. A total of ten flights were performed with a DJI Mavic 3 Enterprise M, using a fixed GSD of 1.84 cm/pixel. In the first study, plant height estimates derived from Digital Elevation Models (DEM) built from RGB images were compared with direct field measurements. Strong correlations were observed at 105, 118, and 132 days after sowing ($R \geq 0.94$), especially during the reproductive stage. Bland–Altman analysis confirmed agreement between methods, with minimal bias when plants exceeded 1.2 m in height. In the second study, six regression models were fitted to the time series values of 13 RGB vegetation indices and 23 multispectral indices across the four genotypes. Quadratic and exponential models showed greater stability, whereas more complex functions such as Gompertz and Richards were more susceptible to failures in low-variance datasets. Among the indices, GLI and RGBVI produced moderate fits ($R^2 = 0.63–0.76$), reflecting phenological trends consistent with field observations for all genotypes. The results validate the use of RGB and multispectral RPA imagery for phenotyping castor bean traits and phenology. This approach offers a promising tool for accelerating breeding applications in *Ricinus communis*.

Keywords: *Ricinus communis L.*; plant height; phenological stage

Table of contents

GENERAL INTRODUCTION 9
LITERATURE REVIEW 12
1. Castor bean: description, distribution, uses, production, and breeding 12
2. Phenological stages of castor bean 14
3. Grey mold attacks on Castor bean 18
4. RPA-imagery as a HTP technique 18
5. Regression growth models 21
REFERENCES 24
CHAPTER 1: Estimating plant height in castor bean using RPA-derived Digital Elevation Models from RGB images 29
RESUMO 30
ABSTRACT 31
INTRODUCTION 32
MATERIALS AND METHODS 33
1.1. Plant material 33
1.2. Study area 34
1.3. Experimental design 34
1.4. Meteorological data 35
1.5. Monitoring date 35
1.6. Field data acquisition and calculation 36
1.7. Phenological stage determination 37
1.8. Aerial Image acquisition 39
1.9. Digital Elevation Model (DEM) creation 41
1.10. Extraction of Plant height using DEM 42
1.11. Statistical analysis 43
RESULTS 44
2.1 Climatic conditions 44
2.2 Flight parameters 45
2.3 Phenological stages 47
2.4 Canopy area and volume 47
2.5 Direct measurement of plant height 49
2.6 Agreement between estimated and measured plant height 49
DISCUSSION 53
CONCLUSION 55
REFERENCES 57
CHAPTER 2: Phenological modeling of castor bean based on RPA-derived vegetation indices 58
RESUMO 59
ABSTRACT 60
INTRODUCTION 61

MATERIALS AND METHODS **63**
1.1. Plant material 63
1.2. Study area 64
1.3. Experimental design 64
1.4. Meteorological data 65
1.5. Grey mold severity monitoring 65
1.6. Monitoring date 67
1.7. Aerial Image acquisition 67
1.8. Orthomosaic creation 70
1.9. Vegetation Indices calculation using Orthomosaic 70
1.10. Phenological models 74
RESULTS **77**
2.1 Climatic conditions 77
2.2 Grey mold incidence and severity 77
2.3 Plant yield 79
2.4 Flight parameters 80
2.5 Vegetation indices 82
2.6 Phenology models 85
DISCUSSION **93**
CONCLUSION **95**
REFERENCES **98**

GENERAL INTRODUCTION

Phenotypic characterization is an important tool to assess variability within plant genetic resources along with molecular characterization. However, extensive phenotypic data is considered nowadays as a bottleneck for crop breeding and functional genomics research because this method is time-consuming, labor intensive, subjective, and frequently destructive to plants. Additionally, crop characteristics and yields often vary within a single farm area, emphasizing the need for site-specific analysis or precision farming techniques to maximize output. (SONG et al., 2021)

As a result, a wide range of innovative technologies and strategies are being developed to monitor crops and related field data. These advancements include the use of smart agriculture, precision agriculture, Remotely Piloted Aircrafts (RPA), wireless communication technologies, the Internet of Things (IoT), and smartphone applications tailored for agricultural use. When applied to breeding programs, these advanced technologies could serve as interesting tools for high-throughput phenotyping. Therefore, these tools can facilitate the phenotypic evaluation process by enhancing its efficiency in terms of time and data quality and quantity (SOUSSI et al., 2024).

The use of aerial images using satellite and RPA images in the Euphorbeaceae family is mainly done with *Hevea brasiliensis, Manihot esculenta.* However, there are only a few studies done with *Ricinus communis* L.. For example, yield prediction was performed using Sentinel-2A derived indices namely NDVI and EVI and linear regression in a semi-arid region of India (KUMAR et al., 2023). Infrared thermometer, and spectral radiometer were used to monitor stress in germplasm and yield prediction (KUMAR et al., 2005).

Considering the fact that Brazil ranks third in the world for castor bean production, after India and Mozambique (FAO, 2021), as well as its several uses in the industrial, cosmetic and medicinal sectors, this crop catches the attention of researchers and breeders. However, due to the scarcity of studies related to high-throughput phenotyping using RPA-images and prediction models used within this species, it is important to evaluate the applicability of these technologies in castor bean breeding programs for selecting promising accessions.

Despite the increasing use of satellite and aerial images for crop monitoring, limitations still exist when applying these technologies to castor bean (*Ricinus communis* L.). Satellite imagery, although valuable for large-scale monitoring, presents restrictions in spatial resolution, acquisition frequency, and susceptibility to atmospheric conditions such as cloud cover, which hinder its effectiveness in breeding trials and small experimental plots (MAES; STEPPE, 2019; JONES et al., 2019). In contrast, Remotely Piloted Aircrafts (RPA) allow the acquisition of high-resolution data at flexible times and at different phenological stages, enabling the monitoring of small targets and improving the precision of site-specific analysis (ZHANG; KOVACS, 2012). Considering the global importance of castor bean and the scarcity of studies using RPA-derived imagery for high-throughput phenotyping in this species, there is a clear need to evaluate and establish methodologies that integrate these technologies into breeding programs.

The cultivation of castor bean holds significant socio-economic value in Brazil, primarily concentrated in the state of Bahia, in the northeastern region within a semi-arid environment, it is managed by small-scale family-owned farms. The Nucleus of Genetic Improvement and Biotechnology (NBIO) of the Federal University of the Reconcavo of Bahia (UFRB) has developed since 2004 the only castor bean germplasm bank in the state of Bahia (EMBRAPA, 2023). However, there are other institutions such as Embrapa Algodão and Instituto Agronômico de Campinas (IAC) that have their own collections of castor bean germplasm and commercialized cultivars in the states of Paraíba and São Paulo (MILANI et al., 2007)

Therefore, four genetic materials were used in this study, including two promising lineages UFRB-222 and UFRB-23 developed by the NBIO breeding program, and two cultivars, IAC-80 developed by IAC, and BRS-ENERGIA developed by Embrapa Algodão. The RPA images were taken using a DJI Mavic 3 Enterprise equipped with an RGB and a multispectral camera, including Red, Blue, Red-edge and Infra-red bands. A total of nine flights were done, the first flight occurred during the insertion of the primary raceme, and the ultimate occurred at the maturation stage. Various growth, phenological and yield descriptors were evaluated in the field, mostly at the same date of the flights. In addition, grey mold occurrence and scale was monitored during crop cycle.

The main objective of this study was to develop a methodology for high-throughput phenotyping of castor bean using RPA-derived imagery, with the purpose of supporting genetic breeding programs through accurate and efficient phenotypic evaluations.

The first chapter entitled “Estimating plant height in castor bean using RPA-derived Digital Elevation Models from RGB images”, examines the capacity of RPA to estimate individual plant height at different phenological stages of the castor bean plant at a fixed flight altitude of 40 meters above ground, comparing the agreement of estimated plant height values with direct field measurements using the Bland-Altman method.

The second chapter entitled “Phenological modeling of castor bean based on RPA-derived vegetation indices”, explores the use of vegetation indices calculated from RGB and multispectral RPA images to model plant phenology throughout its growth cycle. In this study, six growth models (Logistic, Gompertz, Richards, Weibull, Exponential, and quadratic) were tested for each genotype-index combination. Model performance was assessed using R^2 and the Akaike Information Criterion (AIC), allowing selection of the best-fitting model in each case. Model performance was visualized through R^2 and AIC graphs. The five best-performing indices per genotype were identified using a combined standardized score of R^2 and AIC, and their phenological curves were plotted.

LITERATURE REVIEW

1. Castor bean: description, distribution, uses, production, and breeding

Ricinus communis L., commonly known as "castor bean" in English or "Mamona" in Portuguese, is a robust oleaginous shrub that belongs to the family Euphorbiaceae (GISD, 2023). Castor bean exhibits diverse regional distribution, favoring tropical, subtropical, and warm-temperate zones due to its adaptability to arid and semi-arid climates. However, it is unsuitable for profitable cultivation in cold and temperate regions (GISD, 2023), (LANDONI, M. et al., 2023), (ESALQ, 2023). The extracted castor oil from the seeds comprises a blend of esters of both saturated and unsaturated fatty acids, primarily consisting of 90% of ricinoleic acid and 10% of palmitic, stearic, oleic, linoleic, and linolenic acid linked to glycerol (LANDONI, M. et al., 2023), (ESALQ, 2023). Although the seeds themselves are non-edible and possess toxicity for animals and humans due to the presence of the toxic lectin, ricin, it is noteworthy that the castor oil remains free from this harm due to the fact that ricin is insoluble in oil (KAIIMA, 2023). Castor oil possesses notable properties. It demonstrates solubility in alcohol, maintains a liquid state even at temperatures below -30°C, and exhibits a viscosity 18 times higher than other vegetable oils (ESALQ, 2023). The initial oil extraction involves hot or cold pressing to yield castor cake, while the remaining oil is extracted through a solvent extraction technique utilizing n-hexane. Subsequently, the oil undergoes a refining process to obtain the final castor oil product, leaving behind the extracted solid termed de-oiled castor cake (ICOA, 2023). This versatile vegetable oil and its derivatives find applications across various sectors. In the industrial domain, they serve as lubricants, paints, coatings, and polymers. In the pharmaceutical industry, castor oil is utilized as a laxative. It is also incorporated into cosmetic products and employed as a fertilizer or for phytoremediation in agriculture. Additionally, it serves as an emulsifier within the food industry (SHEKADE, S. V. et al., 2023).

The FAO reported in 2021 that India was the largest global producer of castor bean seeds, generating 1647000 tons. Mozambique followed in second place with an output of 72783.38 tons, with Brazil ranking third with 35195 tons. China secured the fourth spot, producing 21000 tons (FAOSTAT, 2021). The cultivation of castor bean holds significant

socio-economic value in Brazil, primarily concentrated in the state of Bahia, in the northeastern region within a semi-arid environment, it is managed by small-scale family-owned farms. The cultivation of castor beans in Brazil is closely linked to family farming due to its ability to withstand water deficits and adapt to the semi-arid conditions of the region. It can be grown with minimal mechanization and can yield successful harvests when intercropped with beans and corn, making it an ideal choice for family farming. However, despite its advantages, the castor bean industry has experienced a stagnation, contrasting with the growth seen in other sectors of Brazilian agribusiness (EMBRAPA, 2023).

In this regard, genetic enhancement can contribute to the development of productive cultivars adapted to diverse climatic conditions with traits that facilitate their management and production, and most importantly meeting the needs of the market and the small-scale farmers (SHEKADE, S. V. et al., 2023). Brazilian public institutions such as Instituto Agronômico (IAC) and Embrapa Algodão had developed castor bean cultivars since 1974 and 1987 respectively (MOREIRA et al., 1996)

Castor bean breeding employs techniques commonly used for self-pollinating species, although the plant exhibits an intermediate reproductive system. The most common method used to select high heritability traits is mass selection. It involves selecting superior plants from existing cultivars or local varieties to enhance or standardize economically important traits. Another breeding technique is Individual Plant Selection with Progeny Testing, where the breeder selects individual plants and evaluates their progeny in subsequent generation, discarding progeny that perform below the control, that is usually a commercialized cultivar. The Pure line selection technique is used on segregated populations derived from hybridization, the selection starts in the F2 population where genetic variability is highest, and continues through controlled self-pollination and evaluation of descendants. Backcrossing is a breeding method employed to introduce a specific trait from a donor parent into the genetic background of an elite cultivar (recurrent parent). This technique is particularly effective for traits governed by one or a few genes, such as specific plant architecture, or seed characteristics. Ultimately, the Single seed descent technique is based on the hybridization of one or more parents with interesting traits. The resulting F1 is self-pollinated to obtain the F2 seeds, then one

seed per plant is randomly selected to grow the F3 generation. This step is repeated for about 5–6 generations, lines become homozygous and genetically stable. Then phenotypic and genotypic selection are performed on traits like oil content, disease resistance, and plant architecture. SSD allows breeders to quickly develop pure lines from segregating populations (MOREIRA, J., et al., 1996).

Since 2005, the Nucleus of Genetic Improvement and Biotechnology (NBIO) at the Federal University of Recôncavo da Bahia (UFRB) have started the castor bean genetic improvement program using the Single Seed Descent (SSD) technique, focusing on creating enhanced lineages with high oil content, compact stature, improved productivity, and tolerance for semi-arid regions, achieving significant advancements in the cultivation. Phenotypic characterization is an important tool to assess variability within the NBIO's castor bean germplasm along with molecular characterization.

2. Phenological stages of castor bean

Castor bean produces a thyrse-type (branched) inflorescence at the tip of the main axis as well as on all lateral axes. Each inflorescence is monoecious, it is composed of carpellate flowers in the distal position and staminate flowers in the proximal position. The first raceme emerges at the terminal point of the main shoot; it is the largest and most productive. Subsequently, lateral axes develop and produce terminal inflorescences, referred to as the second and third racemes, which progressively decrease in size (CLASSEN-BOCKHOFF; FRANKENHÄUSER, 2020; HUSSEN K. W., 2022).

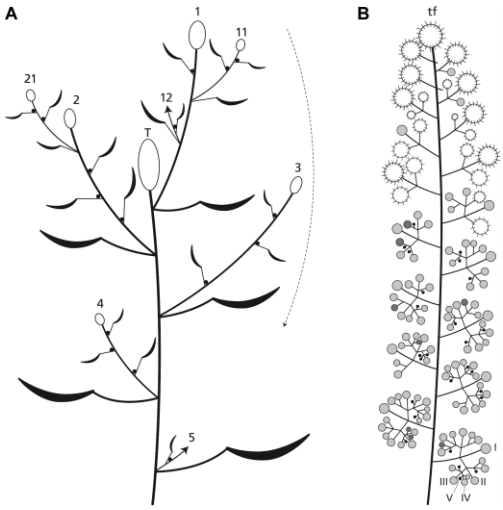


Figure 1. Plant and inflorescence architecture.

(A) The main axis ends in a terminal inflorescence (T). Lateral axes (1–4) also produce terminal inflorescences which flower in basipetal direction (arrow). Uppermost branches overtop the terminal inflorescence and continue to branch (11, 21) in a sympodial manner. **(B)** The inflorescence is a thyrse with a terminal unit (usually a terminal flower: tf) and up to five branch orders (I–V). Its distal part bears predominantly carpellate flowers (large circles), the proximal one staminate units (small circles). The pictured inflorescence is at the end of anthesis. The carpellate flowers are already fruiting, most of the staminate units are in the postfloral stage (gray) few of them are flowering (dark gray) or still in the bud stage (black). (CLASSEN-BOCKHOFF; FRANKENHÄUSER, 2020)

The staminate flowers possess a calyx divided into five lobes and stamens with secondary branches. Their color is pale yellow at the time of anthesis. The carpellate flowers feature a calyx with three parts; the pistil includes an ovary composed of three carpels with sessile stigmas. Each carpel contains an ovule, and the stigmas appear red during anthesis.

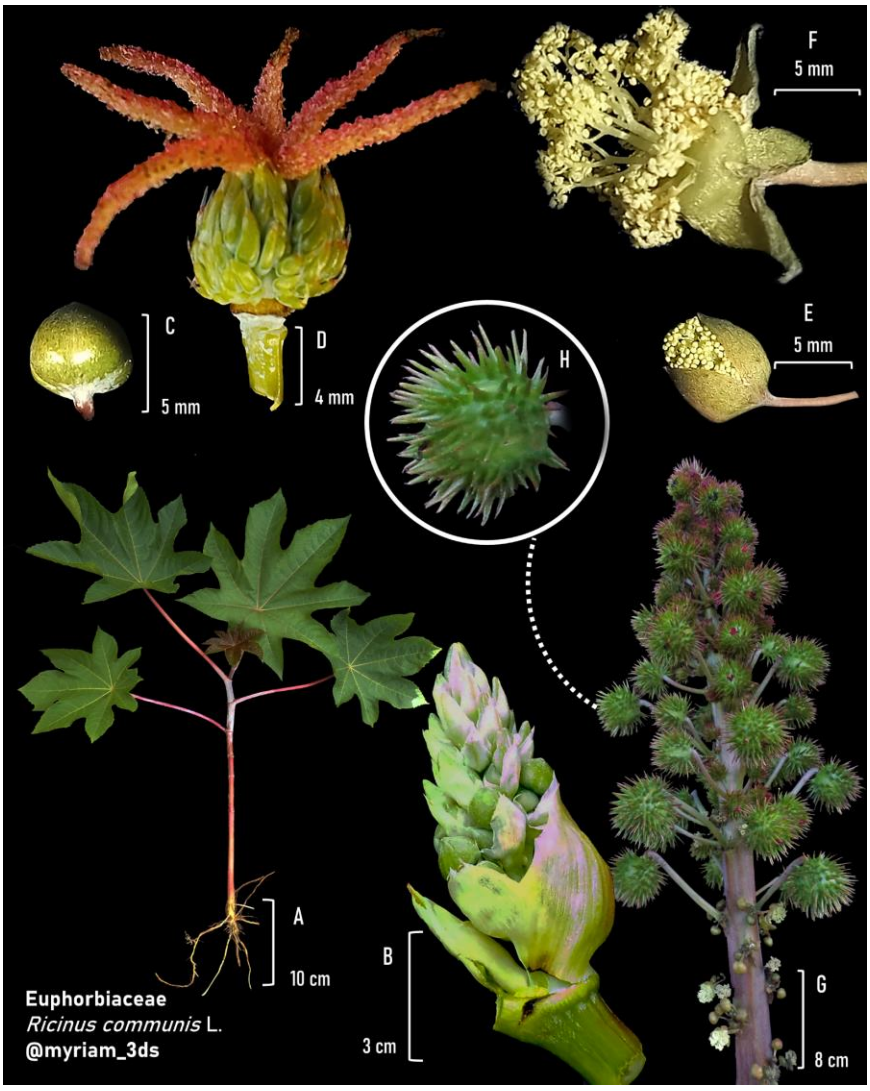


Figure 2. *Botanical photographic plate of Ricinus communis L. A: Castor bean plant at 5 leaves stage; B: Flower bud at emergence stage; C: Closed carpellate flower; D: Carpellate flower at anthesis stage; E: Staminate flower opening; F: Staminate flower fully opened; G: Raceme at grain formation stage; H: Immature fruit at grain formation stage. (El ADAS, M., 2023)*

Four stages and fifteen-substages were defined by Gervasio, F.A.R. *et al.* (2016). The phenological stages of castor bean were described as shown in table 1.

Table 1 : The standardized crop phenology of castor bean (adapted from GERVASIO et al., 2016)

Stage	Substage	Description
Initial Growth stage	**Ve**	Cotyledons
	Vm	1-2 true leaves
	Vo	3-5 true leaves
Growth stage	**F1**	Initial flowering stage with the **emergence of primary racemes**.
	A1	**Anthesis** stage with the appearance of primary raceme inflorescences.
	F2	Secondary flowering stage with the **emergence of secondary racemes**.
	G1	Stage of initial **grain formation in primary racemes**.
	A2	**Anthesis** stage with the appearance of secondary raceme inflorescences.
Productive stage	**F3**	Tertiary flowering stage with the **emergence of tertiary racemes**.
	G2	Stage of initial **grain formation in secondary racemes**.
	A3	**Anthesis** stage with the appearance of tertiary raceme inflorescences.
	M1	Stage of **initial fruit maturation in primary racemes**.
	G3	Stage of **grain formation in tertiary racemes**.
	M2	Stage of **fruit maturation in secondary racemes**.
Maturation	**M3**	Final stage of **leaf fall and fruit maturation in tertiary racemes**.

The germination of castor bean seeds marks the initial growth stage. During this phase, the primary stem elongates vertically, accompanied by the development of true leaves. The growth stage continues with the emergence of a terminal inflorescence at the main shoot, known as the primary raceme, which is the largest and the first to flower. This stage encompasses the emergence, anthesis, and grain formation of the first raceme, as well as the emergence and anthesis of the second raceme. The third stage, referred to as the productive stage, begins with the emergence of the tertiary raceme. The final stage, called

maturation, is characterized by leaf senescence and the maturation of fruits on the tertiary raceme.

3. Grey mold attacks on Castor bean

Castor is affected by several pathogens such as fungi, bacteria, viruses and nematodes. One of the most destructive diseases that can cause a 100% loss in castor bean production in the northeast region of Bahia is grey mold. The causal agent, *Amphobotrys ricini*, is an ascomycete fungus belonging to the order Helotiales and the family Sclerotiniaceae. High precipitation, relative humidity of 80%, and temperatures around 25 °C when coinciding with the flowering and fruiting period, provide optimal conditions for the fungus to break dormancy and colonize its unique host: the castor bean plant. This pathogen can infect nearly all parts of the plant at any stage of its life cycle. Initial symptoms of infection include small grey-blue marks; as the disease progresses, a greenish mycelial mass may cover the entire raceme, leading to partial or complete destruction. This fungus exhibits high genetic variability, which enables it to develop resistance to fungicides. Chemical control with curative spraying may be used once the disease is present. However, no fungicides are currently registered for this crop. It is recommended to remove and destroy infected plants, planting at recommended time and to practice crop rotation. The use of cultivars resistant to grey mold is the most effective and desirable management strategy; however, cultivars with high levels of resistance to this disease are still being developed (MILANI, et al., 2005; SOARES et al., 2022)

4. RPA-imagery as a HTP technique

High-throughput phenotyping (HTP) technique is based on a large-scale evaluation of plant performance using advanced technologies such as cameras, sensors, and robotic platforms that gather a large amount of detailed plant measurements that enhance our understanding of crop physiology, morphology and biochemical traits. HTP can facilitate the phenotypic evaluation process by enhancing its efficiency in terms of time and data quality and quantity (FAHLGREN, N., et al., 2015)

Remote sensing involves capturing images of the Earth's surface from a distance using sensors mounted on aircraft or satellites. Digital cameras can function as remote

sensors when installed on aerial platforms. These sensors detect reflected energy at different wavelengths. Color images are created by combining data from blue, green, and red bands. The level of detail in these images depends on spatial resolution, which defines the sensor's ability to distinguish objects by size. Through specialized cameras embarked to Remotely Piloted Aircraft, also known as RPA, one can measure the light reflected by the plant surface. Multispectral images are captured by cameras that record the reflected light in a limited number of discrete wavelengths of the electromagnetic spectrum, typically ranging from 3 to 10 bands. In contrast, hyperspectral images are acquired through cameras capable of capturing data in numerous bands, often covering a continuous range of wavelengths across the electromagnetic spectrum. Hyperspectral data tends to be more data-intensive and necessitates advanced processing techniques, while multispectral data is more accessible and easier to process for general applications.

This methodology relies on the absorption of solar radiation by the plant to facilitate its natural photosynthetic process. The reflected light is influenced by the concentration of biochemical compounds in the leaf, as well as the foliar surface and internal structure. Depending on its wavelength, the reflected light provides a diverse range of information about plant composition. For example, chlorophyll absorbs primarily in the red visible region of the spectrum and partially in the blue and green regions, which are also generally absorbed by other pigments like xanthophylls and carotenoids. Moreover, foliar absorption/reflection in the near-infrared region is mainly dependent on the structural discontinuities and water content of foliar cells (FILELLA I., *et al*, 2019; UMILES GROUP, 2023).

The raw images taken by the RPA are compiled to form a unique photo known as orthomosaic. It is a raster that represents a matrix containing pixel-specific reflectance data. The raw reflectance data are converted into mathematical combinations of two or more bands known as vegetation indices (VIs) that are broadly used to measure biomass, plant health, chlorophyll content, water content, nutrient content, and yield. Researchers are increasingly adopting the integration of VIs HTP applications because they can rapidly and economically assess plant traits across extensive areas without damaging the plants (TAYADE, R., *et al,* 2022).

On the other hand, these technologies face challenges with field phenotyping for breeding, mainly due to the influence of multiple stresses and environmental variations over the resulting phenotype. Furthermore, image resolution and mosaicking difficulties are reducing the precision of the collected data, resulting in inefficient plant breeding (CHAWADE, A. et al., 2019). Additionally, RPA are suitable for relatively small plots at a breaking point of an area of five hectares (LUKAS, V. et al., 2022).

In RPA imaging, the key spatial-resolution parameter is the Ground Sampling Distance (GSD), i.e., the distance on the ground represented by one pixel ($cm \cdot px^{-1}$). GSD depends jointly on sensor pixel size, lens focal length, and height above ground. Therefore, flight altitude alone is not a portable parameter for reproducing a methodology when different cameras or lenses are used. For methodological reproducibility across platforms, one should specify and match a target GSD (and image overlap), then compute the required flight altitude for each camera to reach that GSD (PIX4D, 2024; WINGTRA, 2024; INERTIAL LABS, 2025; MAES, 2025).

Vegetation Indices (VIs) are band combinations designed to enhance biophysical signals from canopies. Classical indices include NDVI (NIR, red) for overall greenness and canopy vigor (ROUSE et al., 1974), SAVI/OSAVI to mitigate soil background (HUETE, 1988; RONDEAUX; STEVEN; BARET, 1996), and EVI to reduce atmospheric/soil and high-LAI saturation effects (HUETE et al., 2002). Indices exploiting green and red-edge bands—e.g., GNDVI (greater sensitivity to chlorophyll/nitrogen) and NDRE/chlorophyll indices—are widely used to estimate chlorophyll content, LAI, and nutritional status (GITELSON; MERZLYAK, 1998; CLEVERS; GITELSON, 2013; DAUGHTRY et al., 2000). Collectively, these VIs are foundational for high-throughput phenotyping because they enable non-destructive, repeatable measurements linked to biomass, LAI, chlorophyll, water status, and yield components.

Time-series of VIs (NDVI, EVI, red-edge/green-based indices) are standard for extracting phenological metrics (start of season, green-up, peak, senescence) and for fitting growth curves across genotypes and environments (ZENG et al., 2020; DRONOVA, 2022). In addition to descriptive curve fitting, many studies have applied regression models to link VIs with crop traits such as biomass, LAI, chlorophyll content, and yield. For instance, linear regression between Sentinel-2 NDVI/EVI and castor bean yield

showed promising results under semi-arid conditions (KUMAR et al., 2023). Similar approaches have been reported for rice, wheat, maize, and cotton, using both simple linear and nonlinear regression (exponential, quadratic, logistic) to estimate plant growth and productivity from RPA multispectral indices (GNYP et al., 2014; SUN et al., 2017; LIU et al., 2018; YENDREK et al., 2017).

5. Regression growth models

In regression analysis, a model is considered linear or nonlinear depending on its parameters, not the shape of the curve. A regression model is linear if the parameters appear linearly in the equation, even if the predictor variables are raised to powers or involve transformations. For example, the quadratic polynomial model($y = \beta_0 + \beta_1 x + \beta_2 x$) is a linear model because the parameters (β_0,β_1,β_2) are not multiplied or transformed. In contrast, nonlinear models include cases where parameters appear in exponents, denominators, or as part of nonlinear functions. For example, the Logistic model ($y = \frac{A}{1 + e(\frac{x - x_0}{B})}$) is nonlinear because parameters A,B, x_0, are involved inside an exponential and denominator, making estimation dependent on iterative methods such as nonlinear least squares (SEBER; WILD, 2003; DRAPER; SMITH, 1998).

Non-linear mathematical models are particularly suited to describing biological growth dynamics, since vegetation growth and vegetation indices (VIs) typically follow sigmoidal or exponential-like trajectories (ZHU et al., 2023). At the initial growth phase, VI values increase slowly, then accelerate as the canopy expands, stabilize at maturity when photosynthetic activity peaks, and finally decline during senescence (ZEIDE, 1985).

According to Yuki et al. (2019), before fitting a model, a guiding biological question should be defined — in the case of VI-based growth modeling, the key question is whether the chosen VI adequately represents the phenological dynamics of the crop. Model calibration is performed by estimating parameters using nonlinear least squares for nonlinear models, and ordinary least squares for linear models such as quadratic regression. Commonly applied growth models in crop phenology include the Logistic, Gompertz, Richards, Weibull, Exponential, and Quadratic polynomial models (RICHARDS, 1959; GOMPERTZ, 1825; CAUSTON; VENUS, 1981).

Model performance is evaluated to discriminate between candidates in terms of how well they represent experimental data. A common selection criterion is the Akaike Information Criterion (AIC), this method is a tool used to compare and select models based on their goodness of fit while penalizing complexity, identifying the model that most efficiently explains the data with the fewest parameters. Increased complexity can lead to overfitting. AIC comparison must be limited to the same experiment, species, and dataset; however, it can compare models that are structurally different.(BURNHAM; ANDERSON, 2002). AIC is defined as:

(1) $$AIC = 2k - 2ln(\hat{L})$$

Where:

K = number of estimated parameters

$\hat{L}$ = maximum likelihood of the model

The lower the AIC, the better the model among the tested models for the same dataset. However, to interpret the results, the differences between the AIC values (ΔAIC), known as Akaike weights, are calculated. These give information about the relative probability that each model is the best one among the set considered. Thus, the Akaike weight quantifies the evidence in favor of each biological assumption.

To calculate the Akaike weight:

1. Compute $\Delta_i$for each model, this estimates the information loss when using model i rather than the best model. Hence the larger Δ_i, the less plausible is model i

(2) $$\Delta_i = AIC_i - min(AIC)$$

where:

$min(AIC)$ = AIC value of the best model in the collection

AIC_i = model i

2. Rescale and normalize the Δ_i values so that the resulting weights sum to 1, giving the Akaike weight, which represents the probability that model i is the best model. The smaller the Akaike weight, the less plausible that model i is the best. A single best model can be considered if its Akaike weight ω_i >0.9.

(3) $$\omega_i = \frac{exp(-\Delta_i/2)}{\sum_{r=1}^{R} exp(-\Delta_r/2)}$$

General conclusion

Together, the literature shows that castor bean's agronomic relevance and wide distribution demand phenotyping methods aligned with its distinct phenological stages. RPA-based imagery emerges as a practical high-throughput solution for plot-scale, repeatable measurements when planned around target GSD and standardized acquisition, enabling both structural (height) and functional (spectral) traits to be captured. Vegetation indices and regression growth models provide the analytical bridge from raw imagery to biologically interpretable dynamics.

Chapter 1 validates an RPA workflow to estimate individual plant height across phenological stages from RGB-derived DEMs, assessing agreement with field measurements (Bland–Altman). Chapter 2 then models phenology from RGB and multispectral VI time series using linear (quadratic) and nonlinear (Logistic, Gompertz, Richards, Weibull, Exponential) growth functions, comparing fits via AIC and Akaike weights to identify genotype-specific indices and curves most informative for breeding decisions.

REFERENCES

BURNHAM, K. P.; ANDERSON, D. R. *Model selection and multimodel inference: a practical information-theoretic approach*. 2. ed. New York: Springer, 2002.

CASTOR. Kaiima, [s.d.]. Disponível em: https://kaiima.com/castor/. Acesso em: 10 nov. 2023.

CAUSTON, D. R.; VENUS, J. C. *The Biometry of Plant Growth*. London: Edward Arnold, 1981.

CHAWADE, A. et al. High-throughput field-phenotyping tools for plant breeding and precision agriculture. *Agronomy*, [S. l.], v. 9, n. 5, p. 258, 2019. Disponível em: https://doi.org/10.3390/agronomy9050258. Acesso em: 27 maio 2025.

CLASSEN-BOCKHOFF, R.; FRANKENHÄUSER, H. The 'male flower' of *Ricinus communis* (Euphorbiaceae) interpreted as a multi-flowered unit. *Frontiers in Cell and Developmental Biology*, Lausanne, v. 8, p. 525561, 2020. DOI: https://doi.org/10.3389/fcell.2020.525561.

CLEVERS, J.; GITELSON, A. Remote estimation of crop and grass chlorophyll and nitrogen content using red-edge bands on Sentinel-2 and -3. *International Journal of Applied Earth Observation and Geoinformation*, Amsterdam, v. 23, p. 344–351, 2013. DOI: https://doi.org/10.1016/j.jag.2012.10.008.

DAUGHTRY, C. S. T.; WICEK, J.; BIRKELAND, R.; YANG, C.; … Estimating corn leaf chlorophyll concentration from leaf and canopy reflectance (MCARI). *Remote Sensing of Environment*, Amsterdam, v. 74, n. 2, p. 229–239, 2000. DOI: https://doi.org/10.1016/S0034-4257(00)00113-9.

DRAPER, N. R.; SMITH, H. *Applied regression analysis*. 3. ed. New York: John Wiley & Sons, 1998.

DRONOVA, I. Remote sensing of phenology: Towards the comprehensive understanding of land surface phenology. *Journal of Ecology*, London, v. 110, n. 8, p. 1890–1912, 2022. DOI: https://doi.org/10.1111/1365-2745.13897.

ESALQ. Disponível em: https://www.esalq.usp.br/departamentos/lgn/pub/seminar/MBMNobrega-200602-Resumo.pdf. Acesso em: 10 nov. 2023.

ESTATÍSTICAS - Portal Embrapa. Disponível em: https://www.embrapa.br/agencia-de-informacao-tecnologica/cultivos/mamona/pre-producao/socioeconomia/estatisticas. Acesso em: 10 nov. 2023.

FAHLGREN, N.; GEHAN, M. A.; BAXTER, I. Lights, camera, action: high-throughput plant phenotyping is ready for a close-up. *Current Opinion in Plant Biology*, v. 24, p. 93–99, 2015.

FAOSTAT. Disponível em: https://www.fao.org/faostat/en/#data/QCL. Acesso em: 10 nov. 2023.

FARRAR, C. R.; WORDEN, K. Supervised Learning – Classification and Regression. In: FARRAR, Charles R.; WORDEN, Keith. *Structural Health Monitoring: A Machine Learning Perspective*. Hoboken: Wiley, 2012. p. 361–401. Disponível em: https://doi.org/10.1002/9781118443118.ch11.

FILELLA, I.; BJERKE, J. W.; MACIAS-FAURIA, M. Reflectance assessment of plant physiological status – ClimEx Handbook. *ClimEx Handbook: Handbook for standardized measurements in climate change*

experiments, 2019. Disponível em: https://climexhandbook.w.uib.no/2019/11/03/reflectance-assessment-of-plant-physiological-status/. Acesso em: 11 nov. 2023.

GERVASIO, F. A. R. et al. Method and phenological characterization of the stadiums and phases of the development of castor bean plants. *African Journal of Agricultural Research*, [S. l.], v. 11, n. 44, p. 4488–4497, 3 nov. 2016. DOI: https://doi.org/10.5897/AJAR2016.11337.

GISD – Global Invasive Species Database. *Ricinus communis*. Disponível em: http://www.iucngisd.org/gisd/speciesname/Ricinus+communis. Acesso em: 10 nov. 2023.

GITELSON, A. A.; MERZLYAK, M. N. Remote sensing of chlorophyll concentration in higher plant leaves. *Advances in Space Research*, Oxford, v. 22, n. 5, p. 689–692, 1998. DOI: https://doi.org/10.1016/S0273-1177(97)01133-2.

GOMPERTZ, B. On the nature of the function expressive of the law of human mortality. *Philosophical Transactions of the Royal Society of London*, London, v. 115, p. 513–585, 1825. DOI: https://doi.org/10.1098/rstl.1825.0026.

GNYP, M. L.; LIU, W.; MIAO, Y.; CHEN, X.; RIECHERS, M.; STÜNZI, J.; WALTER, A.; KAUFMANN, H. Hyperspectral canopy sensing of paddy rice aboveground biomass at different growth stages. *Field Crops Research*, Amsterdam, v. 155, p. 42–55, 2014. DOI: https://doi.org/10.1016/j.fcr.2013.09.023.

HUETE, A. R. A soil-adjusted vegetation index (SAVI). *Remote Sensing of Environment*, Amsterdam, v. 25, n. 3, p. 295–309, 1988. DOI: https://doi.org/10.1016/0034-4257(88)90106-X.

HUETE, A.; DIDAN, K.; MIURA, T.; RODRIGUEZ, E. P.; GAO, X.; FERREIRA, L. G. Overview of the radiometric and biophysical performance of the MODIS vegetation indices. *Remote Sensing of Environment*, Amsterdam, v. 83, p. 195–213, 2002. DOI: https://doi.org/10.1016/S0034-4257(02)00096-2.

HUSSEIN, K. W. Review on Reproductive Biology of Caster bean (*Ricinus communis* L.). *Journal of Ecology and Natural Resources*, v. 6, n. 1, 2022. Disponível em: https://medwinpublishers.com/JENR/review-on-reproductive-biology-of-caster-bean--(ricinus-communis-l.).pdf. Acesso em: 6 jun. 2025.

ICOA – International Castor Oil Association. [S. l.]: ICOA, [s.d.]. Disponível em: https://www.icoa.org. Acesso em: 10 nov. 2023.

INERTIAL LABS. How to calculate Ground Sampling Distance (GSD). 2025. Available at: https://inertiallabs.com/how-to-calculate-ground-sampling-distance/. Accessed: 29 Aug. 2025.

JANIESCH, C.; ZSCHECH, P.; HEINRICH, K. Machine learning and deep learning. *Electronic Markets*, [S. l.], v. 31, n. 3, p. 685–695, 2021. Disponível em: https://doi.org/10.1007/s12525-021-00475-2. Acesso em: 27 maio 2025.

JONES, H. G.; SCHOFIELD, P.; WEST, J. S. Precision agriculture for crop protection. *Functional Plant Biology*, Melbourne, v. 46, n. 2, p. 173–188, 2019. DOI: https://doi.org/10.1071/FP18090.

KRAUSE, S. European beech spring phenological phase prediction with UAV-based multispectral data and machine learning. *Scientific Reports*, London, v. 14, 66338, 2024. DOI: https://doi.org/10.1038/s41598-024-

66338-w.

KUMAR, P. et al. Use of remote sensing for drought stress monitoring, yield prediction and varietal evaluation in castor beans (*Ricinus communis* L.). *International Journal of Remote Sensing*, Abingdon, v. 26, p. 5525–5534, 2005. DOI: https://doi.org/10.1080/01431160500285258.

KUMAR, R. et al. Mapping and yield prediction of castor bean (*Ricinus communis*) using Sentinel-2A satellite image in a semi-arid region of India. *Journal of Landscape Ecology*, [S. l.], v. 16, p. 1–23, 2023. DOI: https://doi.org/10.2478/jlecol-2023-0008.

LANDONI, M. et al. Opportunities and challenges of castor bean (*Ricinus communis* L.) genetic improvement. *Agronomy*, Basel, v. 13, n. 8, p. 2076, ago. 2023. DOI: https://doi.org/10.3390/agronomy13082076.

LIU, B.; LIU, L.; XU, X.; ZHANG, J.; SUN, G. Monitoring rice growth based on UAV multispectral remote sensing. *Remote Sensing*, Basel, v. 10, n. 4, p. 542, 2018. DOI: https://doi.org/10.3390/rs10040542.

LUKAS, V. et al. Using UAV to identify the optimal vegetation index for yield prediction of oil seed rape (*Brassica napus* L.) at the flowering stage. *Remote Sensing*, [S. l.], v. 14, n. 19, p. 4953, 2022. Disponível em: https://doi.org/10.3390/rs14194953. Acesso em: 27 maio 2025.

MAES, W. H.; STEPPE, K. Perspectives for remote sensing with unmanned aerial vehicles in precision agriculture. *Trends in Plant Science*, Oxford, v. 24, n. 2, p. 152–164, 2019. DOI: https://doi.org/10.1016/j.tplants.2018.11.007.

MAES, W. H. Practical guidelines for performing UAV mapping flights with snapshot sensors. *Remote Sensing*, Basel, v. 17, n. 4, 606, 2025. DOI: https://doi.org/10.3390/rs17040606.

MILANI, M.; FÁVERO, A. P.; SOUSA, R. L.; DANTAS, F. V. Caracterização de acessos do Banco de Germoplasma de Mamona da Embrapa Algodão. Campina Grande: Embrapa Algodão, 2007. (Comunicado Técnico, n. 310). Disponível em: https://www.infoteca.cnptia.embrapa.br/bitstream/doc/273452/1/COMTEC310.pdf. Acesso em: 10 nov. 2023.

MILANI, M.; NÓBREGA, M. B. M.; SUASSUNA, N. D.; COUTINHO, W. M. Resistência da mamoneira (*Ricinus communis* L.) ao mofo cinzento causado por *Amphobotrys ricini*. Campina Grande: Embrapa Algodão, 2005. 22 p. (Documentos, 137). Disponível em: https://www.infoteca.cnptia.embrapa.br/infoteca/bitstream/doc/277966/1/DOC137.pdf. Acesso em: 10 nov. 2023.

MOREIRA, J. de A. N.; LIMA, E. F.; FARIAS, F. J. C.; AZEVEDO, D. M. P. de. Melhoramento da mamoneira (*Ricinus communis* L.). Campina Grande: EMBRAPA-CNPA, 1996. 6 p. Disponível em: https://www.infoteca.cnptia.embrapa.br/infoteca/bitstream/doc/269457/1/MELHORAMENTODAMAMONEIRA.pdf. Acesso em: 10 nov. 2023.

PIX4D. Ground sampling distance (GSD) in photogrammetry. 2024. Available at: https://support.pix4d.com/hc/en-us/articles/202559809. Accessed: 29 Aug. 2025.

RICHARDS, F. J. A flexible growth function for empirical use. *Journal of Experimental Botany*, Oxford, v. 10, n. 2, p. 290–301, 1959. DOI: https://doi.org/10.1093/jxb/10.2.290.

RONDEAUX, G.; STEVEN, M.; BARET, F. Optimization of soil-adjusted vegetation indices. *Remote Sensing of Environment*, Amsterdam, v. 55, n. 2, p. 95–107, 1996. DOI: https://doi.org/10.1016/0034-4257(95)00186-7.

ROUSE Jr., J. W.; HAAS, R. H.; SCHELL, J. A.; DEERING, D. W. Monitoring vegetation systems in the Great Plains with ERTS. *Third ERTS Symposium Proceedings*. Washington, DC: NASA SP-351, v. 1, p. 48–62, 1974.

RUSSELL, Stuart; NORVIG, Peter. *Artificial Intelligence: A Modern Approach*. 3. ed. Global ed. Harlow: Pearson, 2010.

SEBER, G. A. F.; WILD, C. J. *Nonlinear regression*. Hoboken: Wiley, 2003.

SHEKADE, S. V. et al. Phytochemical, pharmacognostic, and pharmacological aspects of *Ricinus communis* seed oil: an overview. *Natural Products Journal*, Sharjah, v. 13, n. 3, 2023. Disponível em: https://www.ingentaconnect.com/content/ben/npj/2023/00000013/00000003/art00005. Acesso em: 27 maio 2025.

SOARES, D. J.; COUTINHO, W. M.; ARAÚJO, A. E. Doenças da mamoneira. Campina Grande: Embrapa Algodão, 2022. Disponível em: https://www.embrapa.br/agencia-de-informacao-tecnologica/cultivos/mamona/producao/doencas. Acesso em: 10 nov. 2023.

SONG, P. et al. High-throughput phenotyping: breaking through the bottleneck in future crop breeding. *The Crop Journal*, Beijing, v. 9, p. 633–645, 2021. DOI: https://doi.org/10.1016/j.cj.2021.03.015.

SOUSSI, A. et al. Smart sensors and smart data for precision agriculture: a review. *Sensors*, Basel, v. 24, p. 2647, 2024. DOI: https://doi.org/10.3390/s24082647.

SUN, Y.; YU, X.; ZHAO, Y.; WANG, Y. Estimation of cotton yield from UAV-based multispectral imagery using regression models. *Computers and Electronics in Agriculture*, Amsterdam, v. 143, p. 38–47, 2017. DOI: https://doi.org/10.1016/j.compag.2017.09.001.

TAYADE, R. et al. Utilization of spectral indices for high-throughput phenotyping. *Plants*, v. 11, p. 1712, 2022. Disponível em: https://doi.org/10.3390/plants11131712. Acesso em: 26 maio 2025.

UMILES GROUP. RPAS, UAS and UAV: what are they and how do they differ? [S. l.]: UMILES Group, 2023. Disponível em: https://umilesgroup.com/en/rpas-uas-and-uav-what-are-they-and-how-do-they-differ. Acesso em: 19 maio 2025.

WINGTRA. Ground sample distance explained and why it matters. 2024. Available at: https://wingtra.com/surveying-gis/ground-sample-distance/. Accessed: 29 Aug. 2025.

YENDREK, C. R.; TOMAZ, T.; LEAKEY, A. D. B. High-throughput phenotyping of maize leaf physiological and biochemical traits in the field using UAV-based hyperspectral sensing. *Plant Physiology*, Rockville, v. 173, n. 1, p. 614–626, 2017. DOI: https://doi.org/10.1104/pp.16.01447.

YUKI, A. Y.; KAZUTO, K.; MAKOTO, N. Model selection using information criteria for non-linear mixed-effect models of sigmoid growth curves. *Current Plant Biology*, [S. l.], v. 20, p. 100127, 2019. Disponível em: https://www.sciencedirect.com/science/article/pii/S2468042719300508. Acesso em: 28 jul. 2025.

YUKI, S.; MURAKAMI, N.; NAKAGAWA, T. Statistical approaches for crop phenology modeling. *Agricultural Systems*, Amsterdam, v. 174, p. 125–135, 2019. DOI: https://doi.org/10.1016/j.agsy.2019.04.001.

ZENG, L.; WARDLOW, B. D.; XIANG, D.; HU, S.; LI, D. A review of vegetation phenological metrics extraction using time-series, multispectral satellite data. *Remote Sensing of Environment*, Amsterdam, v. 237, 111511, 2020. DOI: https://doi.org/10.1016/j.rse.2019.111511.

ZEIDE, Boris. Analysis of Growth Equations. In: HANN, D. W.; BORDERS, B. E. (ed.). *Forest growth models*. Dordrecht: Springer, 1985. p. 227–254. Disponível em: https://link.springer.com/content/pdf/10.1007/978-94-009-2235-8_12. Acesso em: 28 jul. 2025.

ZEIDE, B. Tolerance of trees to damage. *Forest Ecology and Management*, Amsterdam, v. 13, p. 149–161, 1985. DOI: https://doi.org/10.1016/0378-1127(85)90037-9.

ZHU, Yuwei et al. The Nonlinear Mixed-Effect Models Approach Provides an Efficient Method for Longitudinal Data Analysis in Agricultural Studies. *Agronomy*, Basel, v. 13, n. 8, p. 2042, 2023. Disponível em: https://www.mdpi.com/2073-4395/13/8/2042. Acesso em: 28 jul. 2025.

ZHU, W.; LIU, Y.; LI, J.; CAO, W.; YANG, W. Advances in nonlinear growth modeling of crops based on UAV vegetation indices. *Remote Sensing*, Basel, v. 15, n. 3, 2023. DOI: https://doi.org/10.3390/rs15030761.

ZHANG, C.; KOVACS, J. M. The application of small unmanned aerial systems for precision agriculture: a review. *Precision Agriculture*, Dordrecht, v. 13, n. 6, p. 693–712, 2012. DOI: https://doi.org/10.1007/s11119-012-9274-5.

CHAPTER 1: Estimating plant height in castor bean using RPA-derived Digital Elevation Models from RGB images

CRUZ DAS ALMAS-BA
2025

Uso do RPA na estimativa da altura da mamona utilizando Modelos Digitais de Elevação derivados de imagens RGB.

Autora: Myriam EL ADAS
Orientadora: Dra. Simone Alves Silva

RESUMO

A caracterização morfológica da mamona (*Ricinus communis* L.) apresenta desafios, pois depende de descritores qualitativos e quantitativos que, além de serem trabalhosos e demorados, muitas vezes envolvem medições subjetivas e destrutivas. Para superar essas limitações, este estudo avaliou o uso de Aeronaves Remotamente Pilotadas (ARP) equipadas com sensores RGB de 20 MP como ferramenta de fenotipagem de alto desempenho para estimar a altura de plantas em diferentes estádios fenológicos. O experimento foi conduzido com duas cultivares (IAC-80 e BRS-ENERGIA) e duas linhagens (UFRB-23 e UFRB-222), pertencentes ao banco ativo de germoplasma do Núcleo de Melhoramento de Plantas (NBIO/UFRB). A altura das plantas e outros parâmetros de crescimento foram avaliados em quatro estádios fenológicos. As imagens RGB foram capturadas com o DJI Mavic 3 Enterprise Multispectral com um GSD de 1.84 cm/pix (representando uma altitude de voo de 40 m). Os Modelos Digitais de Elevação (MDE) e os ortomosaicos foram gerados no software *Agisoft Metashape Educational*, e as estimativas de altura foram extraídas com o pacote *FieldImageR* no ambiente *R/QGIS*. As alturas estimadas apresentaram forte correlação com as medições manuais em 105 DAS (R = 0,95; $p < 0,001$), 118 e 132 DAS (R = 0,94; $p < 0,001$). A análise de Bland-Altman indicou boa concordância em 118 DAS, com viés de –0,07 m e limites estreitos de concordância (0,10 a –0,24 m), coincidindo com o estádio reprodutivo, quando as plantas ultrapassaram 1,20 m. Contudo, a acurácia da estimativa foi influenciada pela densidade foliar, estrutura da copa, o GSD e as condições ambientais. Recomenda-se a realização de estudos adicionais com variação do GSD ao longo do ciclo para aprimorar a robustez do método.

Palavra-chaves: *Ricinus communis L.*, fenotipagem de alto rendimento, Bland-Altman

Estimating plant height in castor bean using RPA-derived Digital Elevation Models from RGB images

Author: Myriam EL ADAS
Adviser: Dra. Simone Alves Silva

ABSTRACT

Morphological characterization of castor bean (*Ricinus communis* L.) remains a challenge due to its reliance on numerous qualitative and quantitative descriptors, which are often labor-intensive, time-consuming, subjective, and destructive. To overcome these limitations, this study evaluated the potential of Remotely Piloted Aircraft (RPA) equipped with RGB sensors of 20 MP as a high-throughput phenotyping tool for estimating plant height at different phenological stages. A field trial was conducted with two cultivars (IAC-80 and BRS-ENERGIA) and two lineages (UFRB-23 and UFRB-222) from the active germplasm bank of the Nucleus of Plant Breeding (NBIO/UFRB). Plant height and related growth parameters were measured across four phenological stages. RGB images were captured using a DJI Mavic 3 Enterprise M with a GSD of 1.84 cm/pix. Digital Elevation Models (DEM) and orthomosaics were generated using *Agisoft Metashape Educational*, and plant height estimates were extracted using the *FieldImageR* package in *R/QGIS*. The estimated and direct measurements of plant heights showed strong correlations at 105 DAS ($R = 0.95$, $p < 0.001$), 118 DAS, and 132 DAS ($R = 0.94$, $p < 0.001$). Bland-Altman analysis indicated high agreement at 133 DAS, with a bias of –0.07 m and narrow limits of agreement (0.10 to –0.24 m), aligning with the reproductive stage when plants exceeded 1.20 m. However, prediction accuracy was influenced by leaf density, canopy structure, flight GSD, and environmental conditions. Further studies are recommended to evaluate variable GSD across developmental stages to enhance model robustness.

Keywords: *Ricinus communis* L.; high throughput phenotyping; Bland-altman

INTRODUCTION

Phenotypic characterization is an important tool to assess variability within plant genetic resources along with molecular characterization. However, extensive phenotypic data is considered nowadays as a bottleneck for crop breeding and functional genomics research because this method is time-consuming, labor intensive, subjective, and frequently destructive to plants. Additionally, crop characteristics and yields often vary within a single farm area, emphasizing the need for site-specific analysis or precision farming techniques to maximize output. (SONG et al., 2021)

As a result, a wide range of innovative technologies and strategies are being developed to monitor crops and related field data. These advancements include the use of smart agriculture, precision agriculture, Remotely Piloted Aircrafts (RPA), wireless communication technologies, the Internet of Things (IoT), and smartphone applications tailored for agricultural use. When applied to breeding programs, these advanced technologies could serve as interesting tools for high-throughput phenotyping. Therefore, these tools can facilitate the phenotypic evaluation process by enhancing its efficiency in terms of time and data quality and quantity (SOUSSI et al., 2024).

The use of aerial images using satellite and RPA images in the Euphorbeaceae family is mainly done with *Hevea brasiliensis, Manihot esculenta.* However, there are only a few studies done with *Ricinus communis* L.. For example, yield prediction was performed using Sentinel-2A derived indices namely NDVI and EVI and linear regression in a semi-arid region of India (KUMAR et al., 2023). Infrared thermometer, and spectral radiometer were used to monitor stress in germplasm and yield prediction (KUMAR et al., 2005).

This study assesses the efficacy of drone-captured RGB image analysis as a high-throughput phenotyping technique to assist breeding activities of castor bean at the Nucleus of Genetic Improvement and Biotechnology (NBIO). Plant height is an important parameter in germplasm characterization, thus smaller crops are easier to harvest manually and mechanically. The objective of this study is to evaluate the potential of RPA-based data as a high-throughput phenotyping technique, and to elaborate a methodology to assess the accuracy of plant height estimation at different phenological stages at a fixed GSD of 1.84 cm/pix.

MATERIALS AND METHODS

1.1. Plant material

Two lineages, UFRB-23 and UFRB-222, were chosen for this study from the Active Lineage Germplasm Bank of UFRB/CCAAB/NBIO, based on their high yield. As well as two commercialized cultivars, IAC-80 and BRS-ENERGIA (Figure 3). Three seeds per pot were sown in the greenhouse on the 24 of April 2024, the plants were then thinned ten days after seedling emergence leaving only one plant per hole. Transplantation occured when the seedlings had reached 10 cm in height and a stem diameter of 5 cm, it's when seedlings with two complete leaves ready for planting in the field (Vm) (38 Days After Sowing or DAS) (GERVASIO, F. A. R. et al., 2016).



Figure 3. *The plant material used in the experiment: Genotypes, architecture, raceme, productivity (kg/ha) (NBIO, 2023)*

1.2. Study area

The study was conducted from april to october 2024 in the experimental fields of the CCAAB at *Universidade Federal Do Recôncavo da Bahia* (UFRB), in Cruz das Almas (BA), Brazil (12˚40'39" S, 39˚ 40' 23" W). The municipality is at an altitude of 220 meters and has an average temperature of 24.5˚C, relative humidity of 82%, and annual precipitation of 1,197 mm. According to the Köppen classification system, the climate of the region is a transition zone between Am (monsoon climate) and Aw (tropical climate with a dry winter season) (type C1), and it is dry and subhumid. The soil in the experimental field is classified as a Dystrophic Yellow Latosol A - moderate sandy clay texture (Embrapa, 1993).

Plowing was carried out using a moldboard plow, followed by transplanting on 29 May 2024. Base fertilization was carried out based on soil analysis, when transplanting, applying 15 Kg of Nitrogen per hectare, with ammonium sulfate as the source; 50 Kg of phosphorus per hectare from triple superphosphate; and 30 kg per hectare of potassium chloride. Weed control during the crop cycle was done using a weed whacker between lines and by manual weeding using a hoe around the plant before each RPA flight.

1.3. Experimental design

The experimental design was a randomized complete block design, with four genotypes, and six blocks, each plot consisting of five plants of the same genotype. Castor Bean is planted with 4 meters of row spacing and 1 meter of intra-row spacing. A buffer zone is planted surrounding the experiment, consisting of the UFRB-160 Castor Bean Lineage, and each plot was separated by a 3 meters spacing to avoid overlapping between genotypes (Figure 4).



Figure 4. *Overview of the study area in the experimental farm of UFRB. yellow: BRS-ENERGIA; blue: IAC-80, red: UFRB-222, green: UFRB-23; purple: UFRB-160.*

1.4. Meteorological data

The daily meteorological data were collected from the NASA POWER Data Access Viewer (DAV) website (https://power.larc.nasa.gov/data-access-viewer/). The extracted variables are date, mean temperature (°C), precipitation (mm), Mean Relative Humidity (%), and all sky surface Photosynthetically Active Radiation (PAR) Total.

1.5. Monitoring date

Field data collection and RPA image acquisition were scheduled according to the phenological stages of the castor bean plant (Table 1) as well as favorable climatic conditions. Phenological stages were monitored twice weekly, from the emergence of the primary raceme to the fruit maturation of the tertiary raceme. A total of 10 RPA flights were conducted. The first flight (V0) occurred before planting. Flight V1 took place during the initial growth stage, before the emergence of the primary raceme. Flights V2, V3, and V4 were conducted during the growth stage, coinciding with the emergence of the primary raceme. Flights V5, V6, V7, and V8 occurred during the production stage, marked by the emergence of the tertiary raceme. Finally, flight V9 was conducted during the maturation stage, when the leaves begin to fall and the fruits reach full maturity.

1.6. Field data acquisition and calculation

On the same day as the RPA image acquisition, direct field evaluations were carried out (Table 2).

Table 2. Summary of the growth descriptors evaluated and the RPA image acquisition dates

Flight date	Field evaluation	DAS	CD1	CD2	PH	NI	NL	SD	Stage
29/05/2024	✕	35	✕	✕	✕	✕	□	✕	Initial growth stage
13/06/2024	13/06/2024	51	□	□	□	✕	□	□	Initial growth stage
05/07/2024	06/07/2024	73	□	□	□	□	□	□	Growth stage
09/07/2024	10/07/2024	77	□	□	□	□	□	□	Growth stage
18/07/2024	18/07/2024	85	□	□	□	✕	□	✕	Growth stage
✕	24/07/2024	91	□	□	□	✕	✕	✕	Growth stage
01/08/2024	02/08/2024	100	□	□	□	✕	✕	✕	Production stage
07/08/2024	07/08/2024	105	□	□	□	✕	✕	✕	Production stage
21/08/2024	20/08/2024	118	□	□	□	✕	✕	✕	Production stage
03/09/2024	04/09/2024	132	□	□	□	✕	✕	✕	Production stage
✕	13/09/2024	142	□	□	□	✕	✕	□	Production stage
28/10/2024	29/10/2024	187	✕	✕	□	✕	✕	✕	Maturation

The following growth traits were measured for all 120 plants: number of leaves (NL), stem diameter (SD), number of internodes (NI), plant height (PH), largest crown diameter (CD1), perpendicular crown diameter (CD2), canopy area (CA), and canopy volume (CV). Given the elliptical shape of the castor bean canopy, CA was calculated using CD1 and CD2, while CV was estimated using plant height, CD1, and CD2 (OWEN, H. J. F., et al., 2024)

$$Canopy\ Area\ (m^2) = \pi \times \frac{CD1}{2} \times \frac{CD2}{2}$$

$$Canopy\ Volume\ (m^3) = \frac{4}{3}\pi \times \frac{CD1}{2} \times \frac{CD2}{2} \times \frac{AP}{2}$$

1.7. Phenological stage determination

Phenological stages were monitored twice weekly (Table 3), from the emergence of the primary raceme to the fruit maturation of the tertiary raceme.

The phenological stages (PS) are based on the four stages defined by Gervasio, F.A.R. *et al.* (2016), as described in Table 1. The substages (PSub) and the flower stage scale (Rscale) are newly developed descriptor (Table 4) based on the phenological stages of the castor bean plant described by Gervasio et al. (2016) and on the floral development described by CLASSEN-BOCKHOFF and FRANKENHÄUSER in their morphological study of castor bean flower structure (CLASSEN-BOCKHOFF; FRANKENHÄUSER, 2020).

Table 3. Summary of the phenology evaluation dates

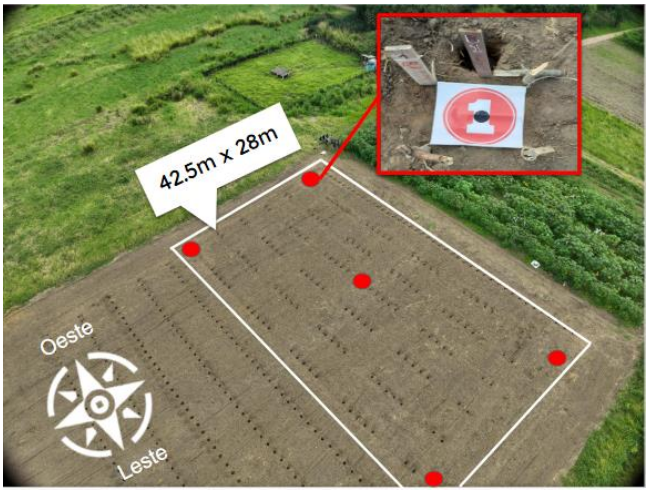
Evaluation date	DAS	Stage
13/06/2024	51	Initial growth stage
05/07/2024	72	Growth stage
09/07/2024	76	Growth stage
10/07/2024	77	Growth stage
16/07/2024	83	Growth stage
18/07/2024	85	Growth stage
23/07/2024	90	Growth stage
02/08/2024	100	Production stage
06/08/2024	104	Production stage
23/08/2024	121	Production stage
27/08/2024	125	Production stage
03/09/2024	132	Production stage
17/09/2024	146	Production stage

Table 4. Adapted phenological descriptors of castor bean genotypes used in this study

Stage (PS)	Substage (PSub)	Description	Scale (Rscale)
Initial Growth Stage	**Ve**	Cotyledons	**AP**: Appearance **AB**: Opening **ED**: in development **DC**: fully developed
	Vm	1-2 true leaves	
	Vo	3-5 true leaves	
Growth Stage *marked by the emergence of the first raceme*	Emergence of raceme **(E)**	Emergence of the panicle until its total opening	**000**: very small bud **00**: small bud **0**: maximum size before opening **1**: small opening **2**: carpellate flowers are visible **3**: Panicle half open **4**: Panicle entirely open
	Anthesis of the carpellate flowers **(A)**	Carpellate flowers open, the stylar arms are reddish or orange and spread backward	**0**: panicle is in a full conal shape, all flower buds are fully grown and ready to open **1**: initial opening of carpellate flowers **2**: half of carpellate flowers are open **3**: ¾ of carpellate flowers are open **4**: all carpellate flowers are open
	Fertilization **(F)**	Spike formation is marked by the differentiation of the long greenish hairs present on the gynoecium that become long and stiff. The spike starts showing from the base to the apex of the panicle.	**1**: initial spike formation **2**: up to 50% of the spikes are formed **3**: up to 75% of the spikes are formed **4**: up to 100% of the spikes are formed
Production Stage *marked by the grain formation of the first raceme*	Grain formation **(G)**	Capsule formation, the grains start to form leading to the increase in the size of the capsules, meanwhile the peduncle increases in length starting from bottom to top	**1**: Starting of grain formation **2**: 50% of peduncles are longer **3**: 75% of peduncles are longer **4**: 100% of peduncles are longer
Maturation Stage *marked by leaf fall and fruit maturation in tertiary racemes*	Fruit maturation **(M)**	The castor fruit is a schizocarp, typical regma. when the capsules reach maximum size, they start drying gradually until they are ready to be harvested	**1**: Stylar arms are dry, initial yellowing of the spikes **2**: Black points on capsules on spikes **3**: Capsules start showing cavities **4**: Raceme starts showing noticeable drying **5**: 100% of the fruits are dry

1.8. Aerial Image acquisition

Before starting image acquisition with the Remotely Piloted Aircraft (RPA), five Ground Control Points (GCPs) were placed, one at each of the four corners of the field and one at the center using fixed stakes (Figure 5.A). These stakes must be firmly fixed to the ground to prevent any movement, ensuring the consistency and accuracy of georeferencing during all flight dates. It is essential to select flat, stable, and open locations with good visibility, ensuring even distribution between the field's extremities and center. The GCP markers used were plastic targets (50x50 cm) with unique numbering. A mobile Real-Time Kinematic (RTK) system was employed prior to the first RPA flight to collect GPS points with real-time, centimeter-level accuracy (Figure 5.B).



A



B



C

Figure 5. *Ground Control Points (GCP) distribution in the field (A) and the RTK-GNSS system used to georeference the GCP (B), DJI mavic 3 Entreprise M used in this study(C)*

An initial flight (V0) was conducted before transplantation to assess plant height evolution in the Digital Elevation Model (DEM). Subsequently, nine additional flights were performed throughout crop development until maturation, corresponding to the following monitoring dates: June 13, July 7, July 9, July 18, August 1, August 7, August 21, September 4, and October 28 (Figure 6). Flight scheduling was dependent on weather conditions and RPA availability. All RPA flights were conducted at a fixed altitude of 40 meters above ground level, between 12:00 and 13:00. The flight dates were selected based on visual assessment of weather conditions, prioritizing the absence of cloud cover and precipitation, as well as low wind speeds at both plant and RPA level (<12 m/s). Wind conditions were evaluated by observing plant leaves; minimal leaf movement was considered ideal for flight.

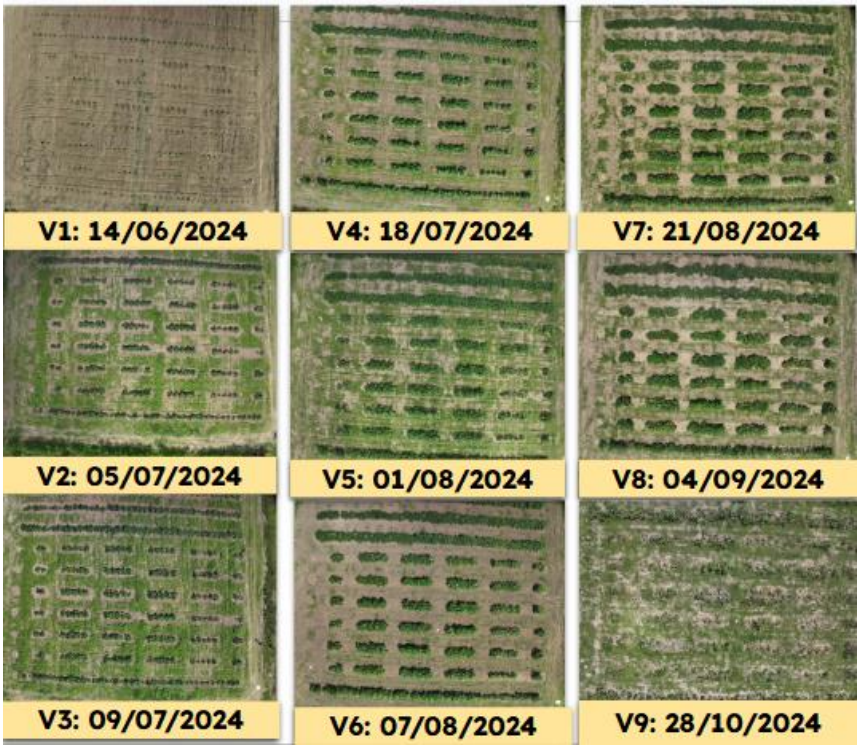


Figure 6. *Aerial image acquisition in 9 different flight dates.*

Images were captured using a DJI Mavic 3 Enterprise Multispectral (Figure 5.C)., equipped with both an RGB camera (Table 5) . The use of the DJI Pilot application facilitated flight planning, path control, and speed regulation during image acquisition. The same flight route and characteristics are used on all flights.

Table 5 . RGB camera characteristics of the DJI Mavic 3 Enterprise Multispectral

Bands	Resolution	FOV	GSD	Flight speed	Side overlap	Front overlap	Margin
RGB	20MP	84°	1.85 cm/pix	1.5 m/s	80%	90%	2

1.9. Digital Elevation Model (DEM) creation

Agisoft Metashape (Educational version) is used to generate the Digital Elevation Models (DEMs) and the orthomosaic for each flight using the images of the RGB camera. DEMs represent the elevation of the Earth's surface, it is a matrix data structure that contains pixel-specific elevation data. Whereas orthomosaic gathers reflectance data in each pixel. The resulting DEMs and orthomosaics are exported in raster format (.tif),

The methodology used for DEM and orthomosaic generation from RPA (Remotely Piloted Aircraft) data with Ground Control Points (GCPs) is based on the Agisoft HelpDesk Portal. The process begins by: (1) aerial images upload, (2) photos alignment, (3) Adjustment of the bounding box to reduce processing time, (4) optimize camera alignment and gradual selection, (5) load GCPs, and filter photos by GCPs, also known as markers, (6) generate a high quality point cloud, (7) Classify vegetation and soil by color, (8) build DEM from point cloud (9) build orthomosaic based on DEM surface data (10) Export DEM and orthomosaic.

1.10. Extraction of Plant height using DEM

In order to extract plant height, the FIELDimageR package (MATIAS et al., 2020) in the QGIS Software (R DEVELOPMENT CORE TEAM, 2021) is used.

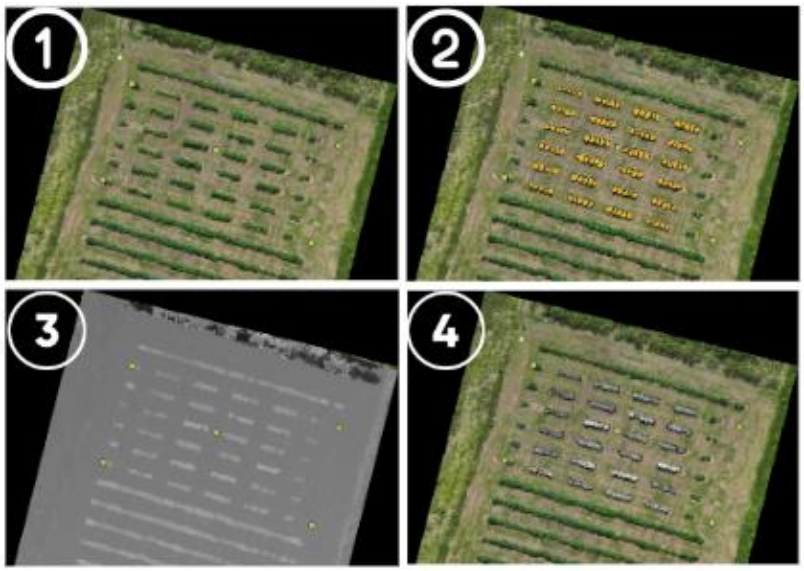


Figure 7. *Plant height extraction using FieldImageR package on QGIS.*

(1)*Add GCP (yellow points) to the raster; (2) Add a shapefile using polygons to delimit the plant area; (3) Create height raster using FieldHeight function; (4) Extract maximum height for each plant. (source : Author)*

A polygon shapefile is created to identify and delimit each plant within plots based on the orthomosaic. The created polygons must be validated using the *Check validity tool*. FieldHeight function is used to calculate the Canopy Height Model (CHM) by calculating the difference of elevation before plantation and the date of the aerial image acquisition. The resulting CHM raster is then clipped by the polygon vector. Then maximum height values per plant are extracted from the CHM raster using the *Zonal statistics* function (Figure 7).

1.11. Statistical analysis

To identify the best phenological stage for estimating plant height using RPA images, the estimated plant height within each flight is compared with direct field measurements. First a Pearson correlation analysis shows if there is a relationship between the values of the two methods. Then the Bland-Altman method is used as an approach for evaluating agreement between two quantitative measurement techniques, including estimated and measured techniques. This method helps detect any systematic bias, defined as the mean difference between the two methods, and calculates the limits of agreement: the superior limit of agreement (SLoA), equal to the bias + 1.96 x the standard deviation (SD), and the inferior limit of agreement (ILoA), equal to the bias - 1.96 x SD. These limits indicate the range within which 95% of the differences are expected to fall, reflecting the typical variation between the two methods (BLAND, J. M.; ALTMAN, D. G., 1986) (HIRAKATA; CAMEY, 2009).

RESULTS

2.1 Climatic conditions

During the crop growing season, from June to October 2024, climatic conditions showed moderate variability across all measured parameters (Figure 8).

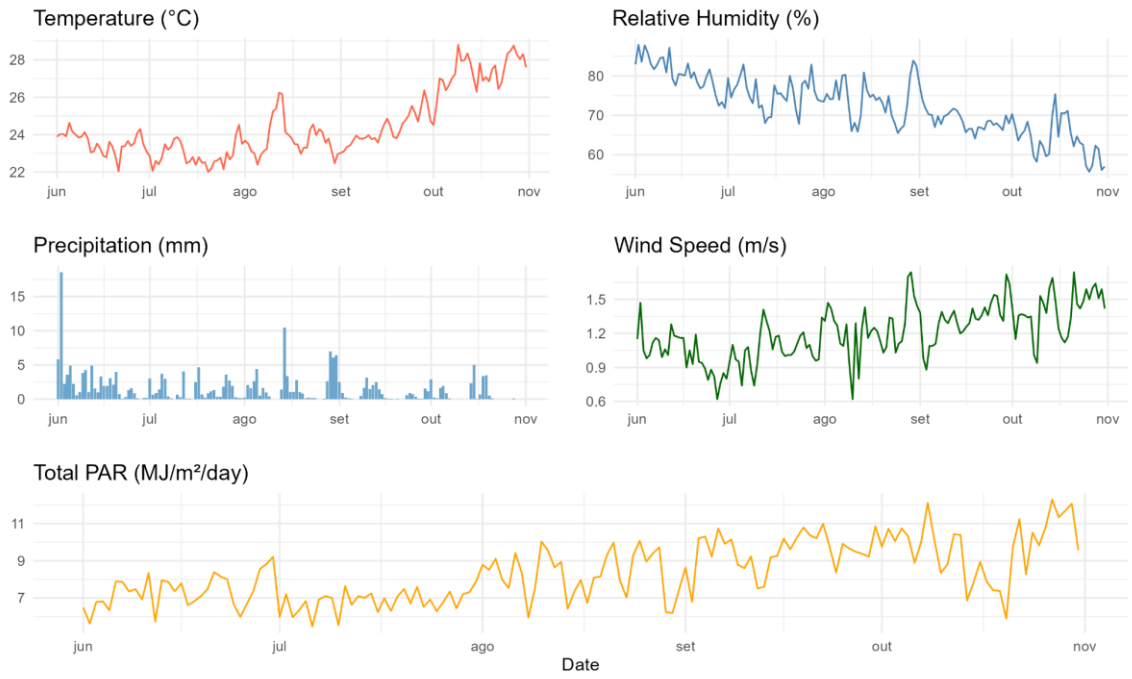


Figure 8. *Daily average temperature, relative humidity, precipitation,wind speed at 2 meters height, and all sky surface photosynthetically active radiation (PAR) total, through the growing season.*

According to the meteorological data extracted from the *NASA POWER Data Access Viewer (DAV)* website, temperature ranged from 22.01°C to 28.80°C, with a mean temperature of 24.39°C. The relative humidity ranged from 55.66% to 87.89%, with a mean of 72.46%, indicating generally humid conditions. Precipitation levels were highly variable, ranging from 0 mm to a maximum of 18.57 mm/day. The wind speed at 2 meters height remained relatively stable throughout the period, with values ranging from 0.62 m/s to 1.74 m/s. Regarding radiation, the total photosynthetically active radiation (PAR) measured at the surface ranged from 5.46 MJ/m²/day to 12.29 MJ/m²/day, with a mean of 8.32 MJ/m²/day.

2.2 Flight parameters

Although the experiment was carried out during the winter season, which is typically characterized by frequent rainfall and strong winds in the region, it was still possible to successfully complete nine flights throughout the experimental period. Table 6 presents the meteorological conditions recorded during image acquisition at 12:00-13:00h.

Table 6. Climatic conditions during image acquisition between 12h and 13h

Flight date (DAS)	Temperature (°C)	Relative Humidity (%)	Wind speed at 2 meters (m/s)	Wind speed at 40 meters (m/s)	Precipitation (mm)	Hourly PAR (MJ/m²/hour)
51	28.44	49.26	2.0	5.2	0.47	1.1
73	28.74	52.42	1.31	3.17	0.34	0.97
77	29.45	46.3	1.97	4.97	0.12	0.97
85	29.6	40.13	1.69	4.21	0.09	0.76
100	30.21	42.88	2.16	5.43	0.28	1.17
105	29.76	45.45	1.39	3.49	1.58	1.21
118	30.91	33.36	1.74	4.19	0.0	1.4
132	31.42	37.28	1.66	3.98	0.0	1.47
187	36.1	32.3	1.74	4.03	0.0	1.55

Temperatures ranged from 28.44°C to 36.10°C, with the highest temperature observed on October 28th, indicating a seasonal transition toward warmer conditions. Relative humidity varied between 32.3% and 52.42%, generally decreasing over time, particularly from August onward (118 DAS). Wind speed was recorded at two heights: 2 meters (plant level) and 40 meters (flight altitude). At 2 meters, wind speeds ranged from 1.31 to 2.16 m/s, suggesting mild ground-level wind conditions. At 40 meters, wind speeds were consistently higher, ranging from 3.17 to 5.43 m/s, yet still within safe

operational limits for RPA flights (<12m/s). Precipitation levels were minimal or absent on most flight dates, with no rainfall recorded on the final three flights. The highest precipitation (1.58 mm) occurred on August 7th, although conditions at flight time remained within acceptable thresholds. Finally, the Photosynthetically Active Radiation (PAR) integrated over the 12:00-13:00 period, representing light availability, ranged from 0.76 to 1.55, reflecting generally favorable lighting conditions for aerial imaging, especially during the later flights with minimal cloud cover and higher solar angle.

These data confirm that, despite the experiment taking place during the winter and early spring, periods typically associated with rain and wind in the region, the selected flight windows provided acceptable environmental conditions for aerial data acquisition according to the user manual of the aircraft (DJI, 2023). The resulting DEM showed a very high Ground sample distance (GSD) (Table 7) ranging from 2.19 to 2.24 cm/pix which represents a field area of 4.7961 to 5.0176 cm^2. Differences in DEM dimension and size is due to manual delimitation of the bounding box during images processing, however these parameters don't affect the accuracy of the height data.

Table 7. Summary of flight parameters and information on DEM processing.

Flight date (DAS)	N° of images	DEM dimension	DEM GSD	DEM size
51	71	3.689 x 3.943	2.24 cm/pix	34.58 MB
73	75	3.590 x 4.099	2.22 cm/pix	33.26 MB
77	75	3.436 x 3.724	2.26 cm/pix	29.35 MB
85	71	3.490 x 3.664	2.2 cm/pix	31.11 MB
100	71	3.516 x 3.864	2.2 cm/pix	34.72 MB
105	41	3.611 x 3.835	2.19 cm/pix	31.77 MB
118	72	3.602 x 3.805	2.19 cm/pix	32.77 MB
132	74	3.491 x 3.618	2.19 cm/pix	29.73 MB
187	71	3.631 x 3.899	2.23 cm/pix	30.99 MB

2.3 Phenological stages

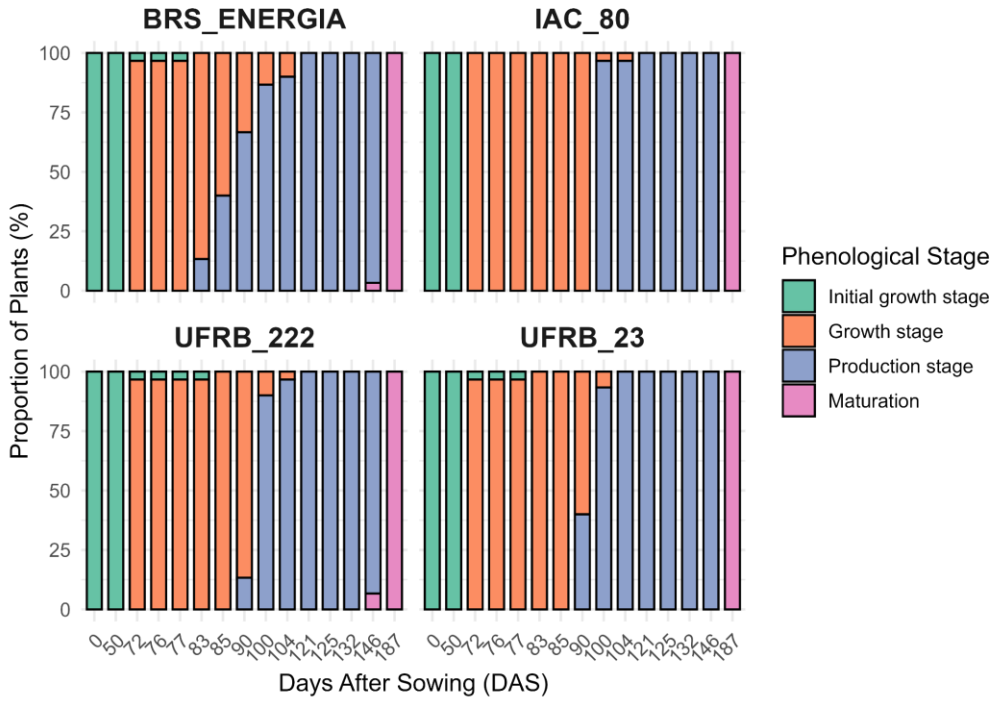


Figure 9. *Length of the growing cycle expressed in DAS (Days after Sowing) in castor bean.*

The length of the main phenological stages for primary racemes is shown in Figure 9 above. Based on the proportion of plants in each phenological stage over time, the genotypes showed distinct developmental behaviors. Considering that a genotype is in a given stage when 50% or more of the plants have reached it, BRS-ENERGIA was the earliest to reach the production stage (blue) near 90 DAS. UFRB-222, UFRB-23 and IAC-80 entered the production stage at 100 DAS. These results confirm the fact that the cultivar BRS-ENERGIA is an early-maturing genotype, while the other genotypes have a mid-maturing genotype.

2.4 Canopy area and volume

UFRB-23 showed the highest canopy area and volume during the whole cycle, followed by UFRB-222 and IAC-80. The cultivar BRS-ENERGIA had the lowest canopy area and volume, likely due to its erect growth habit. On the other hand, UFRB-23 and IAC-80 both have a semi-erect stature, whereas UFRB-222 is known for its open plant architecture (Figure.10–11)

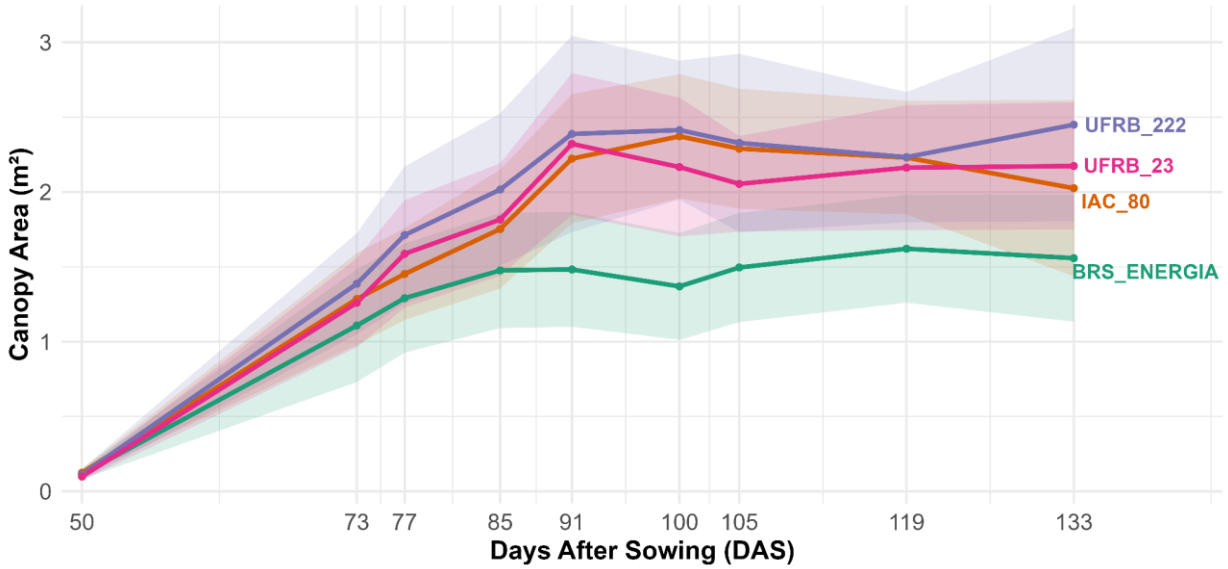


Figure 10. *Calculated canopy area evolution based on field measurements.*

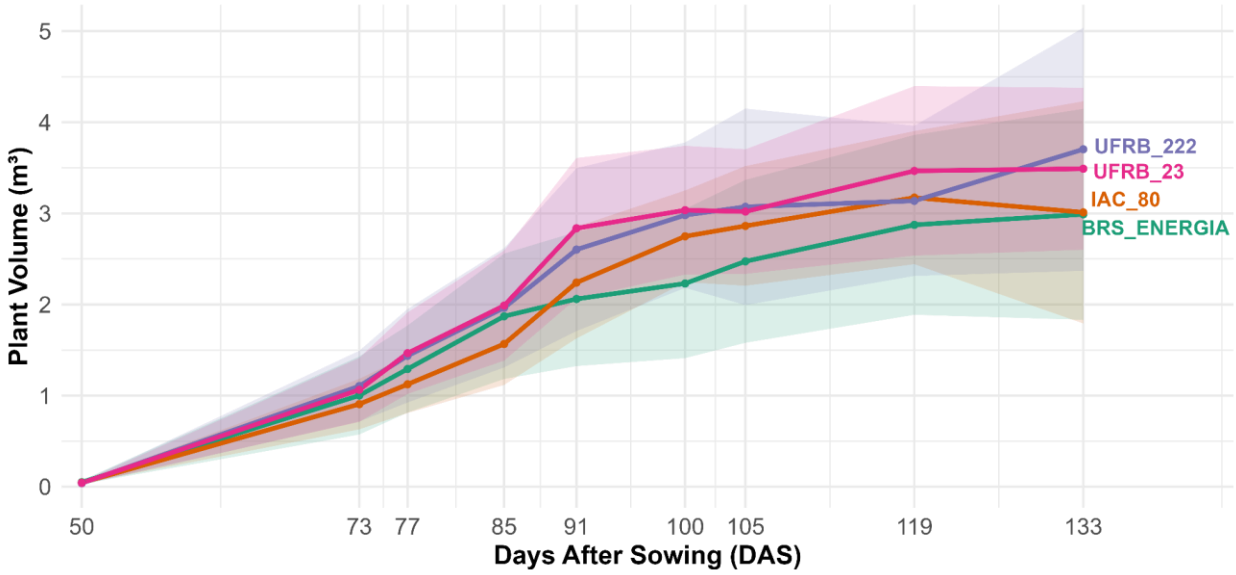


Figure 11. *Calculated canopy volume evolution based on field measurements.*

2.5 Direct measurement of plant height

Plant height, obtained through direct field measurements, showed significant differences among genotypes within each evaluation date (DAS), confirming distinct growth rates between genotypes. Furthermore, the inclusion of block effects revealed significant spatial variation across experimental units. The genotype BRS-ENERGIA exhibited the greatest plant height, followed by UFRB-23. In contrast, UFRB-222 and IAC-80 presented lower plant heights (Figure 12).

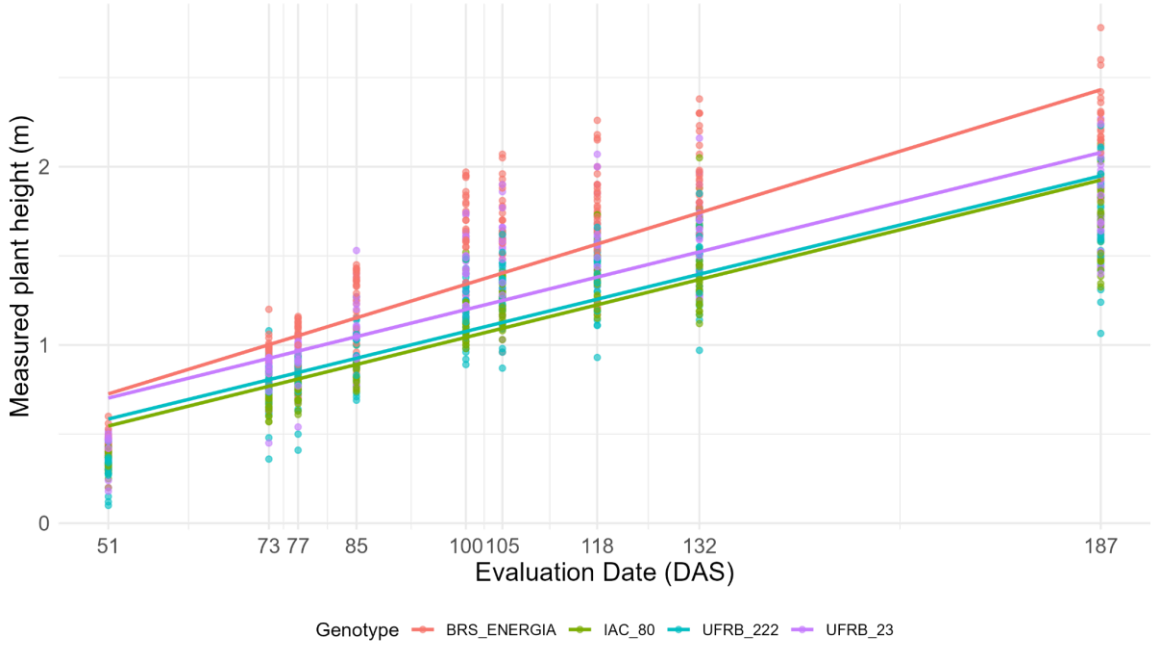


Figure 12. *Linear Regression of Plant Height Over Time for Four Castor Bean Genotypes*

2.6 Agreement between estimated and measured plant height

The figure 13 and 14 below show the Pearson Correlations and Bland-Altman agreement between the estimated and the direct measurement of castor bean plant height for each flight and considering all genotypes.

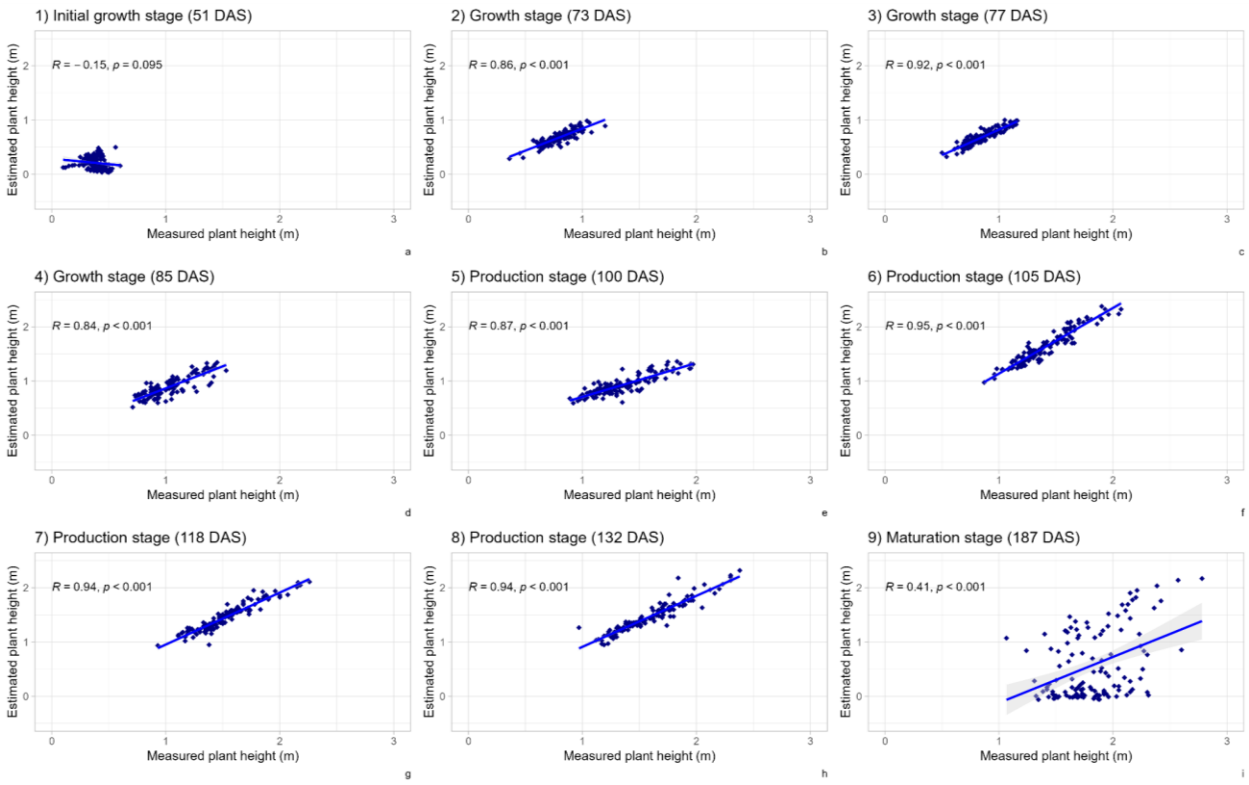


Figure 13. *Pearson correlations between estimated and direct measurements of plant height within each RPA flight.*

Very low correlation was observed during the first flight at 51 days after sowing (DAS) (r = -0.15, p = 0.095), which corresponds to the initial growth stage. At this stage, plant height ranged from 0.10 to 0.60 meters, and the number of leaves varied between 5 and 8 across all genotypes. During the vegetative growth stage, plant height increased to a range of 0.50 to 1.40 meters, with the development of broader leaves. Strong correlations were observed at 73 DAS (r = 0.86, p < 0.001), 77 DAS (r = 0.92, p < 0.001), and 85 DAS (r = 0.84, p < 0.001). In the production stage, plant height ranged from 0.90 to 2.30 meters, and high correlations were also recorded at 100 DAS (r = 0.87, p < 0.001), 105 DAS (r = 0.95, p < 0.001), 118 DAS and 132 DAS (r = 0.94, p < 0.001). At the maturation stage (188 DAS), a moderate correlation was observed (r = 0.41, p < 0.001), with plant height varying from 1.00 to 2.70 meters, and most leaves having already fallen.

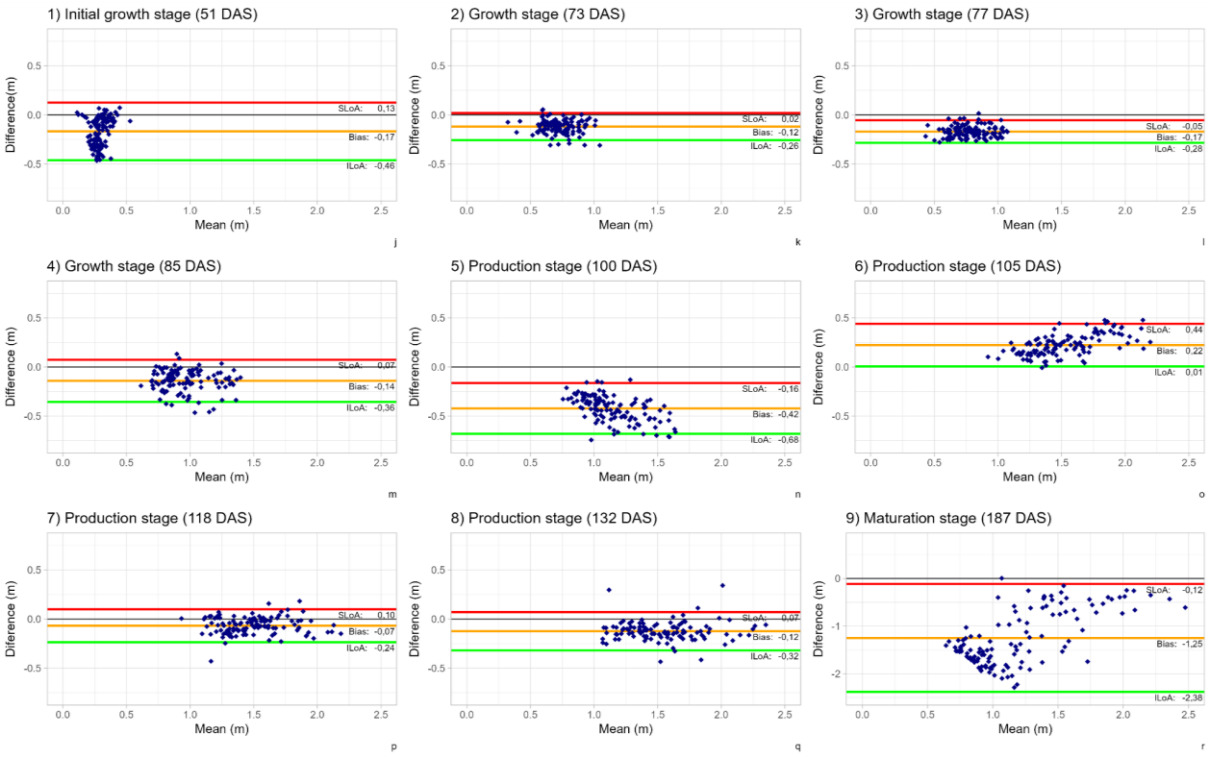


Figure 14. *Bland-Altman agreement graphs of estimated and direct measurements of plant height within each RPA flight.*

As shown in the Figure 14, at the initial growth stage, the mean difference between estimated and directly measured plant height is -0.17 meters, which means that on average estimated plant height measures 0.17 meters less than direct measurement, with an inferior limit of agreement of 0.46 meters and a superior limit of agreement of 0.13 meters. The graph (i) shows a tendency where lower plant heights (between 0.2 and 0.4 meters) tend to be underestimated with an increased variability in plant height measures, which makes the estimated measurements less reliable.

At the growth stage, all flight dates (73 DAS, 77 DAS, 85 DAS) showed a tendency to underestimate plant height, with a bias of -0.12, -0.17 and -0.14 meters less than directly measured plant height. At 85 DAS, the graph (l) demonstrated a higher underestimation at 1.25 meters of plant height.

At the production stage, disagreement between the two methods of measurement was mostly observed at 100 DAS, 105 DAS and 132 DAS, however with different

tendencies. The highest bias (-0.42 meters) was observed at 100 DAS, with a tendency to underestimate with increasing plant height starting at 1 meter. However, at 105 DAS, the estimated plant height was overestimated in general but started increasing at 1.75 meters of plant height with a bias of 0.22 meters. At 132 DAS, the bias was more acceptable than the other flight dates, with a value of -0.12 meters, estimated plant height was also underestimated with an inferior limit of agreement of -0.32 meters. At 118 DAS was observed a tendency of agreement between the two methods, where the graph points are starting to be equally distributed above and below the line of identity (y=0) with a bias of -0.07 meters, which demonstrates very low mean difference between the measurement methods.

Finally, at maturation stage (187 DAS), estimated measurements tend to underestimate plant height with a bias of -1.25 meters, however the estimated measurements tend to agree with direct measurements for higher plant heights starting 1.5 meters.

In order to identify the optimal plant height where the two methods demonstrate an agreement, another bland-altman graph was created for each phenological stage (Figure 15). Between all four phenological stages, the production stage, observing the plot's tendencies, an agreement is observed at a plant height range of 1.2 meters and above where the points are equidistant from the line of identity (y=0).

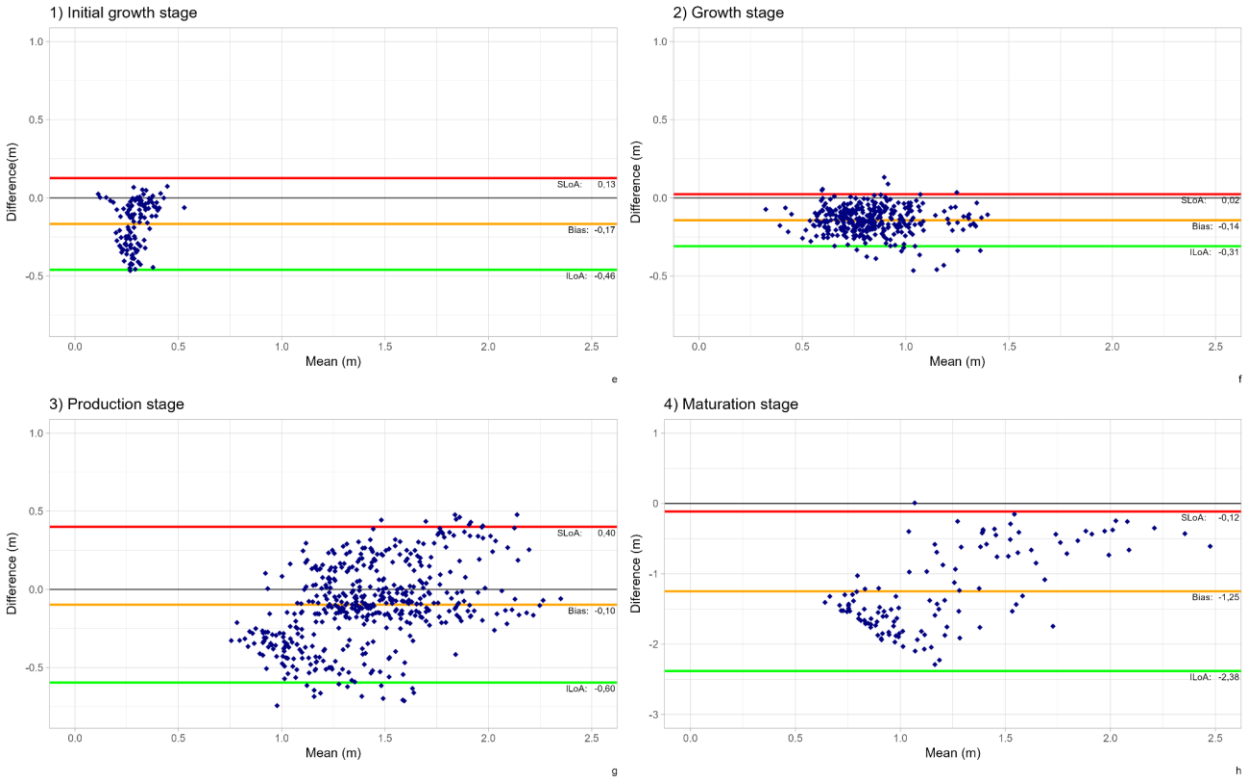


Figure 15. *Bland-Altman agreement graphs of estimated and direct measurements of plant height within each phenological stage.*

DISCUSSION

As shown in Figure 13, a strong correlation (r ranging from 0.84 to 0.95, $p < 0.001$) was observed during flights conducted at the growth stage (73, 77, and 85 DAS) and the production stage (100, 105, 118, and 132 DAS). In contrast, very low correlation was detected at the initial growth stage (51 DAS), where the correlation coefficient was negative (r = –0.15, $p = 0.095$). At this early stage, plant height ranged between 0.1 and 0.6 meters, and individual plants typically had only 5 to 8 small leaves. Similar trends were observed in cassava studies, where RPA-based measurements taken at 30 and 40 meters showed moderate to high correlations at the elongation stage (r = 0.61) and late bulking stage (r = 0.92), indicating improved correlation when plants exceeded 1 meter in height (SELVARAJ, M.G., et al., 2020). At the maturation stage, a moderate correlation was found (r = 0.41, $p < 0.001$) between estimated and directly measured plant heights. Despite the plants being tall at this stage, the reduced canopy structure caused by leaf

drop likely limited the number of surface points available for drone sensors, thus reducing measurement accuracy. According to GAO *et al.* (2022), maize stalks at maturity are thin and tend to sway in the wind, which can result in a noisier point cloud and increased error in plant height estimation using RPAs.

To further evaluate the agreement between the two measurement methods, a Bland–Altman analysis was performed (Figure 14). In general, RPA-based estimates of plant height at a GSD of 1.84 cm/pix (40 m flight altitude) tended to underestimate the actual plant height of castor bean across various flight dates. Similar findings were reported in cassava, where Bland–Altman analyses conducted at different altitudes (20, 30, 40, and 60 meters) consistently showed underestimation for actual plant heights between 2.00 and 3.00 meters (Nascimento et al., 2024). Among these, the 20-meter flight altitude provided the best agreement across altitudes (NGUYEN et al., 2023). Notably, at 118 DAS, which corresponds to the production stage of castor bean, although measurements were underestimated, RPA estimates showed good agreement with direct measurements when plant height was above 1.2 meters (ŠIMUNOVIĆ; MANDIĆ, 2015). When flight data were grouped by phenological stage (Figure 15), the Bland–Altman analysis confirmed that RPA-based plant height estimation during the production stage is reliable, especially when actual plant height exceeds 1.2 meters.

CONCLUSION

Overall, the results show that RPA-based estimation of plant height in castor bean with a DJI Mavic 3 Enterprise Multispectral with a GSD of 1.84 cm/pixel at 40 m of flight altitude, is most reliable in the production stage, when plants exceeded 1.2m of height and canopies were developed and with broader leaves. In contrast, early growth and maturation showed reduced accuracy due to sparser canopies and structural variability. These findings reinforce that phenology, canopy structure, and GSD must be planned together for RPA phenotyping in breeding and crop-monitoring contexts.

Comparing direct measurement and RPA estimation

In our experimental block (0.12 ha; 120 plants), the full RPA workflow took ~6 h 30 min (≈1 h acquisition + 2 h 30 min processing + 3 h height extraction), whereas direct field measurement required ~4 h (≈3 h in the field + 1 h tabulation). Although the direct method is faster, it is subjective and susceptible to fatigue, while the RPA approach is systematic but its performance varies with plant height and canopy density.

GSD effect on DEM quality

The accuracy in our height maps depends on how big each image pixel is on the ground (GSD). Smaller pixels show more detail; larger pixels blur small features like the top of a plant. When the pixels are too large, plant tops look flatter and the model underestimates height. To avoid this, the parts we want to measure should span several pixels. Because GSD is a function of sensor pixel size, focal length, and flight altitude, reproducibility across cameras is best achieved by specifying a target GSD and computing the altitude for each sensor to hit that target.

Main causes of under-/over-estimation

- Climatic conditions (especially wind): leaf/stem motion during acquisition causes blur and canopy “shrinkage” in the DEM (underestimation)

- Plant phenology and structure: sparse early canopies expose soil and increase DTM leakage (over/underestimation, depending on ground filtering); dense, closed canopies hide the ground, pushing the DTM upward (underestimation of height).
- Image processing choices (e.g., Gradual Selection): aggressive thresholds on reprojection error/reconstruction uncertainty can remove valid high canopy tie points (underestimation); insufficient outlier filtering leaves aerial “spikes” or mismatches (overestimation).

Recommendations

Use stage-specific target GSDs, standardize flight plan for all acquisition dates, and if possible capture the bare ground once before emergence to create the DTM from bare soil to stabilize CHM (DSM–DTM) across dates. Future work should determine the optimal GSD per phenological stage rather than altitude alone and quantify how acquisition and processing parameters trade off between processing time and measurement accuracy.

REFERENCES

AgiSoft Helpdesk Portal. Aerial data processing (with GCPs) - Orthomosaic&DEM generation. URL: (https://agisoft.freshdesk.com/support/solutions/articles/31000153696-aerial-data-processing-with-gcps-orthomosaic-dem-generation). Accessed on: 7 october 2025.

BLAND, J. M.; ALTMAN, D. G. Statistical methods for assessing agreement between two methods of clinical measurement. Lancet (London, England), **1986**, v. 1, n. 8476, p. 307–310.

CLASSEN-BOCKHOFF, Regine; FRANKENHÄUSER, Hebert. The 'Male Flower' of Ricinus communis (Euphorbiaceae) Interpreted as a Multi-Flowered Unit. Frontiers in Cell and Developmental Biology, **2020,** v. 8, p. 525561. DOI: https://doi.org/10.3389/fcell.2020.00313

Gao, M.; Yang, F.; Wei, H.; Liu, X. Individual Maize Location and Height Estimation in Field from UAV-Borne LiDAR and RGB Images. Remote Sens. **2022**, 14, 2292. https://doi.org/10.3390/rs14102292

GERVASIO, F. A. R. et al. Method and phenological characterization of the stadiums and phases of the development of castor bean plants. *African Journal of Agricultural Research*, **2016**, v. 11, n. 44, p. 4488–4497. DOI: https://doi.org/10.5897/AJAR2016.11337.

HIRAKATA, V. N.; CAMEY, S. A. Análise de Concordância entre Métodos de Bland-Altman. Clinical and Biomedical Research, **2009**, v. 29, n. 3. URL: (https://seer.ufrgs.br/index.php/hcpa/article/view/11727). Acessed on: 10 october 2025.

HUSSEIN, K. W. Review on Reproductive Biology of Caster bean (Ricinus communis L.). Journal of Ecology and Natural Resources, v. 6, n. 1, **2022**. URL: (https://medwinpublishers.com/JENR/review-on-reproductive-biology-of-caster-bean--(ricinus-communis-l.).pdf) Acessed on: 6 jun. 2025.

MAES, W. H. Practical guidelines for performing UAV mapping flights with snapshot sensors. Remote Sensing, Basel, v. 17, n. 4, 606, 2025. DOI: https://doi.org/10.3390/rs17040606.

MATIAS F. I.; CARAZA-HARTER, M. V.; ENDELMAN, J. B. FIELDimageR: An R package to analyze orthomosaic images from agricultural field trials. The Plant Phenome Journal, **2020**, v. 3, n. 1, p. e20005. DOI: https://doi.org/10.1002/ppj2.20005

Nascimento, J.H.B.; Cortes, D.F.M.; Andrade, L.R.B.d.; Gallis, R.B.d.A.; Barbosa, R.L.; Oliveira, E.J.d. High-Throughput Phenotyping for Agronomic Traits in Cassava Using Aerial Imaging. Plants **2025**, 14, 32. https://doi.org/10.3390/plants14010032

OWEN, H. J. F.; LINES, E. R. Common field measures and geometric assumptions of tree shape produce consistently biased estimates of tree and canopy structure in mixed Mediterranean forests. Ecological Indicators, **2024**, v. 165, p. 112219.

Pawar P., Matias F.I. FIELDimageR-QGIS. URL: (https://github.com/pspawar71/FIELDimageR-QGIS). Accessed on: 7 october 2025.

Selvaraj, M.G.; Valderrama, M.; Guzman, D.; Valencia, M.; Ruiz, H.; Acharjee, A. Machine learning for high-throughput field phenotyping and image processing provides insight into the association of above and below-ground traits in cassava (Manihot esculenta Crantz). Plant Methods **2020**, 16, 87.

CHAPTER 2: Phenological modeling of castor bean based on RPA-derived vegetation indices

CRUZ DAS ALMAS-BA
2025

Modelagem fenológica da mamoneira com base em índices de vegetação derivados de ARP

Autora: Myriam EL ADAS
Orientadora: Dra. Simone Alves Silva

RESUMO

Avanços em sensoriamento remoto com Aeronaves Remotamente Pilotadas (ARP) têm possibilitado o monitoramento rápido e não destrutivo de características das plantas por meio de imagens RGB e multiespectrais. Esses dados são frequentemente transformados em índices de vegetação (IVs), que atuam como proxies para biomassa, teor de clorofila, saúde das plantas e desenvolvimento da cultura. Este estudo teve como objetivo avaliar o desempenho de modelos lineares e não lineares de crescimento ajustados a IVs derivados de imagens de ARPs para descrever o desenvolvimento fenológico de *Ricinus communis* L. O experimento de campo foi conduzido com duas cultivares (IAC-80 e BRS-ENERGIA) e duas linhagens (UFRB-23 e UFRB-222). Os voos com ARP foram realizados com um DJI Mavic 3 Enterprise Multispectral equipado com câmeras RGB e multiespectral. Os índices de vegetação foram calculados com base nas bandas Vermelha, Verde, Azul, RedEdge e Infravermelho Próximo (NIR), utilizando o pacote *FieldImageR* no R. Seis modelos de regressão foram testados, com seleção baseada no AIC e nos pesos de Akaike. Os modelos quadrático e exponencial demonstraram maior estabilidade de ajuste, enquanto modelos mais complexos, como Gompertz e Richards, apresentaram falhas de convergência em casos de baixa variância. Os valores de R^2 variaram entre 0,63 e 0,76. As curvas ajustadas refletem com precisão os principais estágios fenológicos observados em campo. Os resultados confirmam o potencial dos IVs derivados de ARPs, especialmente GLI e RGBVI, para modelagem fenológica da mamona.

Palavra-chaves: *Ricinus communis L.*; fenotipagem de alto rendimento; modelos não lineares

Phenological modeling of castor bean based on RPA-derived vegetation indices

Author: Myriam EL ADAS
Advisor: Dra. Simone Alves Silva

ABSTRACT

Advancements in RPA-based remote sensing have enabled rapid, non-destructive monitoring of plant traits using RGB and multispectral imagery. These data are often transformed into vegetation indices (VIs), which serve as proxies for biomass, chlorophyll content, plant health, and crop development. This study aimed to evaluate the performance of regression growth models fitted to VIs derived from RPA imagery for describing phenological development in *Ricinus communis* L. A field experiment was conducted with two cultivars (IAC-80 and BRS-ENERGIA) and two lineages (UFRB-23 and UFRB-222). RPA flights were carried out using a DJI Mavic 3 Enterprise Multispectral equipped with RGB and multispectral cameras. Vegetation indices were calculated using reflectance data from Red, Green, Blue, RedEdge, and Near-Infrared (NIR) bands. Six linear and nonlinear models were tested, and model selection was based on AIC and Akaike weights. Quadratic and exponential models exhibited the highest fitting stability, successfully modeling all genotype × VI combinations. In contrast, more complex models like Gompertz and Richards frequently failed to converge, particularly under low data variance. R^2 values ranged from 0.63 to 0.76, indicating moderate model fit. The fitted curves captured key phenological transitions observed in the field, particularly the vegetative peak and senescence onset. These results demonstrate the potential of RPA-derived vegetation indices, particularly GLI and RGBVI, for modeling castor bean phenology using robust nonlinear approaches.

Keywords: *Ricinus communis L.*; high throughput phenotyping; nonlinear models

INTRODUCTION

Phenotypic characterization is an important tool to assess variability within plant genetic resources along with molecular characterization. However, extensive phenotypic data is considered nowadays as a bottleneck for crop breeding and functional genomics research because this method is time-consuming, labor intensive, subjective, and frequently destructive to plants. Additionally, crop characteristics and yields often vary within a single farm area, emphasizing the need for site-specific analysis or precision farming techniques to maximize output. (SONG et al., 2021)

As a result, a wide range of innovative technologies and strategies are being developed to monitor crops and related field data. These advancements include the use of smart agriculture, precision agriculture, Remotely Piloted Aircrafts (RPA), wireless communication technologies, the Internet of Things (IoT), and smartphone applications tailored for agricultural use. When applied to breeding programs, these advanced technologies could serve as interesting tools for high-throughput phenotyping. Therefore, these tools can facilitate the phenotypic evaluation process by enhancing its efficiency in terms of time and data quality and quantity (SOUSSI et al., 2024).

Plant spectral reflectance is a commonly used remote sensing technique that relies on empirical data acquisition and processing, rather than requiring in-depth physiological understanding. The analysis of remotely measured reflected light informs about plant-stress conditions and photosynthetic status. Recent advancements in remote sensing technology, particularly the development of multispectral images, offer a high-throughput method for crop growth and yield prediction. Multispectral images provide rich spectral information through 3-10 bands, enabling the creation of vegetation indices (VI). Utilizing predictive modeling approaches based on these VIs allows for simulating the relationship between spectral patterns and final crop growth and yields. This approach capitalizes on the globally available and cost-effective spatial-spectral-temporal information provided by remote sensing images. While the potential of the spectral reflectance technique as a high-throughput phenotyping tool is promising, its current application is in the early stages and necessitates additional technical and logistical advancements (FILELLA I. et al., 2023); (LLORENÇ CABRERA-BOSQUET et al., 2023); (QIAO, M. et al., 2023). The use

of aerial images using satellite and RPA images in the Euphorbiaceae family is mainly done with *Hevea brasiliensis, Manihot esculenta.* However, there are only a few studies done with *Ricinus communis* L.. For example, yield prediction was performed using Sentinel-2A derived indices namely NDVI and EVI and linear regression in a semi-arid region of India (KUMAR et al., 2023). Infrared thermometer, and spectral radiometer were used to monitor stress in germplasm and yield prediction (KUMAR et al., 2005).

The objective of this study is to evaluate the feasibility of modeling crop phenology using vegetation indices derived from RGB and multispectral images captured by Remotely Piloted Aircraft (RPA). Specific objectives of this study are : (1) to identify the most suitable growth model for fitting phenological curves of castor bean genotypes using vegetation indices; (2) to evaluate the opportunities and limits of non linear growth modeling using vegetation indices for further future studies.

MATERIALS AND METHODS

1.1. Plant material

Two lineages, UFRB-23 and UFRB-222, were chosen for this study from the Active Lineage Germplasm Bank of UFRB/CCAAB/NBIO, based on their high yield. As well as two commercialized cultivars, IAC-80 and BRS-ENERGIA (Figure 3). Three seeds per pot were sown in the greenhouse on the 24 of April 2024, the plants were then thinned ten days after seedling emergence leaving only one plant per hole. Transplantation occurred when the seedlings had reached 10 cm in height and a stem diameter of 5 cm, it's when seedlings with two complete leaves ready for planting in the field (Vm) (38 Days After Sowing or DAS) (GERVASIO, F. A. R. et al., 2016).

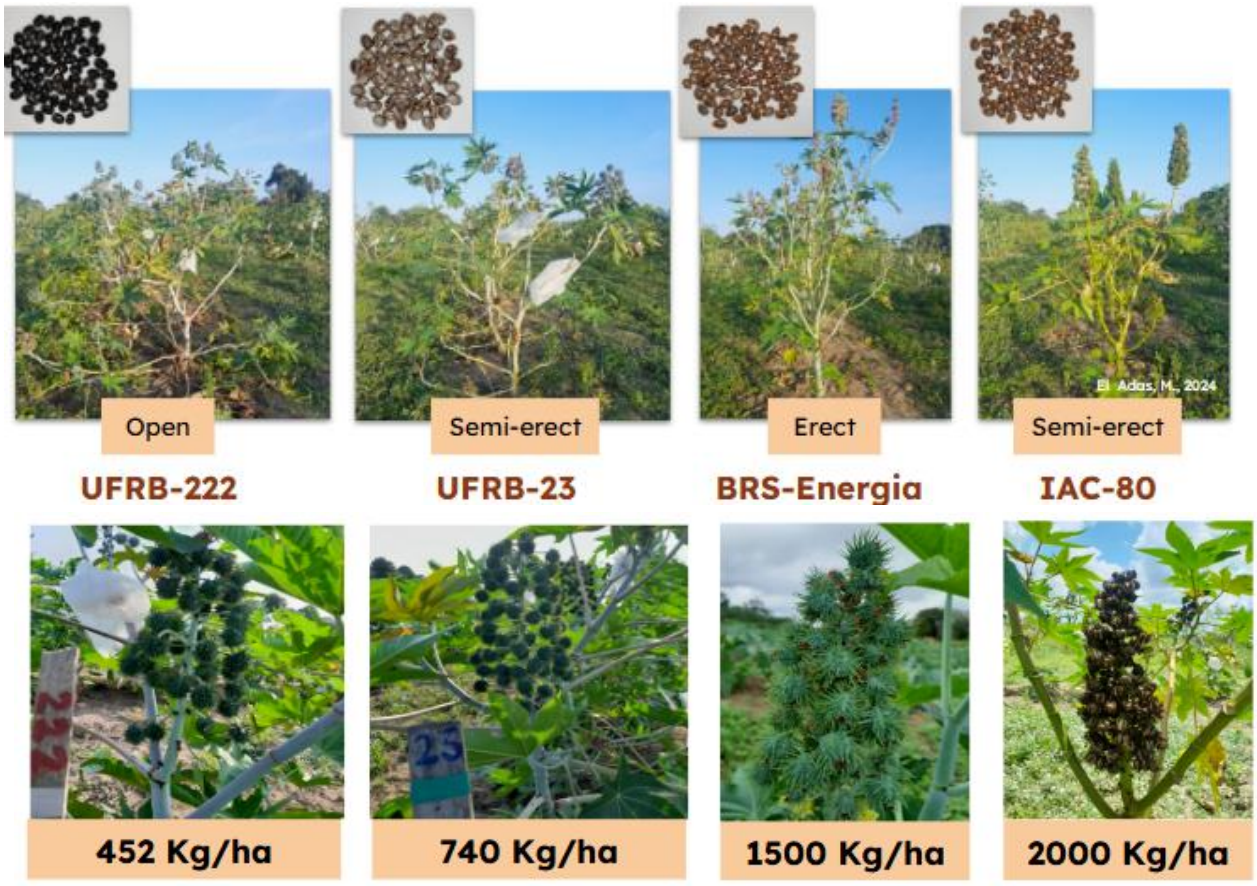


Figure 3. *The plant material used in the experiment: Genotypes, architecture, raceme, productivity (kg/ha) (NBIO, 2023)*

1.2. Study area

The study was conducted from april to october 2024 in the experimental fields of the CCAAB at *Universidade Federal Do Recôncavo da Bahia* (UFRB), in Cruz das Almas (BA), Brazil (12˚40'39" S, 39˚ 40' 23" W). The municipality is at an altitude of 220 meters and has an average temperature of 24.5˚C, relative humidity of 82%, and annual precipitation of 1,197 mm. According to the Köppen classification system, the climate of the region is a transition zone between Am (monsoon climate) and Aw (tropical climate with a dry winter season) (type C1), and it is dry and subhumid. The soil in the experimental field is classified as a Dystrophic Yellow Latosol A - moderate sandy clay texture (Embrapa, 1993).

Plowing was carried out using a moldboard plow, followed by transplanting on 29 May 2024. Base fertilization was carried out based on soil analysis, when transplanting, applying 15 Kg of Nitrogen per hectare, with ammonium sulfate as the source; 50 Kg of phosphorus per hectare from triple superphosphate; and 30 kg per hectare of potassium chloride. Weed control during the crop cycle was done using a weed whacker between lines and by manual weeding using a hoe around the plant before each RPA flight.

1.3. Experimental design

The experimental design was a randomized complete block design, with four genotypes, and six blocks, each plot consisting of five plants of the same genotype. Castor Bean is planted with 4 meters of row spacing and 1 meter of intra-row spacing. A buffer zone is planted surrounding the experiment, consisting of the UFRB-160 Castor Bean Lineage, and each plot was separated by a 3 meters spacing to avoid overlapping between genotypes (Figure 4).



Figure 4. *Overview of the study area in the experimental farm of UFRB. yellow: BRS-ENERGIA; blue: IAC-80, red: UFRB-222, green: UFRB-23; purple: UFRB-160.*

1.4. Meteorological data

The daily meteorological data were collected from the *NASA POWER Data Access Viewer* (DAV) website (https://power.larc.nasa.gov/data-access-viewer/). The extracted variables are date, mean temperature (°C), precipitation (mm), Mean Relative Humidity (%), and all sky surface Photosynthetically Active Radiation (PAR) Total.

1.5. Grey mold severity monitoring

The control of grey mold (*Amphobotrys ricini)* was conducted through three fungicide applications on the following dates: July 31, 2024 (before 10 AM), September 9, 2024 (at 2 PM), and September 28, 2024 (at 9 AM). A fungicide was used containing 875 g/kg (87.5%) of the active ingredient Thiophanate-methyl (Dimethyl 4,4'-(o-phenylene) bis (3-thioallophanate)). Applications were made at a concentration of 50–70 g per 100 liters of water, with recommended application volumes of 500 to 1000 L/ha. Although it is recommended to initiate fungicide applications at the emergence of the primary raceme, due to machinery limitations and climatic conditions, treatments began

instead at the emergence of the secondary racemes. A total of three applications were carried out at seven-day intervals.

Grey mold severity was monitored starting from the transplantation of the plants into the field, with the first symptoms observed on July 23, 2024. In total, five monitoring assessments were conducted on the following dates: July 23, August 2, August 23, September 3, and September 17. The evaluation involved counting the number of affected fruits in the primary cluster of each plant and estimating disease severity using the rule of three. Data were classified according to a diagrammatic scale with six severity levels (Figure 17): 0, 1 (8%), 2 (22%), 3 (43%), 4 (76%), and 5 (100%). These levels corresponded to five severity categories: no disease (ND), low severity (LS), moderate severity (MS), high severity (HS), and total loss (TL), based on the model proposed by Chagas et al. (2010) and adapted by Sousa (2014).

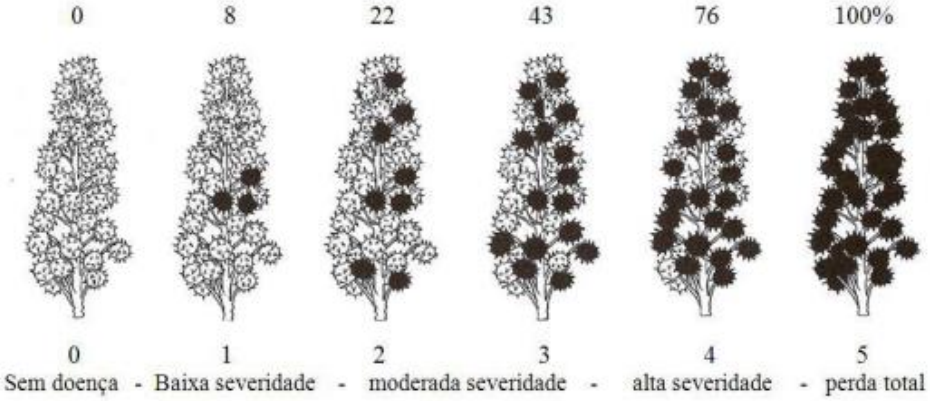


Figure 17. *Six severity levels of grey mold symptoms on castor bean racemes, based on the model by Chagas et al. (2010) and adapted by Sousa (2014)*

1.6. Monitoring date

Field data collection and RPA image acquisition were scheduled according to the phenological stages of the castor bean plant (Table 1) as well as favorable climatic conditions. Phenological stages were monitored twice weekly, from the emergence of the primary raceme to the fruit maturation of the tertiary raceme. A total of 10 RPA flights were conducted. The first flight (V0) occurred before planting. Flight V1 took place during the initial growth stage, before the emergence of the primary raceme. Flights V2, V3, and V4 were conducted during the growth stage, coinciding with the emergence of the primary raceme. Flights V5, V6, V7, and V8 occurred during the production stage, marked by the emergence of the tertiary raceme. Finally, flight V9 was conducted during the maturation stage, when the leaves begin to fall and the fruits reach full maturity.

1.7. Aerial Image acquisition

Before starting image acquisition with the Remotely Piloted Aircraft (RPA), five Ground Control Points (GCPs) were placed, one at each of the four corners of the field and one at the center using fixed stakes (Figure 5.A). These stakes must be firmly fixed to the ground to prevent any movement, ensuring the consistency and accuracy of georeferencing during all flight dates. It is essential to select flat, stable, and open locations with good visibility, ensuring even distribution between the field's extremities and center. The GCP markers used were plastic targets (50x50 cm) with unique numbering. A mobile Real-Time Kinematic (RTK) system was employed prior to the first RPA flight to collect GPS points with real-time, centimeter-level accuracy (Figure 5.B).

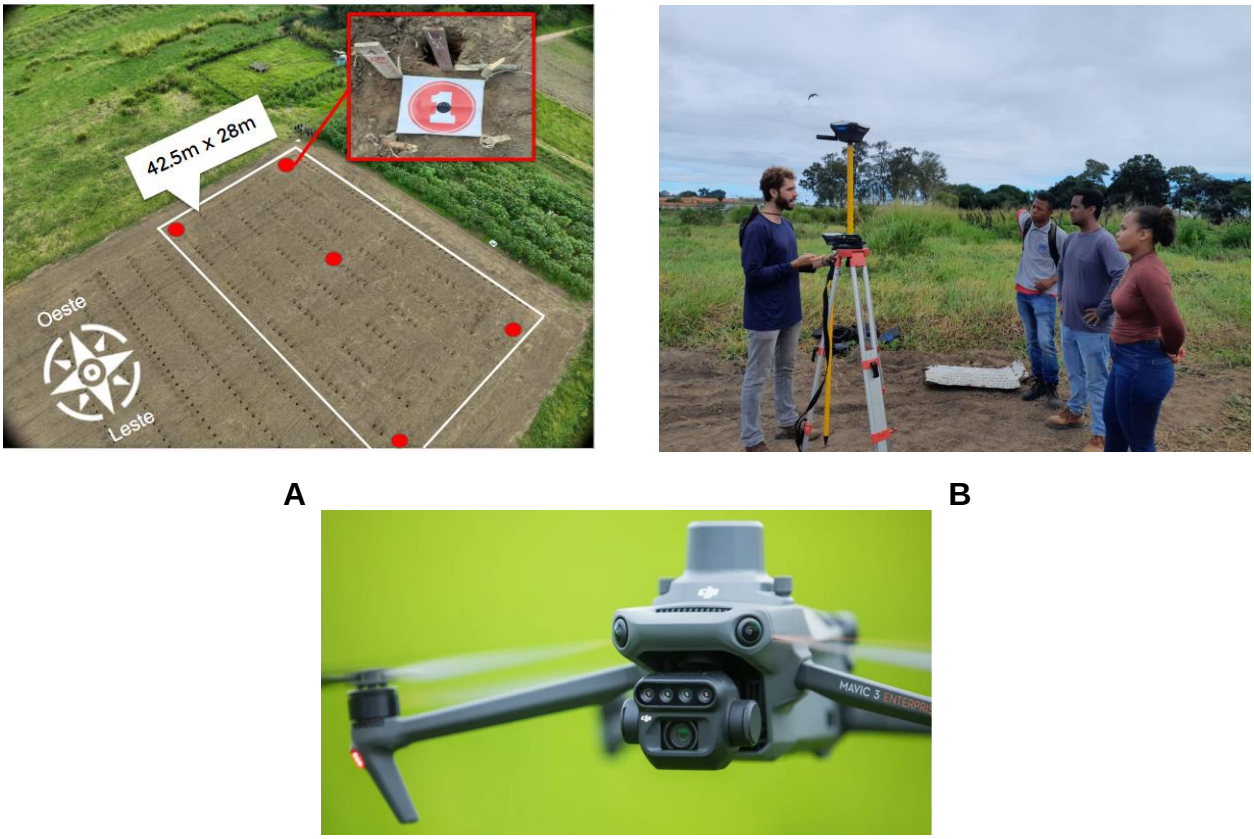


Figure 5. *Ground Control Points (GCP) distribution in the field (A) and the RTK-GNSS system used to georeference the GCP (B), DJI mavic 3 Entreprise M used in this study(C)*

An initial flight (V0) was conducted before transplantation to assess plant height evolution in the Digital Elevation Model (DEM). Subsequently, nine additional flights were performed throughout crop development until maturation, corresponding to the following monitoring dates: June 13, July 7, July 9, July 18, August 1, August 7, August 21, September 4, and October 28 (Figure 6). Flight scheduling was dependent on weather conditions and RPA availability. All RPA flights were conducted at a fixed altitude of 40 meters above ground level, between 12:00 and 13:00. The flight dates were selected based on visual assessment of weather conditions, prioritizing the absence of cloud cover and precipitation, as well as low wind speeds at both plant and RPA level (<12 m/s). Wind conditions were evaluated by observing plant leaves; minimal leaf movement was considered ideal for flight.

Images were captured using a DJI Mavic 3 Enterprise Multispectral (Figure 5.C), equipped with both an RGB camera and a multispectral (MS) camera (Table 8).

Table 8. Camera characteristics of DJI Mavic 3 Enterprise Multispectral

Camera type	Resolution	FOV	BANDS
RGB	20MP	84°	Red, Green, Blue
MS	5MP	73.91°	Green = 580 ±16 nm, Red = 670 ±16 nm, Red-Edge or RE = 720 ±16 nm, and Near-Infrared or NIR = 840 ±26 nm.

The DJI Pilot application facilitated flight planning, path control, and speed regulation during image acquisition. The same flight route and characteristics are used on all flights (Table 9)

Table 9 . Flight parameters from the DJI Pilot Application

Duration	GSD	Flight speed	Side overlap	Front overlap	Margin
2min46sec	1.85 cm/pix	1.5 m/s	80%	90%	2

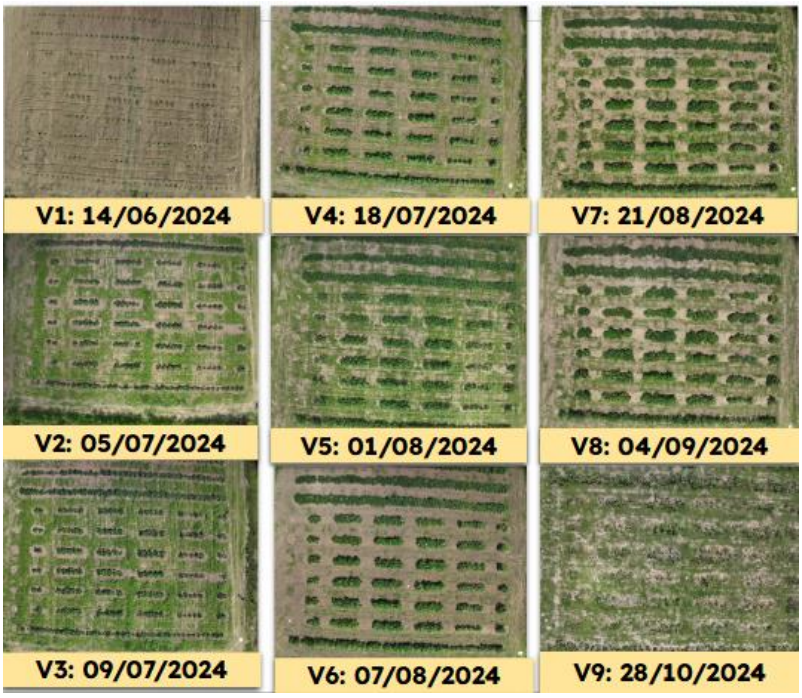


Figure 6. *Aerial image acquisition in 9 different flight dates.*

1.8. Orthomosaic creation

Agisoft Metashape (Educational version) is used to generate the orthomosaics for each flight using the images of the RGB and MS camera. Orthomosaic gathers reflectance data in each pixel. The resulting orthomosaics are exported in raster format (.tif). The methodology used orthomosaic generation from RPA data with Ground Control Points (GCPs) is based on the Agisoft HelpDesk Portal. The process begins by: (1) aerial images upload, (2) photos alignment, (3) Adjustment of the bounding box to reduce processing time, (4) optimize camera alignment**,** (5) load GCPs, and filter photos by GCPs, also known as markers, (6) generate a high quality point cloud, (7) Classify vegetation and soil by color, (8) build DEM from point cloud (9) build orthomosaic based on DEM surface data (10) Export DEM and orthomosaic.

1.9. Vegetation Indices calculation using Orthomosaic

In order to calculate the Vegetation Indices of the RGB and MS orthomosaics, the *FIELDimageR* package (MATIAS et al., 2020) in the *R Software* (R DEVELOPMENT CORE TEAM, 2021) is used. This package facilitates image preparation, enabling users to crop the image, eliminate soil and weed interference, and adjust the image orientation. Additionally, the package generates a plot shapefile for extracting data related to different wavelengths, stand count, canopy coverage, building Vegetation Indices and plant height assessment within each plot. In the Figure 18 below the flowchart used for calculating vegetation indices from RGB and MS images. A total of 14 RGB e 22 MS vegetative indices were calculated.

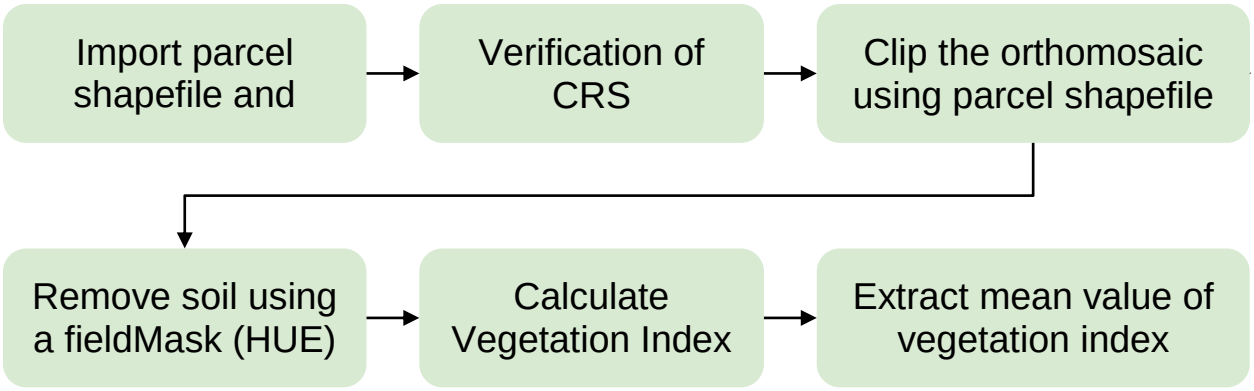


Figure 18. *Flowchart of RGB and MS Vegetation Indices (VI) extraction using FieldImageR package on Rstudio interface.*

❖ **General information**

A literature review was conducted on the 13 RGB-based (BCC, EXG, EXG2, EXGR, EXR, GCC, GLI, MGVRI, NGRDI, RCC, RGBVI, TGI, VARI) and 22 multispectral (MS)-based (CIG, CIRE, CVI, DVI, GDVI, GNDVI, GOSAVI, GRVI, MCARI1, MCARI2, MDD, MNLI, MSR, MTCARI, NDRE, NDVI, NRI, OSAVI, PSRI, RVI, SAVI, TVI) vegetation indices generated from RPA orthomosaics. Table 10 summarizes each index, including its full name, formula, and primary use. In general, these vegetation indices are widely applied to assess crop health, canopy structure, and biomass accumulation throughout the growing season.

Table 10. Vegetation indices used for generating the growth curve models.

VI	Name	Formula	Use	Reference
BCC	Blue Chromatic Coordinate	Blue / (Green + Red + Blue)	Quantifies greenness using blue reflectance	Moore et al., 2016
EXG	Excess Green Index	2*Green - Red - Blue	Captures greenness; chlorophyll-correlated	Woebbecke et al., 1995; Arjenaki et al., 2012
EXG2	Excess Green Index 2	(2*Green - Red - Blue) / (Green + Red + Blue)	Robust green extraction; lighting tolerant	Woebbecke et al., 1995; Arjenaki et al., 2012
EXGR	Excess Green minus Red	3*Green - 2.4*Red - Blue	Emphasizes green; detects vegetation structure	Liu et al., 2015; Nguyen et al., 2024; Woebbecke et al., 1995
EXR	Excess Red Index	1.4*Red - Green	Health and biomass; solar-sensitive	Guo et al., 2008
GCC	Green Chromatic Coordinate	Green / (Red + Green + Blue)	Green reflectance; phenology monitoring	Toomey et al., 2020; Richardson et al., 2016
GLI	Green Leaf Index	(2*Green - Red - Blue) / (2*Green + Red + Blue)	Detects green vegetation	Yilmaz et al., 2019
MGVRI	Modified Green Red Vegetation Index	(Green^2 - Red^2) / (Green^2 + Red^2)	Health and density	Barbosa et al., 2019
NGRDI	Normalized Green–Red Difference Index	(Green - Red) / (Green + Red)	Visible bands for cover/biomass	Gitelson et al., 2002; Kusumandari et al., 2022
RCC	Red Chromatic Coordinate	Red / (Green + Red + Blue)	Red proportion; color analysis	Richardson et al., 1987
RGBVI	Red Green Blue Vegetation Index	(Green^2 - Red*Blue) / (Green^2 + Red*Blue)	Early biomass detection	Pereira et al., 2024; Joshi et al., 2023
TGI	Triangular Greenness Index	Green - (0.39*Red - 0.69*Blue)	Crop vigor	USDA ARS, 2013; NV5, 2024; Yagci et al., 2020
VARI	Visible Atmospherically Resistant Index	(Green - Red) / (Green + Red - Blue)	Reduces illumination effects	Yilmaz et al., 2019
CIG	Chlorophyll Index—green	(NIR / Green) - 1	Green band for chlorophyll	Gitelson et al., 2003
CIRE	Red-edge chlorophyll index	(NIR / RedEdge) - 1	Chlorophyll content	Barnes et al., 2000

CVI	Chlorophyll Vegetation Index	(NIR * Red) / (Green^2)	Chlorophyll proxy; health indicator	Kawashima and Nakamura, 1988
DVI	Difference Vegetation Index	NIR - RedEdge	Vigor	Gunathilaka, 2021
GDVI	Generalized Difference Vegetation Index	NIR - Green	Canopy density, chlorophyll	Gitelson et al., 2014; CGAIR, 2022
GNDVI	Green normalized differences vegetation index	(NIR - Green) / (NIR + Green)	Stress, biomass	MDPI Sensors, 2025
GOSAVI	Green Optimized Soil Adjusted Vegetation Index	1.16 * (NIR - Green) / (NIR + Green + 0.16)	Chlorophyll; Soil-adjusted	Ahmad et al., 2020; Saha et al., 2020
GRVI	Green Ratio Vegetation Index	NIR / Green	Green ratio; precision monitoring	Rouse et al., 1974; Bannari et al., 2010; ESA SNAP Toolbox, 2024
MCARI1	Modified Chlorophyll Absorption Ratio Index 1	((NIR - RedEdge) - 0.2*(NIR - Green)) * (NIR / RedEdge)	Chlorophyll absorption; leaf area sensitive	Saha et al., 2020
MCARI2	Modified Chlorophyll Absorption Ratio Index 2	(1.5*(NIR - RedEdge) - 1.3*(NIR - Green)) / sqrt((2*NIR+1)^2 - (6*NIR - 5*sqrt(RedEdge)) - 0.5)	Corrected for leaf structure	Haboudane et al., 2004; NV5, 2024
MDD	Modified Difference Drought index	(NIR - RedEdge) - (RedEdge - Green)	Drought monitoring; wheat growth stages	Zhang et al., 2019; Zhou et al., 2024
MNLI	Modified Non-Linear Vegetation Index	(1.5*(NIR^2 - Red)) / (NIR^2 + Red + 0.5)	Vegetation-soil discrimination; lighting tolerant	Koparan et al., 2019; Scribd Document, 2017
MSR	Modified Simple Ratio	((NIR / Red) - 1) / sqrt((NIR / Red) + 1)	Enhances canopy	Zhou et al., 2020; Dronova et al., 2018
MTCARI	Modified Chlorophyll Absorption Ratio Index	3 * ((NIR - RedEdge) - 0.2 * (NIR - Green) * (NIR / RedEdge))	Minimizes soil effect; chlorophyll-sensitive	Zhao et al., 2013
NDRE	Normalized Difference Red Edge Index	(NIR - RedEdge) / (NIR + RedEdge)	Chlorophyll in later stages	Louisiana State Univ. study, 2023
NDVI	Normalized Difference Vegetation Index	(NIR - Red) / (NIR + Red)	Density ; health	Xiong et al., 2023

NRI	Nitrogen Reflectance Index	Red / (NIR + RedEdge + Red)	Leaf or canopy nitrogen	Filella et al., 1995; Ding et al., 2014
OSAVI	Optimized Soil Adjusted Vegetation Index	(NIR - Red) / (NIR + Red + 0.16)	Sparse vegetation monitoring	Rondeaux et al., 1996
PSRI	Plant Senescence Reflectance Index	(Red - Green) / RedEdge	Senescence via carotenoid ratio	ISPRS Annals, 2023
RVI	Ratio Vegetation Index	NIR / Red	Vigor	Jordan, 1969
SAVI	Soil-Adjusted Vegetation Index	1.5 * (NIR - Red) / (NIR + Red + 0.5)	Low cover; soil-sensitive	Huete, 1988
TVI	Transformed Vegetation Index	0.5 * (120*(NIR - Green) - 200*(Red - Green))	Vegetation cover and vigor	Xing, N. et al., 2020

❖ **Statistical analysis**

Spearman and Pearson correlation analyses were applied to the multispectral (MS) and RGB vegetation indices, respectively, in relation to growth parameters measured during the growing season. Indices with non-significant correlations based on the t-test (5% significance level) were discarded and excluded from further analysis.

1.10. Phenological models

To understand the phenological dynamics of the four castor bean genotypes (BRS-ENERGIA, IAC-80, UFRB-222, UFRB-23) using vegetation indices from RGB and MS images, nonlinear regression models were fitted to the temporal index data using *RStudio 4.4.2* interface (Figure 19). The data were first organized by genotype and days after sowing (DAS), with missing values removed. Vegetation indices were normalized between 0 and 1. The result dataset is prepared by creating all the possible combinations of the 89 vegetation indices and 4 genotypes.

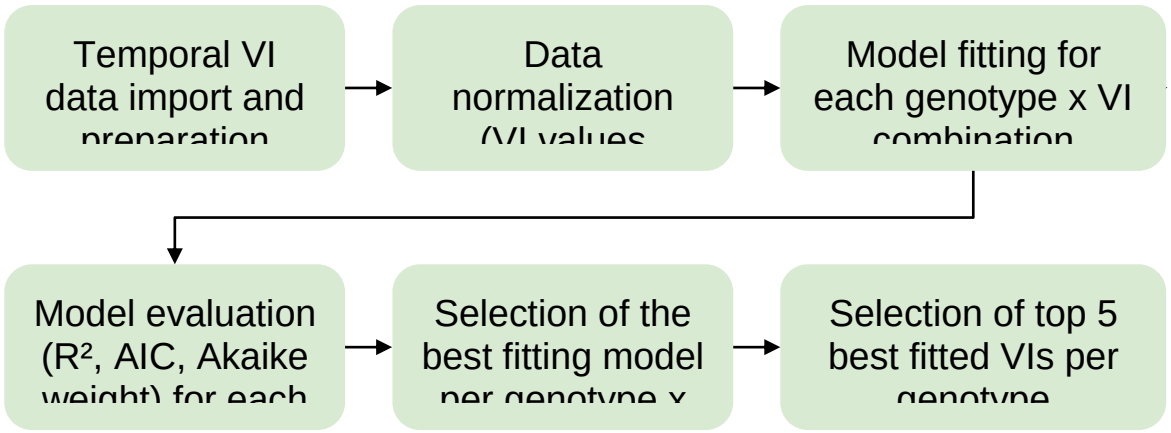


Figure 19. *Flowchart of phenological model and vegetation index (vi) selection for each genotype (BRS-ENERGIA, IAC-80, UFRB-222, UFRB-23)*

Six growth models (Logistic, Gompertz, Richards, Weibull, Exponential, and quadratic) (Table 11) were fitted for each genotype-index combination. Model parameters of the nonlinear models (Logistic, Gompertz, Exponential, Richards, Weibull and Exponantial) were estimated using the nonlinear least squares with the Levenberg-Marquardt algorithm implemented via nlsLM() function from the *minpack.lm* package (ELZHOV et al., 2016). The quadratic model parameters are estimated using the ordinary Least squares of the standard linear regression model lm() from base R. In order to select the best-fitting model in each combination, first the models that failed to converge are discarded.

Then, model performance was assessed using R^2 to evaluate the goodness of fit between observed and predicted values, with higher r values demonstrating better fit of the curve. Additionally, the Akaike Information Criterion (AIC) measures the quality of the model fit and complexity for the same dataset, which means the AIC compares the best of the six models of the same Genotype x Indice combination, then, the Akaike weight ω_i is calculated, it gives information about the relative probability that each model is the best one among the set considered. Both AIC and ω_i are used allowing selection of the best-fitting model in each case. The top five vegetation indices per genotype were selected, and those common to all genotypes were used to plot phenological curves for comparative growth analysis.

Table 11. Growth regression models used in this study

Growth model	Curve type	Function	Parameters	Use	Reference
Logistic	Sigmoid	$y = \frac{A}{1 + e(\frac{x - x_0}{B})}$	*A*: maximum value x_0 : inflection point *B*: growth rate scaling factor x : independent variable y : output	Population growth, epidemiology, crop modeling	RICHARDS, 1959
Gompertz	Sigmoid Asymmetric	$y = A \, . e^{(-e(\frac{x - x_0}{B}))}$	*A*: maximum value x_0 : inflection point *B*: growth rate scaling parameter x : independent variable y : output	Tumor growth, demographic studies, bacterial growth marked by smaller initial growth	GOMPERTZ, 1825
Richards	Sigmoid with adjustable shape	$y = \frac{A}{(1 + B.e^{-kx})^m}$	*A*: maximum value *K* : growth rate *B*: shape parameter m : curve flexibility x : independent variable y : output	Flexible biological growth modeling	RICHARDS, 1959
Weibull	Sigmoid Asymmetric	$y = a \, . e^{-e^{-b(x-c)}}$	*a*: maximum value *b*: steepness parameter c : center parameter x : independent variable y : output	Survival analysis, plant growth, failure time modeling	CAUSTON; VENUS, 1981
Exponential	Exponential growth or decay	$y = Ae^{bx} + \epsilon$	A : initial value at x=0 b: Growth rate x : Independent variable y = output ϵ : Random error	Modeling growth/decay, finance, biology	HUNT, 1982
Quadratic or 2nd-degree Polynomial	Quadratic (U-shape or inverted U)	$y = \beta_0 + \beta_1 x + \beta_2 x$	$\beta_0, \beta_1, \beta_2$: regression coefficients x : independent variable y : response variable	General purpose curve fitting	ARCHONTOULIS; MIGUEZ, 2015

RESULTS

2.1 Climatic conditions

During the crop growing season, from June to October 2024, climatic conditions showed moderate variability across all measured parameters (Figure 8).

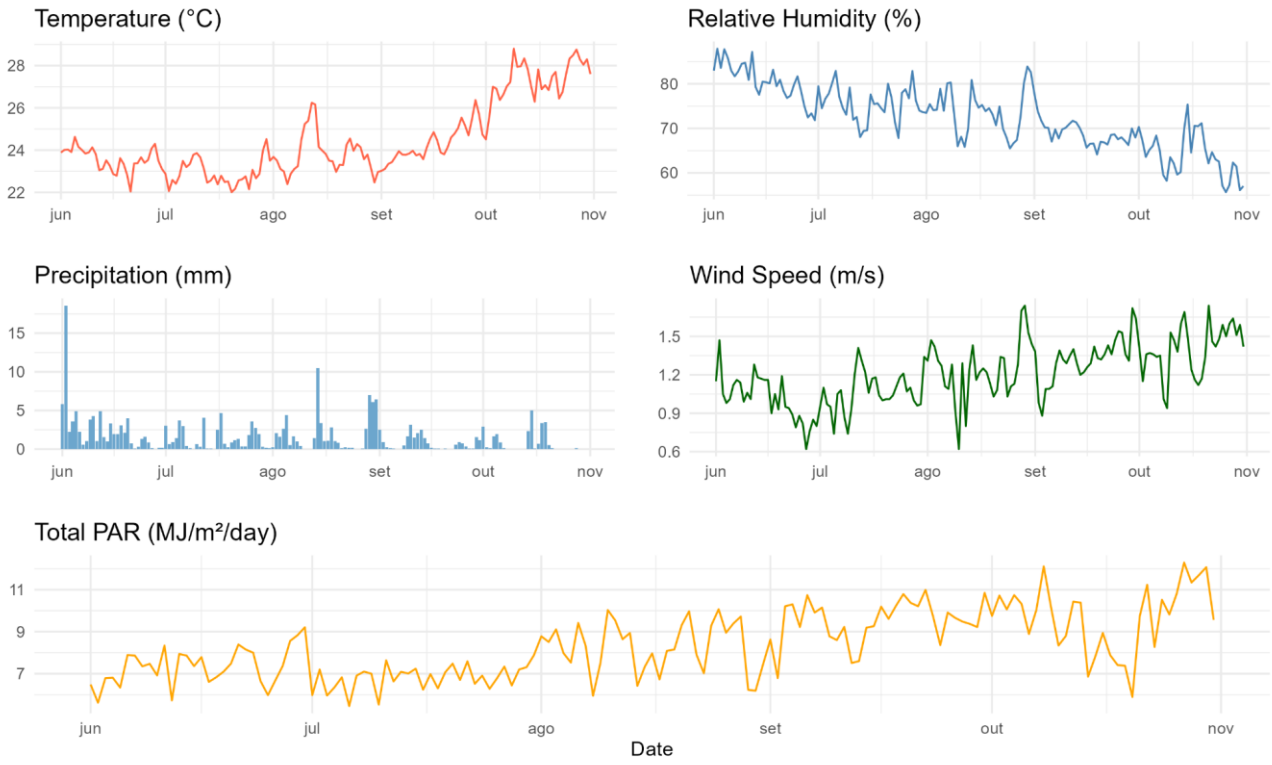


Figure 8. *Daily average temperature, relative humidity, precipitation,wind speed at 2 meters height, and all sky surface photosynthetically active radiation (PAR) total, through the growing season.*

The wind speed at 2 meters height remained relatively stable throughout the period, with values ranging from 0.62 m/s to 1.74 m/s. Regarding radiation, the total photosynthetically active radiation (PAR) measured at the surface ranged from 5.46 MJ/m²/day to 12.29 MJ/m²/day, with a mean of 8.32 MJ/m²/day.

2.2 Grey mold incidence and severity

The stacked bar chart (Figure 20) represents the distribution of Grey mold severity classes in four castor bean genotypes (BRS-ENERGIA, IAC-80, UFRB-222, and UFRB-

23) evaluated at five time points (90, 100, 121, 132, and 146 DAS) and across the first three racemes (R1, R2, and R3).

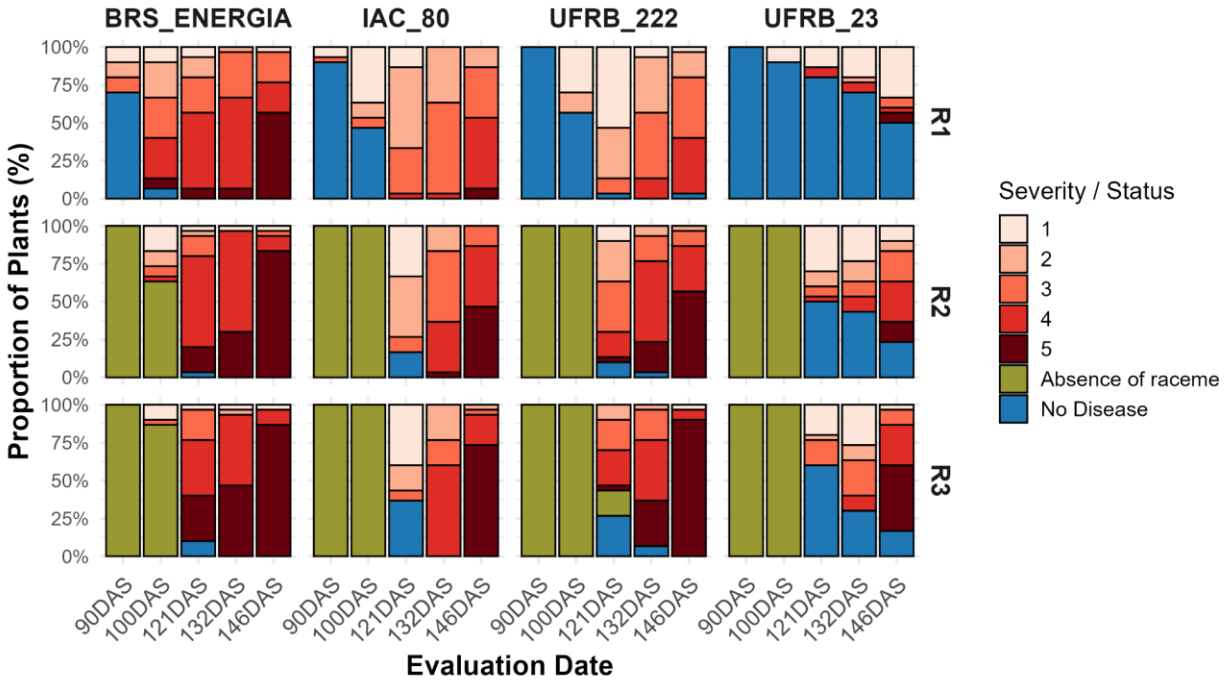


Figure 20. *Temporal progression of grey mold (Amphobotrys ricini) severity classes in castor bean genotypes (BRS-ENERGIA, IAC-80, UFRB-222, UFRB-23) across the first three racemes.*

The colors indicate the proportion of each severity class within the racemes at each stage. A progressive increase in disease severity was observed over time in most genotypes, especially from 121 DAS onward. BRS-ENERGIA, an early-maturing genotype, exhibited the earliest symptoms, with intermediate and severe classes already present by 100 DAS, particularly in racemes R1 and R2. IAC-80 also showed a high degree of susceptibility, with a sharp increase in severity from 121 DAS. UFRB-222 presented an intermediate response, showing a gradual shift from lower to higher severity classes as the cycle progressed. In contrast, UFRB 23 maintained high proportions of healthy or low-severity classes across all racemes and time points, indicating greater resistance. The evaluation of Grey mold was done for monitoring and explanatory purposes of the growth results when needed.

2.3 Plant yield

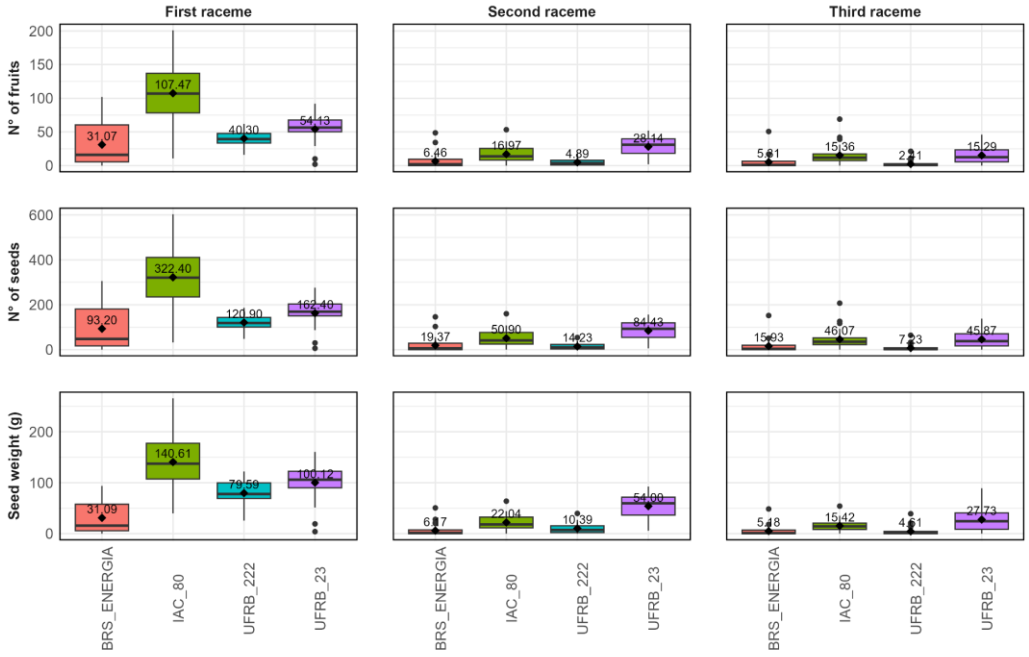


Figure 21. *Boxplots of yield components (number of seeds, number of fruits, and seed weight in grams) for racemes 1, 2, and 3 across four castor bean genotypes (BRS-ENERGIA, IAC-80, UFRB-222, and UFRB-23).*

The IAC-80 cultivar exhibited the highest mean values for number of fruits (107.47), number of seeds (322.4), and seed weight (140.61 g) in the first raceme, followed by the UFRB-23 lineage and then UFRB-222. In contrast, the BRS-ENERGIA cultivar presented the lowest yield parameters across all racemes, primarily due to the severity of grey mold (A*mphobotrys ricini*) infection. In the second and third racemes, UFRB-23 showed superior yield performance, followed by IAC-80 and UFRB-222. The environmental conditions of the region are conducive to the development of grey mold, and the delayed application of preventive fungicide, combined with the absence of a specific active ingredient targeting this pathogen, likely exacerbated its negative impact on plant yield. The evaluation of yield was done for monitoring and explanatory purposes of the growth results when needed.

2.4 Flight parameters

Although the experiment was carried out during the winter season, which is typically characterized by frequent rainfall and strong winds in the region, it was still possible to successfully complete nine flights throughout the experimental period. Table 5 presents the meteorological conditions recorded on the dates of the nine RPA flights.

Table 5. Climatic conditions during image acquisition between 12h and 13h

Flight date (DAS)	Temperature (°C)	Relative Humidity (%)	Wind speed at 2 meters (m/s)	Wind speed at 40 meters (m/s)	Precipitation (mm)	Hourly PAR (MJ/m²/hour)
51	28.44	49.26	2.0	5.2	0.47	1.1
73	28.74	52.42	1.31	3.17	0.34	0.97
77	29.45	46.3	1.97	4.97	0.12	0.97
85	29.6	40.13	1.69	4.21	0.09	0.76
100	30.21	42.88	2.16	5.43	0.28	1.17
105	29.76	45.45	1.39	3.49	1.58	1.21
118	30.91	33.36	1.74	4.19	0.0	1.4
132	31.42	37.28	1.66	3.98	0.0	1.47
187	36.1	32.3	1.74	4.03	0.0	1.55

Temperatures (Table 5) ranged from 28.44°C to 36.10°C, with the highest temperature observed on October 28th, indicating a seasonal transition toward warmer conditions. Relative humidity varied between 32.3% and 52.42%, generally decreasing over time, particularly from August onward (118 DAS). Wind speed was recorded at two heights: 2 meters (plant level) and 40 meters (flight altitude). At 2 meters, wind speeds ranged from 1.31 to 2.16 m/s, suggesting mild ground-level wind conditions. At 40 meters, wind speeds were consistently higher, ranging from 3.17 to 5.43 m/s, yet still within safe operational limits for RPA flights (<12m/s). Precipitation levels were minimal or absent on

most flight dates, with no rainfall recorded on the final three flights. The highest precipitation (1.58 mm) occurred on August 7th, although conditions at flight time remained within acceptable thresholds. Finally, the Photosynthetically Active Radiation (PAR) integrated over the 12:00-13:00 period, representing light availability, ranged from 0.76 to 1.55, reflecting generally favorable lighting conditions for aerial imaging, especially during the later flights with minimal cloud cover and higher solar angle. These data confirm that, despite the experiment taking place during the winter and early spring, periods typically associated with rain and wind in the region, the selected flight windows provided acceptable environmental conditions for aerial data acquisition according to the user manual of the aircraft (DJI, 2023). The resulting orthomosaics showed a high Ground Sample Distance (GSD) (Table 11). For the RGB camera, GSD values ranged from 1.09 to 1.13 cm/pixel, corresponding to a field area of 1.1881 to 1.2769 cm². For the multispectral (MS) camera, GSD values ranged from 1.87 to 1.9 cm/pixel, corresponding to a field area of 3.4969 to 3.61 cm². The variation in GSD between RGB and MS orthomosaics is due to differences in camera resolution. Differences in orthomosaic dimensions and sizes are attributed to the manual delimitation of the bounding box during image processing; however, these parameters do not affect the accuracy of the height data.

Table 11. Summary of flight parameters and information on orthomosaic processing.

Flight date (DAS)	N° of images	RGB Orthomosaic dimension	RGB Orthomosaic resolution	RGB Orthomosaic size	MS Orthomosaic dimension	MS Orthomosaic resolution	MS Orthomosaic size
51	71	7.376 x 7.886	1.12 cm/pix	669.67 MB	*NA*	*NA*	*NA*
73	75	7.180 x 8.196	1.11 cm/pix	805.02 MB	4.210 x 4.428	1.89 cm/pix	4.33 GB
77	75	6.872 x 7.448	1.13 cm/pix	787.66 MB	6.6876 x 6.919	1.87 cm/pix	505.74 MB
85	71	6.980 x 7.328	1.1 cm/pix	719.84 MB	4.454 x 4.298	1.88 cm/pix	4.09 GB
100	71	7.032 x 7.728	1.1 cm/pix	740.65 MB	4.468 x 4.386	1.86 cm/pix	4.12 GB
105	41	7.222 x 7.670	1.09 cm/pix	666.81 MB	3.572 x 3.992	1.88 cm/pix	2.20 GB

118	72	7.204 x 7.610	1.09 cm/pix	689.36 MB	3.994 x 4.168	1.88 cm/pix	3.70 GB
132	74	6.982 x 7.236	1.1 cm/pix	705.23 MB	3.964 x 4.202	1.87 cm/pix	3.78 GB
187	71	7260 x 7.798	1.11 cm/pix	759.69 MB	4.276 x 4.518	1.9 cm/pix	4.00 GB

2.5 Vegetation indices

❖ Correlation between vegetation indices and growth parameters

A correlation analysis was conducted to assess the relationship between vegetation indices and plant growth variables throughout the growing season. Based on this analysis, six vegetation indices — RVI, MSR, SAVI, OSAVI, NDVI, and EXG — were excluded from subsequent modeling steps due to their lack of significant correlation with growth parameters ($p > 0.05$). These indices either exhibited weak associations or inconsistencies in capturing phenological trends under the conditions of this study. The remaining indices demonstrated statistically significant correlations ($p < 0.05$) with at least one growth parameter, highlighting their potential utility in modeling phenological dynamics. These retained indices comprise both RGB-derived (Figure 22) and multispectral (MS)-derived indices (Figure 23), capturing a range of physiological properties such as chlorophyll concentration, canopy structure, and vegetation vigor. Their inclusion in later model calibration and selection steps ensures that only the most informative and statistically relevant predictors are utilized.

Number of Leaves

Among RGB-derived indices, VARI ($r = 0.84$), MGVRI ($r = 0.82$), and NGRDI ($r = 0.82$) showed very strong positive correlations with the number of leaves, highlighting their responsiveness to canopy density and leaf biomass. Multispectral indices such as MDD ($r = 0.64$), MCARI1 ($r = 0.63$), and MTCARI ($r = 0.61$) also demonstrated strong associations, indicating relevance for pigment and biomass monitoring.

Stalk Diameter

The RGB indices VARI ($r = 0.72$), MGVRI ($r = 0.71$), and NGRDI ($r = 0.71$) correlated strongly with stalk diameter, underscoring their ability to reflect stem thickness. Among multispectral indices, CIRE ($r = 0.59$) and CVI ($r = 0.58$) displayed moderate to

strong correlations, suggesting utility for tracking structural development and chlorophyll content.

Canopy Area

For the canopy area, both RGB and multispectral indices demonstrated relevant associations. Among RGB indices, MGVRI (r = 0.46), NGRDI (r = 0.45), and VARI (r = 0.45) showed moderate positive correlations. In contrast, MS indices had slightly stronger responses, with CVI (r = 0.58), PSRI (r = 0.53), and GRVI (r = 0.49) all indicating moderate to strong correlations with canopy area.

Canopy Volume

With respect to canopy volume, multispectral indices led with CVI (r = 0.63), CIRE (r = 0.61), and GNDVI (r = 0.58) showing moderate to strong correlations with canopy volume. Among RGB indices, VARI and MGVRI also showed moderate correlations (r ≈ 0.5), supporting their use in volume-related estimations.

Canopy Diameter 1

The following MS indices CVI (r = 0.63), CIRE (r = 0.61), and GNDVI (r = 0.60) showed strong positive correlations with canopy diameter 1, indicating sensitivity to green biomass accumulation. No RGB index showed strong correlation at this growth stage.

Canopy Diameter 2

RGB indices displayed strong associations with canopy diameter 2, notably MGVRI (r = 0.67), VARI (r = 0.66), and NGRDI (r = 0.65). These results highlight the effectiveness of RGB-derived indices in tracking lateral canopy expansion during vegetative growth.

Despite being important agronomic traits, plant height (AP), canopy area (CA), and canopy volume (CV) exhibited weaker correlations with vegetation indices compared to other growth parameters. This may be attributed to the fact that most vegetation indices are derived from top-view spectral reflectance, which primarily captures horizontal canopy features such as surface greenness, pigment concentration, and spatial coverage. In

contrast, traits like plant height and volume reflect the vertical structure and three-dimensional morphology of the plant, which are not well represented in 2D imagery. Additionally, CA and CV are calculated from crown diameters (CD1 and CD2) through nonlinear transformations that can amplify small measurement errors and biological variation, thereby reducing correlation strength. Similar findings were reported by Bendig et al. (2015), who observed that RPA-based vegetation indices correlated more strongly with canopy coverage than with plant height or volumetric traits derived from field measurements.

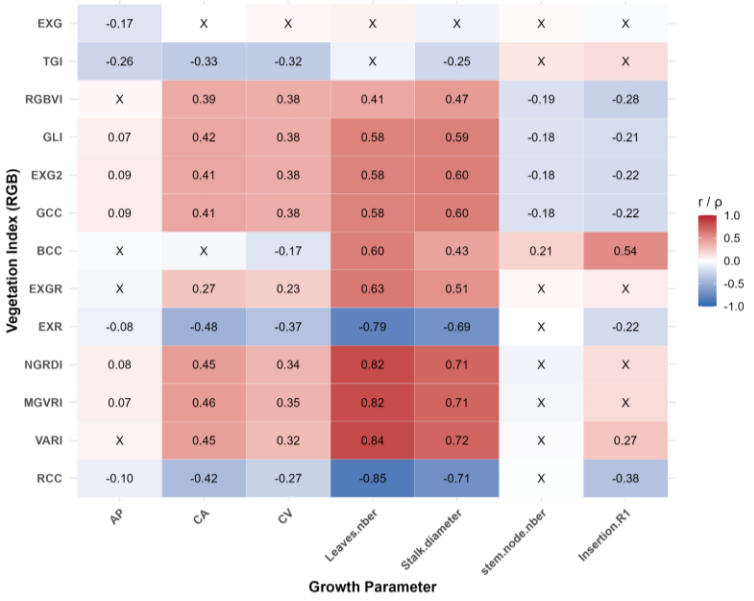


Figure 22. *Pearson correlation studies done between RGB vegetation indices and growth parameters*

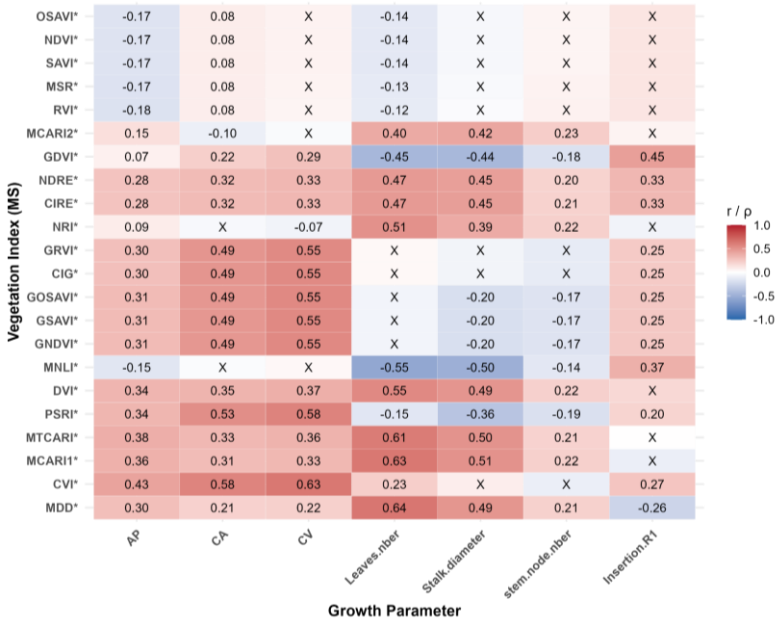


Figure 23. *Spearman correlation studies done between MS vegetation indices and growth parameters*

Legend : AP: Plant Height; CA: Canopy Area; CD1: Crown Diameter 1; CD2: Crown Diameter 2; CV: Canopy Volume; Insertion.R1: Insertion of first raceme (m), Leaves.nber: Leaves count; Stalk.diameter: Stalk diameter at mid-point; Stem.node.nber: Stem node number beneath insertion point of first raceme

2.6 Phenology models

❖ Model fitting and calibration

The selected RGB and multispectral (MS) vegetation indices were fitted to six different growth models. However, only 79% of the expected genotype × vegetation index × model combinations resulted in successful fits. The remaining 21% of combinations failed to converge, primarily due to null or near-zero variance in the vegetation index values. Such conditions produce nearly constant trends that do not conform to the assumptions of sigmoidal or parabolic functions, which require sufficient variability to characterize distinct growth phases and estimate parameters reliably. These limitations are well-documented in nonlinear modeling, where insufficient data variation often leads to non-identifiability and convergence failure during regression fitting (SPIESS; NEUMEYER, 2010) (Figure 24).

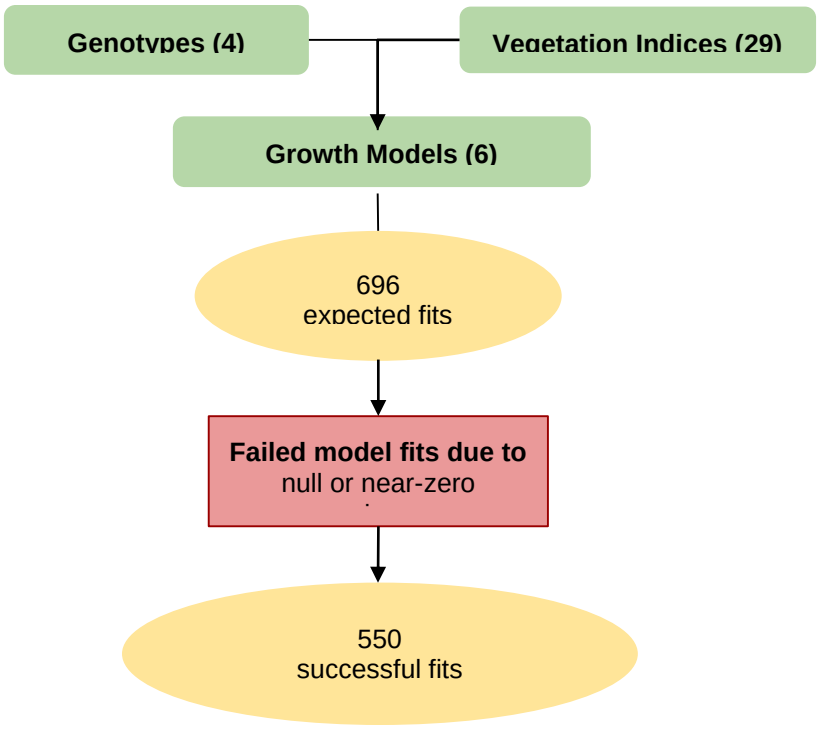


Figure 24. *Model fitting fails percentage and cause*

Among the evaluated growth models, the quadratic and exponential models demonstrated robust fitting performance, successfully modeling all 120 combinations of genotype × vegetation index without any failures. In contrast, the Gompertz, Logistic, Richards, and Weibull models exhibited fitting failures across all four genotypes, as illustrated in Figure 25. Notably, six vegetation indices (CIG, GNDVI, GOSAVI, GRVI, GSAVI, and PSRI) were successfully fitted by all models across all genotypes, indicating their stability and adaptability in nonlinear growth modeling. Conversely, the remaining 24 RGB and multispectral vegetation indices encountered at least one fitting failure, as detailed in the heatmap presented in Figure 26.

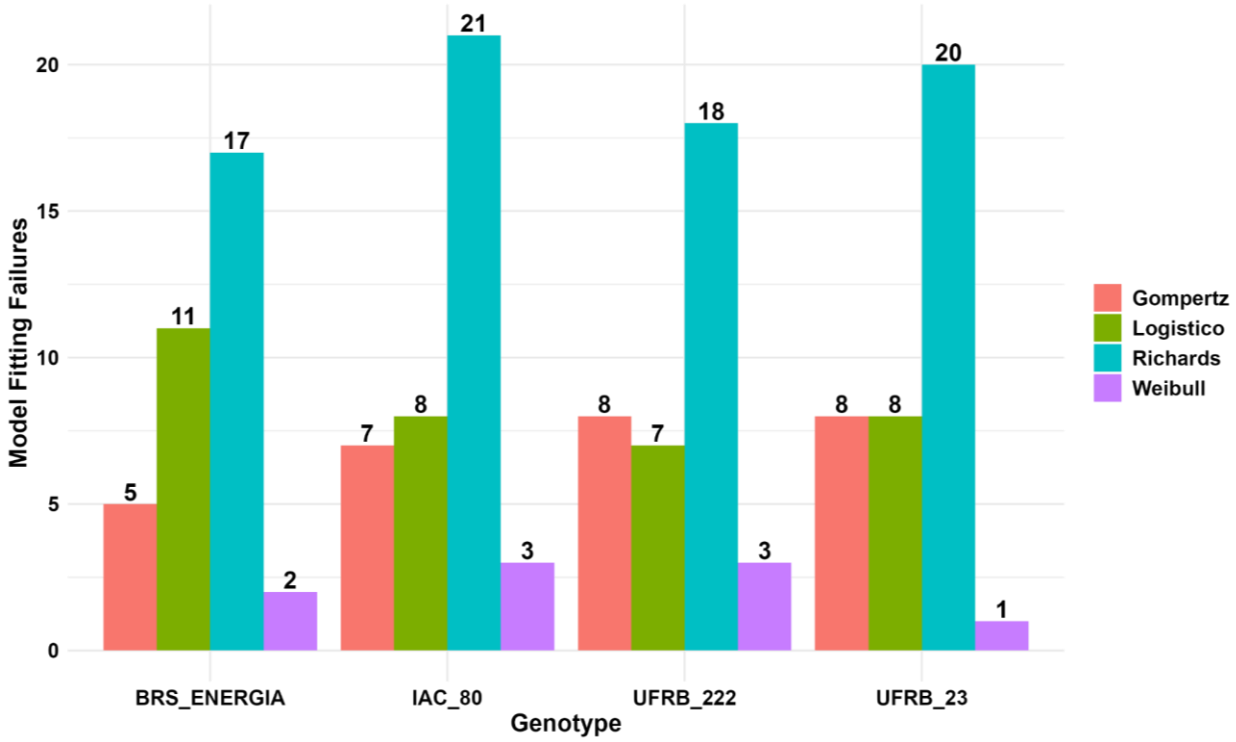


Figure 25. *Number of model fitting failure per genotype and model.*

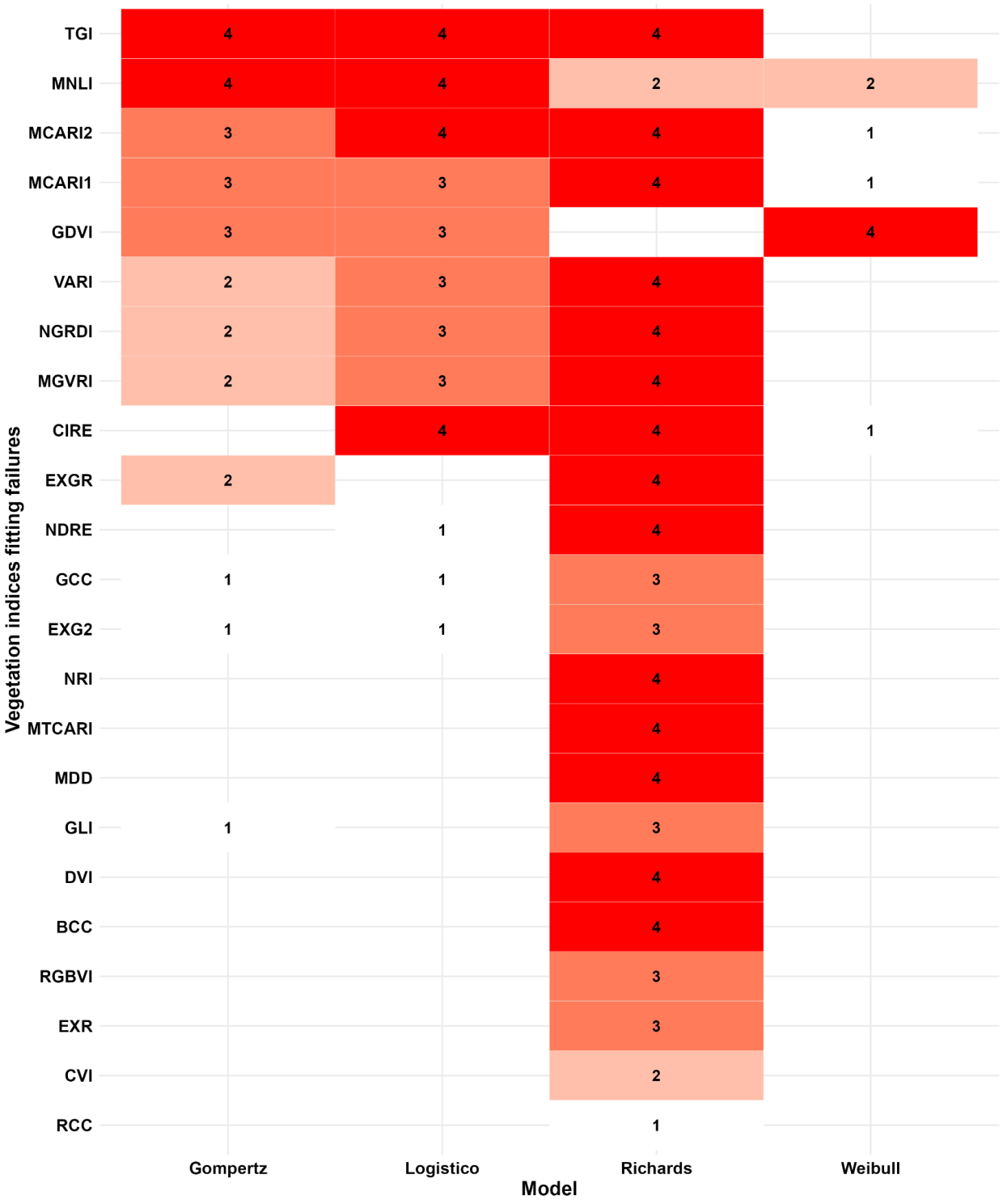


Figure 26. *Vegetation indices with model fitting failures across all genotypes.*

❖ **Model evaluation and selection**

Figure 27 summarizes the best-fitting growth models selected for each genotype × vegetation index combination, using the Akaike Information Criterion (AIC) and Akaike weight (ω_i) as selection metrics. Among the models that successfully converged, only the one with the lowest AIC and highest wi was retained for each index.

For the genotype BRS-ENERGIA, all 30 vegetation indices were best described by one of four models: Quadratic, Logistic, Exponential, or Weibull. The genotypes IAC-80 and UFRB-222 showed successful model fits across five of the six tested models (Quadratic, Logistic, Exponential, Weibull, and Richards) indicating a moderate diversity in curve adaptability. In contrast, UFRB-23 exhibited the greatest flexibility, with all six models, including the Gompertz model, emerging as best fits for at least one vegetation index. This broader model suitability may reflect more complex or less constrained growth dynamics in this genotype. Notably, vegetation index × model combinations with an Akaike weight (ω_i) equal to 1 indicates a 100% relative likelihood of being the best model among those tested (BURNHAM & ANDERSON, 2002). Such values provide strong evidence of model superiority within the candidate set.

The top five vegetation indices were identified for each genotype (Table 12):

- EXGR, EXR, GLI, and MGVRI for BRS_ENERGIA;
- EXG2, EXR, GCC, GLI, and RGBVI for IAC_80;
- EXG2, EXGR, GCC, GLI, and RGBVI for UFRB_23;
- EXG2, EXR, GCC, GLI, and RGBVI for UFRB_222.

Among these, GLI and RGBVI are common to all genotypes' top five vegetation indices and were selected for phenological curve comparison.

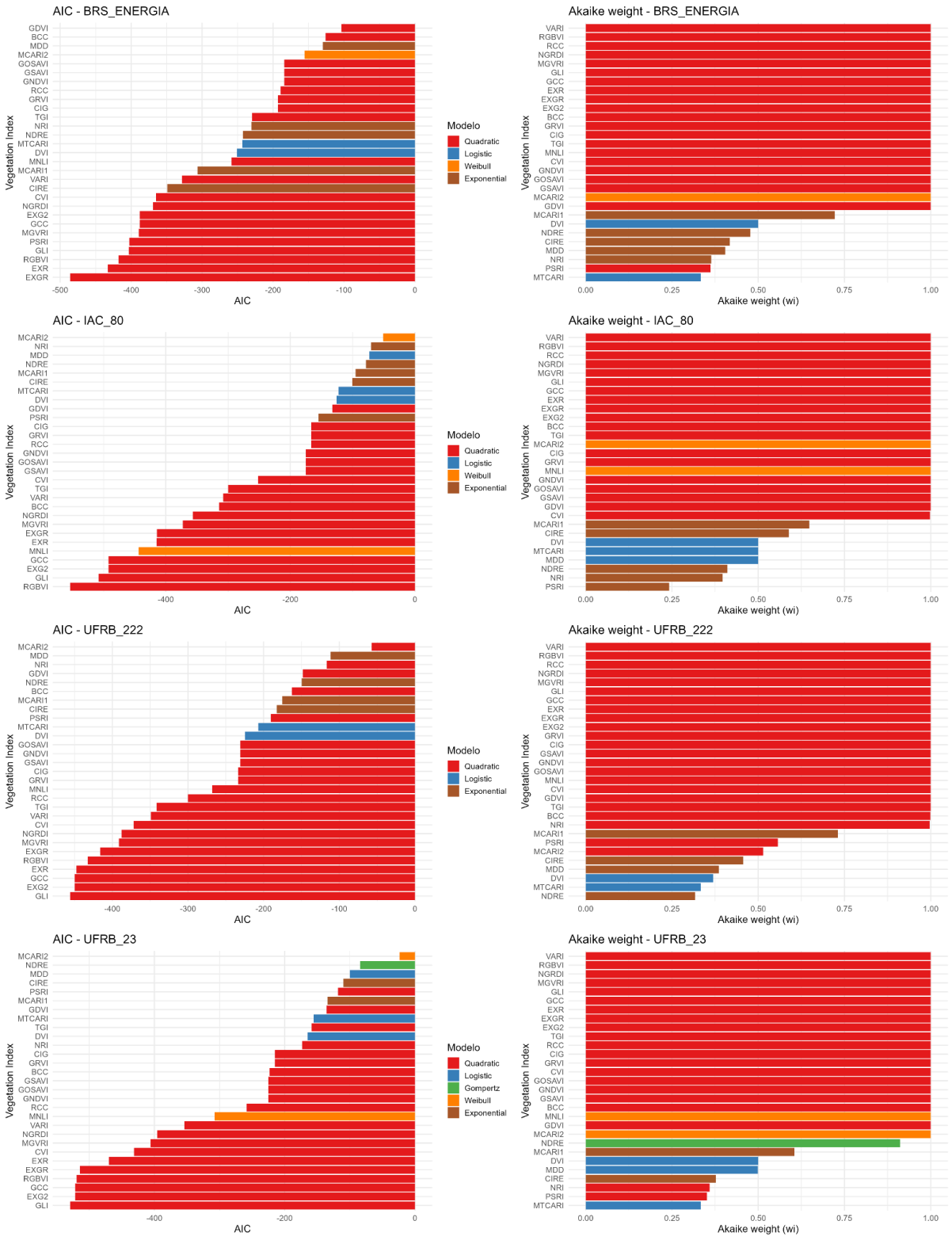


Figure 27. *Model selection for vegetation index-based growth curves using AIC and Akaike weights across four castor bean genotypes.*

***Table 12. Top five vegetation indices per genotype according to lowest AIC and highest ω_i* values obtained with the quadratic growth model**

Genotype	Vegetation index	R^2	AIC	ω_i
BRS–ENERGIA	EXGR	0,7289	–486,067	1
	EXR	0,7306	–432,853	1
	RGBVI	0,6510	–418,060	1
	GLI	0,6650	–403,112	1
	MGVRI	0,7241	–389,248	1
IAC–80	RGBVI	0,7670	–553,738	1
	GLI	0,7675	–507,783	1
	EXG2	0,7536	–491,887	1
	GCC	0,7536	–491,885	1
	EXR	0,7640	–414,603	1
UFRB–222	GLI	0,7253	–455,897	1
	EXG2	0,7077	–449,765	1
	GCC	0,7077	–449,764	1
	EXR	0,7922	–447,488	1
	RGBVI	0,7102	–432,288	1
	GLI	0,7287	–529,463	1
	EXG2	0,7156	–521,503	1

UFRB–23	GCC	0,7156	–521,502	1
	RGBVI	0,7204	–519,300	1
	EXGR	0,7453	–514,389	1

❖ **Model fitting**

The top 5 vegetation indices of the four genotypes were fitted with a quadratic growth model. The R^2 values of all indices (Table 12) were moderate across genotypes (generally between 0.65 to 0.79) indicating acceptable but not perfect fit for a quadratic model. In the context of biological and agronomic data, such values are considered acceptable and are frequently reported in phenological and crop growth modeling studies (ARCHONTOULIS & MIGUEZ, 2015). GLI and RGBVI are selected for modeling (Figure 28) due to their consistent high performance across all genotypes, allowing for standardized phenological curve comparison. Both vegetation indices are based on RGB bands, while GLI (Green Leaf Index) emphasizes green reflectance and correlates with chlorophyll and canopy development, RGBVI (Red Green Blue Vegetation Index) is sensitive to vegetation vigor and canopy cover, particularly during intermediate to late stages. Figure 28 shows that all fitted curves showed a typical quadratic pattern, an increase during early development, peak near full canopy cover and a decline during senescence. Both GLI and RGBVI curves peaked during the same date for all genotypes, approximately between 100 to 119 DAS, and declined after 133 DAS marking senescence. The fitted curves reflect key phenological transitions observed in the field as shown in Figure 9 in chapter 1. However, RGBVI had slightly higher peak values for IAC-80 and UFRB-222, whereas GLI had a steeper decline after peak for UFRB-222 ($a = -8.8854 \times 10^{-5}$).

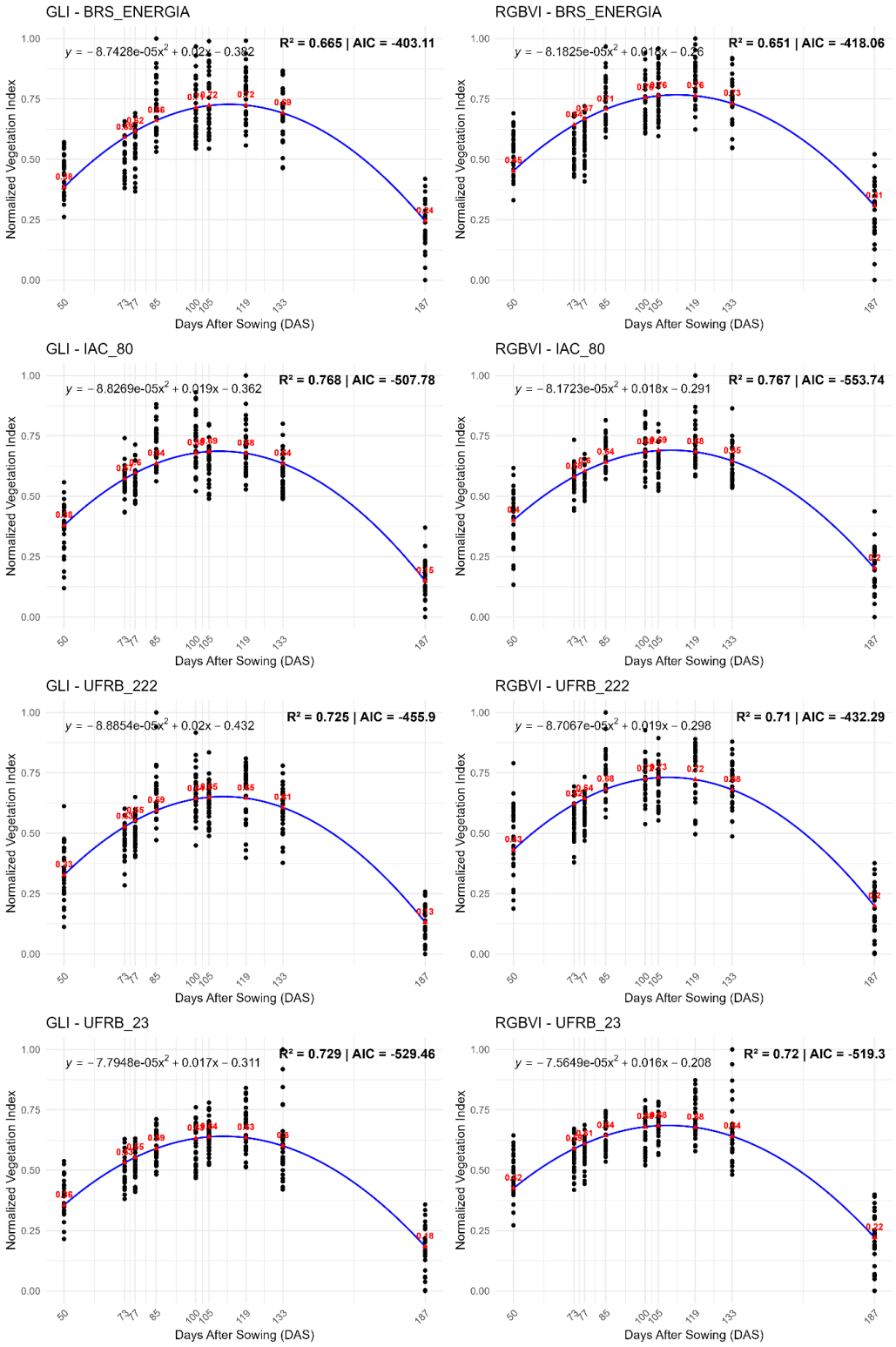


Figure 28. *Phenological growth modeling with GLI and RGBVI indices of four castor bean genotypes (BRS-ENERGIA, IAC-80, UFRB-222, UFRB-23) using quadratic model.*

DISCUSSION

❖ Model fitting

The quadratic and exponential models demonstrated excellent computational stability, successfully fitting all 120 genotype × vegetation index combinations without failure. Their robustness is largely due to their simplicity: quadratic models require only three parameters and offer flexible parabolic shapes, while exponential models effectively capture monotonic growth using just two parameters. In contrast, more complex models such as Gompertz, Logistic, Richards, and Weibull were more prone to convergence failures, particularly in datasets with high noise or low temporal resolution (PAINE et al., 2022; ARCHONTOULIS & MIGUEZ, 2013; Figure 25). These findings align with prior research emphasizing the reliability of simple nonlinear models for field-based plant growth modeling, where overparameterization and data variability can reduce convergence (PAINE et al., 2022).

Several datasets exhibited near-zero variance in vegetation indices, limiting the models' ability to capture dynamic changes. This can be attributed to:

- Canopy saturation at peak vegetative stages (XUE & SU, 2017; GITELSON et al., 2003)
- Index saturation effects, especially in NDVI-like indices (HABOUDANE et al., 2004)
- Imaging artifacts due to shadows or illumination (MULLA, 2013)
- Low biomass or early stress, leading to static reflectance patterns (HUNT & DAUGHTRY, 2018)

These conditions reduce the dynamic range needed for nonlinear modeling, leading to poor identifiability and convergence failures (Spiess & Neumeyer, 2010).

❖ Model evaluation and selection

Model selection was based on information-theoretic criteria, where AIC balances goodness-of-fit and model complexity (PORTET, 2020). Akaike weights were used to rank models by relative likelihood, enabling comparisons across non-nested models

(WAGENMAKERS & FARRELL, 2004). The diversity of selected models across genotype–index combinations reflects differences in canopy behavior, index sensitivity, and phenological progression (GITELSON et al., 2014; WU et al., 2010). Both symmetric (e.g., Logistic) and asymmetric (e.g., Gompertz, Richards) models were included to accommodate different curve shapes, such as early saturation or delayed response (YIN & NG, 2003; WU et al., 2012). Importantly, AIC and R^2 values are only valid within a specific dataset. Cross-comparison between genotype–index combinations is not methodologically sound due to differences in data structure and variance. For this reason, model selection was performed independently for each combination (BURNHAM & ANDERSON, 2002).

- **Model plotting and comparison**

GLI and RGBVI were selected for phenological modeling due to their consistent ranking among the top five indices across all genotypes. Previous studies confirmed the utility of these indices in similar crops, reporting R^2 values of 0.6–0.8 (BENDIG et al., 2018; Dias et al., 2022). The R^2 values obtained in this study (0.63–0.76) are consistent with the literature and reflect the expected variability in field conditions. Thus, GLI and RGBVI are validated as reliable indices for modeling castor bean phenology using quadratic models and can serve as effective tools for monitoring canopy dynamics.

CONCLUSION

- Growth parameters such as stalk diameter, leaf number, aboveground biomass, and chlorophyll content are essential field measurements for modeling and predicting the growth of *Ricinus communis* L.
- Regression models are dataset-specific and their performance cannot be directly compared across different genotype × vegetation index combinations. Consequently, it is not possible to identify which vegetation index is most efficient for castor bean phenological modeling.
- To overcome the limitations of nonlinear models, such as fixed curve shapes, sensitivity to data quantity, and limited variance, future studies should explore machine learning approaches that offer greater flexibility and predictive power.
- The accuracy of growth modeling can be improved by acquiring reflectance data at more than nine time points throughout the crop cycle, ensuring sufficient temporal resolution for robust predictions.
- Additionally, studies evaluating the effect of flight altitude on reflectance data quality are recommended, as altitude may influence vegetation index accuracy and consistency in RPA-based remote sensing.

Final Considerations

This thesis demonstrates that RPA-based imagery is a viable and promising pathway for high-throughput phenotyping of castor bean, particularly for traits linked to plant architecture and phenology. Across two chapters, we validated a workflow to estimate plant height using RGB derived DEM and modeled phenological dynamics from RGB and multispectral vegetation indices using linear and nonlinear growth models. Together, these results show that drones can deliver repeatable, plot-scale measurements that complement or replace manual assessments.

Methodologically, a central lesson is that spatial resolution (GSD) is the controlling variable, not flight altitude per se. Because GSD depends on camera pixel size, focal length, and altitude, reproducing a method across different equipment requires specifying a target GSD and image overlap and then computing altitude for each sensor to hit that target. In our conditions, later developmental stages, with larger leaves and denser canopies, produced more reliable DEMs and height estimates, while seedling/early stages were limited by sparse foliage and fine structures that are difficult to reconstruct at coarser GSDs. Castor bean's architecture (few, large leaves and variable stature) reinforces this pattern: more biomass tends to yield stronger correlations, whereas very dispersed or slender foliage challenges 3D reconstruction.

Operationally, drones proved systematic and scalable but remained sensitive to external constraints. Wind induces leaf and stem motion that can bias heights. The presence of illumination and shadow in the images, as well as field cleanliness (weeds) also affect reconstruction quality. Compared with a single-person manual campaign, our small test block showed manual measurement can be faster, but also more subjective and fatiguing due to ergonomic matter such as plants taller than evaluator. This suggests a break-even analysis is warranted: as area and plant count grow, RPAs likely overtake manual work in both efficiency and consistency. Identifying that threshold for castor bean breeding nurseries is a clear avenue for future work.

For castor bean breeding, height supports selection for compact architecture, a key attribute for harvest mechanization and lodging risk, and can accelerate genotype

screening when combined with other canopy traits. Other growth parameters should be included for better growth modeling, such as stalk diameter, leaf number, aboveground biomass, and chlorophyll content.

For smallholder impact in Brazil, the benefits are twofold. Indirectly, the workflow accelerates the development of cultivars better suited to their realities (e.g., compact architecture for easier harvesting). Directly, repeated flights and time-series modeling can inform management timing, such as anticipating harvest windows or detecting uneven development within a field.

REFERENCES

AHMAD, M. et al. Landsat images classification algorithm (LICA) to automatically extract land cover information in Google Earth Engine environment. 2020. Disponível em: https://www.researchgate.net/publication/340514580.

ARCHONTOULIS, S. V.; MIGUEZ, F. E. Nonlinear regression models and applications in agricultural research. Agronomy Journal, v. 107, n. 2, p. 786–798, 2015. DOI: https://doi.org/10.2134/agronj2012.0506.

BARBOSA, B. D. S. et al. RGB vegetation indices for the evaluation of the biophysical characteristics of soybean. Agronomy Research, v. 17, n. 2, p. 389–399, 2019.

BARNES, E. M. et al. Remote- and ground-based sensor techniques to map the spatial variability of plant nitrogen concentration. In: Precision Agriculture, p. 417–431, 2000.

BENDIG, J. et al. Combining UAV-based plant height from crop surface models, visible, and near infrared vegetation indices for biomass monitoring in barley. International Journal of Applied Earth Observation and Geoinformation, v. 39, p. 79–87, 2015. Disponível em: https://doi.org/10.1016/j.jag.2015.02.012.

BURNHAM, Kenneth P.; ANDERSON, David R. Model selection and multimodel inference: a practical information-theoretic approach. 2. ed. New York: Springer-Verlag, 2002.

CGIAR. Spectral vegetation indices. 2022. Disponível em: https://repo.mel.cgiar.org/handle/20.500.11766/6868.

DING, J. et al. Evaluation and refinement of the nitrogen reflectance index (NRI) for site-specific fertilizer management. Precision Agriculture, v. 15, p. 421–432, 2014.

ELZHOV, Timur V. et al. minpack.lm: R interface to the Levenberg-Marquardt nonlinear least-squares algorithm found in MINPACK. Vienna: R Foundation for Statistical Computing, 2016. Disponível em: https://cran.r-project.org/web/packages/minpack.lm/minpack.lm.pdf.

FERNANDES, J. L. et al. Mask R-CNN refitting strategy for plant counting and sizing in UAV imagery. ResearchGate, 2020. Disponível em: https://www.researchgate.net/publication/344348915.

FILELLA, I. et al. Evaluating wheat nitrogen status with canopy reflectance indices and discriminant analysis. Computers and Electronics in Agriculture, v. 43, n. 1, p. 43–55, 2004.

GITELSON, A. A. et al. Remote estimation of canopy chlorophyll content in crops. Geophysical Research Letters, v. 32, n. 8, p. 1–4, 2005.

GITELSON, A. A. et al. Remote estimation of crop gross primary production with green NDVI and light use efficiency. Remote Sensing, v. 6, n. 2, p. 1211–1233, 2014. Disponível em: https://doi.org/10.3390/rs6021211.

GITELSON, A. A.; VIÑA, A.; ARKEBAUER, T. J.; KEYDAN, G.; LEAVITT, B. Measurement of chlorophyll content in leaves with reflectance spectra: Testing a new algorithm in corn leaves. Remote Sensing of Environment, v. 85, n. 1, p. 67–80, 2003.

GITELSON, Anatoly A. et al. Remote estimation of canopy chlorophyll content in crops. Remote Sensing of Environment, v. 115, n. 2, p. 364–372, 2014.

GOMPERTZ, B. On the nature of the function expressive of the law of human mortality. Philosophical Transactions of the Royal Society of London, v. 115, p. 513–585, 1825. DOI: https://doi.org/10.1098/rstl.1825.0026.

HABOUDANE, D.; MILLER, J. R.; TREITZ, P. M.; ZARCO-TEJADA, P. J.; HU, B. Vegetation indices for predicting green LAI of crop canopies: Improved sensitivity under soil and illumination effects. Remote Sensing of Environment, v. 90, n. 4, p. 476–487, 2004. Disponível em: https://doi.org/10.1016/j.rse.2004.01.005.

HUNT, E. R.; DAUGHTRY, C. S. T. What good are unmanned aircraft systems for agricultural remote sensing and precision agriculture? International Journal of Remote Sensing, v. 39, n. 15-16, p. 5345–5376, 2018. Disponível em: https://doi.org/10.1080/01431161.2017.1410300.

HUNT, R. Plant Growth Curves: The Functional Approach to Plant Growth Analysis. London: Edward Arnold Publishers, 1982.

MULLA, D. J. Twenty-five years of remote sensing in precision agriculture: Key advances and remaining knowledge gaps. Biosystems Engineering, v. 114, n. 4, p. 358–371, 2013. Disponível em: https://doi.org/10.1016/j.biosystemseng.2012.08.009.

PAINE, C. E. T. et al. How to fit nonlinear plant growth models and calculate growth rates: an update for ecologists. Methods in Ecology and Evolution, v. 13, n. 7, p. 1482–1494, 2022. DOI: https://doi.org/10.1111/2041-210X.13905.

PORTET, Simon. A primer on model selection using the Akaike Information Criterion. Infectious Disease Modelling, v. 5, p. 111–128, 2020. Disponível em: https://doi.org/10.1016/j.idm.2019.12.010.

RICHARDS, F. J. A flexible growth function for empirical use. Journal of Experimental Botany, v. 10, n. 2, p. 290–301, 1959. DOI: https://doi.org/10.1093/jxb/10.2.290.

SAHA, S. K. et al. Satellite-based remote sensing for sustainable agriculture. Computers and Electronics in Agriculture, 2020.

SPIESS, André-Nicolas; NEUMEYER, Nils. An evaluation of R^2 as an inadequate measure for nonlinear models in pharmacological and biochemical research: a Monte Carlo approach. BMC Pharmacology, v. 10, n. 6, 2010. Disponível em: https://doi.org/10.1186/1471-2210-10-6.

WAGENMAKERS, Eric-Jan; FARRELL, Sarah. AIC model selection using Akaike weights. Psychonomic Bulletin & Review, v. 11, n. 1, p. 192–196, 2004. Disponível em: https://doi.org/10.3758/BF03206482.

WU, Changxin et al. Evaluation of vegetation indices for estimation of crop leaf area index. Agricultural and Forest Meteorology, v. 150, n. 5, p. 756–766, 2010.

WU, D. et al. Evaluating different models for simulating leaf area index (LAI) dynamics in winter wheat. Field Crops Research, v. 129, p. 17–26, 2012. Disponível em: https://doi.org/10.1016/j.fcr.2012.01.002.

Xing, N.; Huang, W.; Xie, Q.; Shi, Y.; Ye, H.; Dong, Y.; Wu, M.; Sun, G.; Jiao, Q. A Transformed Triangular Vegetation Index for Estimating Winter Wheat Leaf Area Index. *Remote Sens.* **2020**, *12*, 16. https://doi.org/10.3390/rs12010016

XUE, J.; SU, B. Significant remote sensing vegetation indices: A review of developments and applications. Journal of Sensors, v. 2017, Art. ID 1353691, 2017. Disponível em: https://doi.org/10.1155/2017/1353691.

YIN, X.; NG, E. A mechanistic model quantifying CO_2 effect on plant growth. Annals of Botany, v. 91, n. 4, p. 361–371, 2003. Disponível em: https://doi.org/10.1093/aob/mcg033.